PROCESSING AND PROPERTIES OF MATERIALS WITH OR WITHOUT ADIABATIC SHEAR SUSCEPTIBILITY

by

Xiaoxue Chen

A dissertation submitted to the faculty of
The University of North Carolina at Charlotte
in partial fulfillment of the requirements
for the degree of Doctor of Philosophy in
Mechanical Engineering

Charlotte

2018

Approved by:

_____
Dr. Qiuming Wei

_____
Dr. Laszlo Kecskes

_____
Dr. Harish Cherukuri

_____
Dr. Terry Xu

_____
Dr. Don Chen

©2018
Xiaoxue Chen
ALL RIGHTS RESERVED

ABSTRACT

XIAOXUE CHEN. Processing and properties of materials with or without adiabatic shear susceptibility. (Under the direction DR. QIUMING WEI)

In this dissertation, two topic areas related to adiabatic shear banding (ASB) phenomenon were studied. Body centered cubic (BCC) metals and alloys may exhibit ASB under uniaxial high strain rate compression if the grain size is refined into the ultrafine grained (UFG, grain size d > 100 nm but < 1000 nm) or nanocrystalline (NC, d < 100 nm) regime through severe plastic deformation (SPD). Such adiabatic shear localization behavior is an essential property for a kinetic energy (KE) penetrator which exhibits a "self-sharpening" effect. This means that the head of the penetrator remains sharp during the penetration so that most of the KE is primarily imparted to destroy the target. However, UFG/NC BCC refractory metals processed by SPD could not be used as KE penetrators due to the limitation of their physical dimensions. In this work, heterogeneous multi-layer structures of W/Fe/W and W/V/W have been produced using cold rolling and diffusion bonding to achieve a hierarchical structure whereby the limiting dimensions were extended and during testing the products exhibited ASB. The ASBs were observed to propagate through the heterogeneous layers and the bonding interfaces remained intact upon high rate loading. Subscale heterogeneous projectiles have been fabricated for ballistic testing. ASBs identified at the head of the projectile residuals suggest an early onset of shear localization behavior during the ballistic event.

In contrast to the former topic, a twinning induced plasticity (TWIP) steel with a composition of Fe-15Mn-2.5Si-2Al-0.6C and face centered cubic (FCC) structure has been found to exhibit strong strain and strain rate hardening upon the mechanical loading,

resulting in outstanding ASB resistance. The strain and strain rate hardening mechanisms have been experimentally investigated as a function of strain rate under uniaxial tension and compression. The steel sample is characterized by a constant strain hardening rate accompanied by high strength and high ductility under tension. This extraordinary strong strain rate hardening behavior was discussed in the context of deformation kinetics: high strain rate sensitivity (SRS) and low activation volume compared with coarse-grained (CG) FCC counterparts. It is reported for the first time: a marginal size effect has been revealed in this TWIP steel and it is attributed to an extremely small activation volume. According to the Zener-Hollomon equation, increasing the strain rate has an equivalent effect to that of a decrease in deformation temperature which favors the formation of twins with small thickness and spacing.

ACKNOWLEDGMENTS

I would like to sincerely appreciate my advisor Dr. Qiuming Wei for guiding and advising my Ph.D. work. He has the attitude and substance of a genius which continually inspired me in the journey of studying for my Ph.D. Without his guidance and persistent help, this dissertation would not have been possible. I would like to express my deepest appreciation to Dr. Laszlo Kecskes for being my committee member as well as discussing the problems I met during the research. I am grateful to Dr. Harish Cherukuri, Dr. Terry Xu and Dr. Don Chen for being on my doctoral dissertation committee and giving valuable suggestions on my research. Particular thanks are due to Dr. Xu for providing job hunting suggestions. In addition, a thank you to Mr. Franklin Green for setting up the diffusion bonding equipment, a thank you to Dr. Sergey Yarmolenko and Dr. Zhigang Xu at NC A&T for performing X-ray related experiments as well as TEM sample preparation, a thank you to Dr. Johnathon Ligda and Dr. Scott Walck at the U.S. Army Research Laboratory (ARL) and Dr. Jianghua Shen at Osaka University for FIB sample preparation and TEM examinations. Gratitude is also expressed to Dr. Lee Magness at ARL for performing the ballistic test and for his help with interpreting and understanding the testing results.

A very special gratitude goes out to the Graduate Assistant Support Plan (GASP) at the University of North Carolina at Charlotte (UNCC) and also the teaching assistantship from the Department of Mechanical Engineering as well as the research assistantship from the ARL.

Finally, last but not least, also a thank you to everyone in our research group. It was great sharing the laboratory with all of you and discussing problems with you all.

Thanks for all your encouragement!

TABLE OF CONTENTS

LIST OF TABLES

LIST OF FIGURES

CHAPTER 1: INTRODUCTION

1.1 Kinetic energy penetrators

1.1.1 Overview

Modern tanks use two main types of ammunition to defeat the armor of opposing tanks. One type is called high explosive anti-tank (HEAT) projectile which has an explosively driven warhead to penetrate the armor steel to a depth of seven or more times the diameter of the charge. The other type is armor piercing fin stabilized discarding sabot (APFSDS) projectile. The core part of the APFSDS projectile is a kinetic energy (KE) penetrator. KE penetrators are long-rod, armor-piercing projectiles that are fired from modern high-velocity tank guns; they aim to defeat an armored target by burrowing a cavity through the armored material [1]. This ammunition does not contain explosives but uses KE to destroy the target. Ideally, if the armor is defeated, the combination of heat, spalling (particle spray), and the pressure wave generated during the penetration process, destroys the target.

The underlying principle of the KE penetrator is that it uses kinetic energy, which is a function of its mass and velocity, to force its way through the armor. Therefore, for any material to be a good candidate for the penetrator applications, high mass density is one important requirement. Another imperative requirement is that the penetrator should exhibit a “self-sharpening” behavior which means that the head of the penetrator remains sharp during penetration. The rapid development of the flow and shear failure behaviors lead to a quick discard of the penetrator material which builds up at the head of the projectile. It helps to deliver a superior ballistic performance by effectively saving the penetration energy. In general, higher mass density and “self-sharpening” behavior should be the prerequisites for being a penetrator material. The performance of a prototype or

subscale penetrator is usually evaluated by ballistic test where projectiles are fired to a steel target at strain rate up to 10^6 s^{-1} at an indoor small-scale test range facility. By means of measuring and examining the diameter of the tunnel formed upon penetrating through the armor plate, the ballistic performance could be judged for comparison as well as evaluation purposes.

1.1.2 Depleted Uranium alloys penetrator and Tungsten heavy alloys penetrator

Depleted Uranium (DU) alloys, such as U-3/4Ti and U-8Mo alloys with high mass density (17-18 g/cm^3) are highly desired as the penetrator core materials because of their outstanding combination of high strength, good ductility, maintained ductility as well as "self-sharpening" behavior [2-4]. Figure 1.1 (a) is a schematic of the flow and failure behavior of a DU alloy penetrator. An early onset of shear localization occurred at the head of the DU projectile that helped to discard the material build up during penetration. In order to provide a visualized observation of a DU projectile, radiographic images of residual penetrators after perforating armor steel are shown in Figures 1.2 (a) and (b). Both of the U-3/4Ti alloy and U-8Mo alloy developed a chiseled and pointed nose, which depict early shear failure and discard mechanism. However, DU penetrators are made from the radioactive waste of the uranium enrichment process which can lead to acute and chronic toxicity to humans. Therefore, its application has been restricted and research is now being focused on finding environment friendly substitutes.

In an effort to replace DU alloys, W based heavy alloys (WHA) have emerged as attractive alternative candidate materials because of their unique combination of elevated temperature properties and high mass density (~19.3 g/cm^3). Conventional WHAs, such as W-Ni-Fe alloys produced by liquid phase sintering, have been widely studied as DU alloy

substitutes. However, WHA penetrators do not flow soften as quickly as DU alloys penetrators [2, 3], as seen in Figure 1.1 (a) as well as Figures 1.2 (a) and (b). From Figure 1.1 (b) and Figure 1.2 (c), plastic localizations develop only after the WHA has undergone very large plastic strains, producing a large "mushroom" head and thus reducing the eventual depth of penetration. The radiographic image in Figure 1.2 (c) further demonstrates that a mushroom head forms on the residual of the penetrator with late shear localization and discard mechanism.

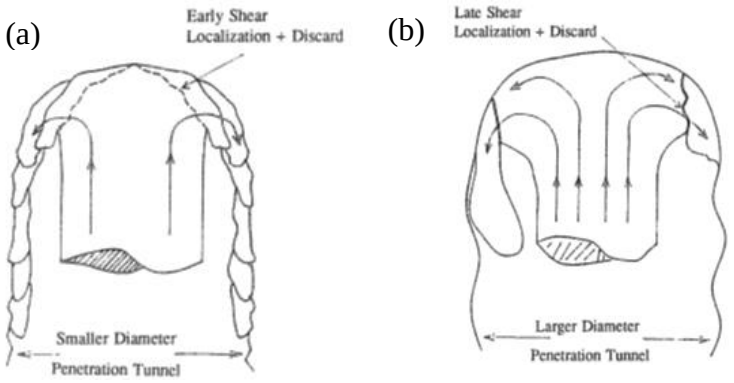

Figure 1.1: Schematic of flow and failure behavior of (a) DU and (b) WHA residual penetrators [5].

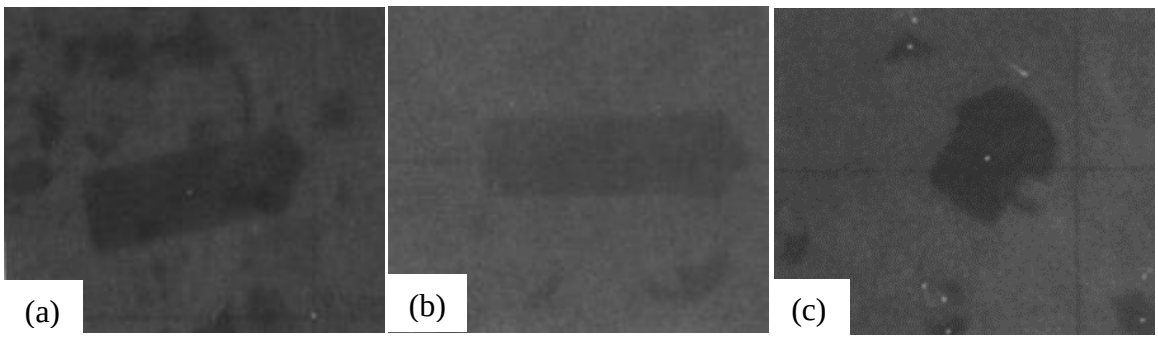

Figure 1.2: Radiographic images of residual penetrators after perforating armor steel: U-3/4Ti alloy (a), U-8Mo alloy (b), W composite (c) [1].

Evaluating the depth and morphology of the penetration tunnel created by DU alloy and WHA penetrators also provides a visualized result on their penetration performance. From

Figure 1.3, the volumes of both of the DU and WHA alloys' penetration cavities were almost equal if considering the experimental error of the measurement. However, the penetration tunnels produced by the DU alloy were narrower and deeper than the ones created by the WHA penetrator. Moreover, the penetration tunnel of the WHA penetrator is often more deteriorated because of its increased diameter due to the heavy plastic deformation at the penetrator's head [6], which further demonstrates a poor ballistic performance compared to a DU alloy penetrator. In general, under the same firing velocity, DU penetrator pierces deeper and generates a smaller diameter tunnel compared to WHA penetrators, which means that DU alloy penetrator delivers a better ballistic performance.

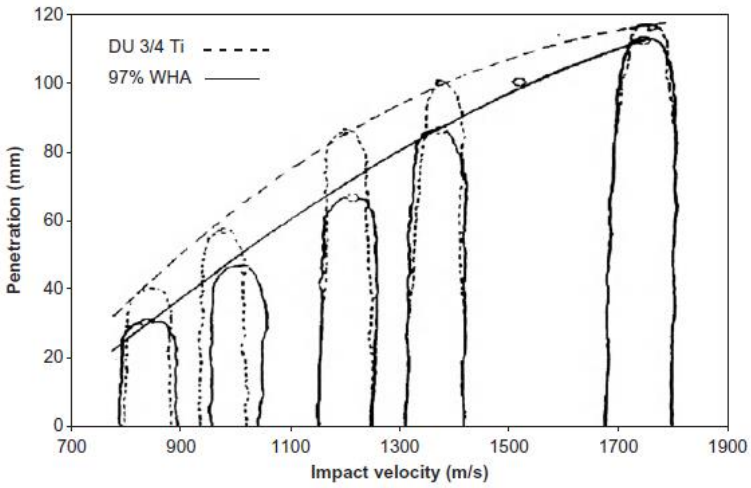

Figure 1.3: Comparison of penetration tunnels formed by U-3/4Ti alloy and 97% W content WHA into a mild steel target. The depth and shape of tunnels burrowed by DU alloy and WHA alloys penetrator are depicted by dotted line and solid line, respectively [3].

1.1.3 Adiabatic shear bands

1.1.3.1 Overview

The "Self-sharpening" effect is rooted in a material's tendency to have adiabatic shear banding (ASB) or adiabatic shear localization (ASL). Hence, the mechanism of ASB has been drawing scientific researchers' attention from the materials and mechanical

engineering fields.

In 1943, Zener and Hollomon [7] had for the first time recognized the relationship between plastic deformation and loading strain rate in steels. Since then, many mechanical engineers have conducted research to develop criteria to explain this plastic instability. Recht [8] came up with a hypothesis that high strain rate plastic behavior was influenced by temperature gradients which are a function of thermophysical properties, strain rate and shear strength. In 1981, Bai [9] derived a criterion for thermo-plastic shear instability in which titanium (Ti) became unstable at small strains and instability developed fully at high strain rates but for mild steel, this phenomenon was reversed. Then, an analytical study was carried out by Bai et al. [10] calculating the width of a shear band to be ~10-100 μm.

Adiabatic plastic deformation had also been widely studied in the area of high strain rate deformation, such as high velocity punching, high velocity forming, high speed machining, cryogenic deformation, ballistic testing, etc. [11-16] through experiments and numerical methods to examine the shear localization as well as its temperature dependence [17-20]. The numerical results for stainless steels showed that a temperature as high as the melting temperature was reached throughout the shear band shortly after the peak load was attained. In contrast, inside a tantalum (Ta) shear band, the temperature rise was less, and it changed from an initial room temperature to 898 K [21]. Validation of such temperature increases is very hard to measure during experiments. ASB was also observed in metallic glass; and composite materials through instrumented indentation tests and ballistic tests, respectively [22, 23].

Overall, ASB is a failure pattern of materials at high strain rates, when thermal softening overcomes strain hardening and strain rate hardening effects [7, 8, 24]. It is generally

characterized by failure inside the shear localization bands in which severe plastic deformation (SPD) occur and is confined to within the band and large strain gradients exist between the shear band and the rest of the material, which consequently leads to cracks.

1.1.3.2 The microstructural and mechanical aspects of adiabatic shear bands

Figures 1.4 (a) to (d) are examples of shear localization observed in WHA, interstitial-free steel, copper (Cu) and Ti by using Scanning Electron Microscopy (SEM), Electron Backscattered Microscopy (EBSD) and Transmission Electron Microscopy (TEM). Figure 1.4 (a) is a SEM image of a WHA alloy, processed by hot hydrostatic extrusion and hot torsion, tested under a uniaxial dynamic (DY) compressive load [25]. From the image, the WHA alloy sample displays a shear band with a width of about 100 μm along the diagonal of the micrograph. One should note that the grains sheared extensively inside the band and yet underwent recrystallization process. Flow lines turn downward through the boundary into the shear band and then curve away on the other side forming an antisymmetric pattern, which is typically called the canonical structure and could be used to predict the occurrence of ASB of W [26]. In comparison with the ASB in a refractory metal alloy, which has a high melting temperature, the ASB developed in an interstitial-free steel shows a totally different morphology with extensive recrystallized grains within the band and a well-defined shear band. It demonstrates that a large amount of heat is generated within the band due to a confinement of the SPD. Since the temporal scale of the shear deformation is much shorter than that of heat conduction, most of the heat remained within the band possibly recrystallizing the grains [27]. TEM images of Cu and Ti taken from the shear localization region further demonstrate the effect of heating by the presence of the nanoscale recrystallized grains with grain size of ~200 nm.

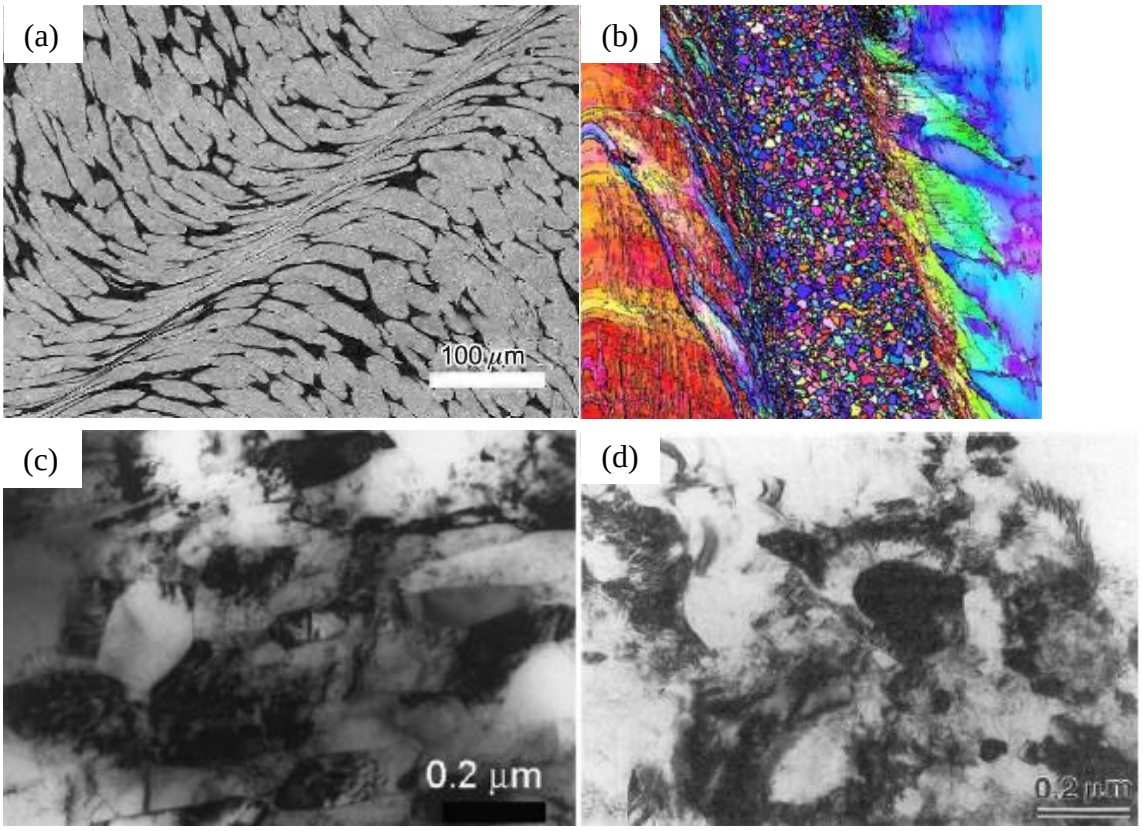

Figure 1.4: An overview SEM micrograph showing a localization of deformation in an adiabatic shear band in the extrusion and hot torsion processed WHA subjected to uniaxial dynamic compression [25] (a). An overview of an interstitial-free steel with an ultrafine-grained structure inside the shear bands (b). Ultrafine-grained structures in the bands of Cu (c) and Ti (d) [28]

In order to understand and correlate the microstructures of ASB to the high strain rate mechanical behavior, Marchand and Duffy [29] conducted a high strain rate torsional test at the strain rate of about 1.6×10^3 s^{-1} on HY-100 steel tubes, as shown in Figures 1.5 (a) and (b). From Figure 1.5 (a), an obvious strain hardening behavior was observed at stage 1 and homogenous deformation was demonstrated by the continuous and un-deformed grid patterns in the left of the micrograph in Figure 1.5 (b). At stage 2, strain hardening was negligible while an elastic-nearly perfectly plastic behavior [30] was observed from the stress-strain curve; the shear strain was up to 40 %. This could be explained by the triggering or onset of the thermal softening, offsetting strain hardening and strain rate

hardening. Slightly sheared grid patterns were observed in the middle picture in Figure 1.6 (b) with the grid pattern being continuous. While at stage 3, a stress collapse is clearly observed which indicated the onset of the ASB. The onset of the ductile failure via shear banding occurs in a sudden and a drastic way. These studies show that immediately following the onset of the ductile failure, the stress level at this material point drops almost vertically to about a quarter of its peak value. This is called a sudden drop, a ductile failure, or a stress collapse and they are used to derive a quantitative measure that can predict the onset of the ASB state [31]. The grid pattern in the right picture of Figure 1.5 (b) is not continuous anymore and a narrow shear band and even a fracture was observed on the sample surface.

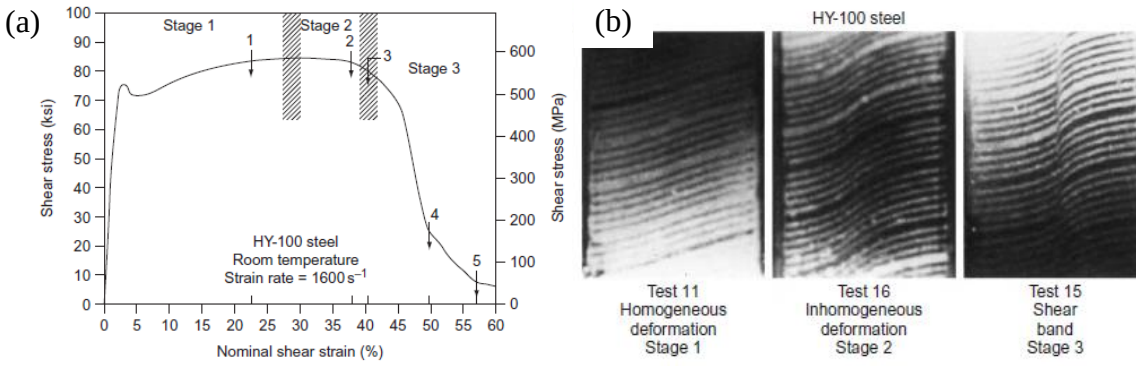

Figure 1.5: A typical stress-strain curve showing three stages of plastic deformation at strain rate of 1.6×10^3 s^{-1} (a) and corresponding images with grid patterns to display the deformation (b) [29].

1.1.3.3 Relationship between adiabatic shear bands and materials properties

The stress-strain curves and microstructural characteristics provide the experimental aspects of understanding the onset and development of ASB, while a theoretical study is important for investigating mechanisms and criteria of adiabatic shear instability.

In separate studies, Shockey and Staker [32, 33] developed the constitutive equation relating the shear stress under a pure shear load as a function of shear strain γ, strain rate $\dot{\gamma}$

and absolute temperature T

$$\tau = \tau(\gamma, \dot{\gamma}, T), \tag{1.1}$$

where

$$\frac{d\tau}{d\gamma} = 0. \tag{1.2}$$

Eq. (1.2) denotes the condition for plastic instability. That is, when the slope of the true stress-strain curve is zero, an instability develops and catastrophic shear or failure is imminent as given by

$$\frac{d\tau}{d\gamma} = \left(\frac{\partial\tau}{\partial\gamma}\right)_{T,\dot{\gamma}} + \left(\frac{\partial\tau}{\partial\dot{\gamma}}\right)_{T,\gamma}\frac{d\dot{\gamma}}{d\gamma} + \left(\frac{\partial\tau}{\partial T}\right)_{\gamma,\dot{\gamma}}\frac{dT}{d\gamma} = 0 \tag{1.3}$$

In Eq. (1.3), the three terms from left to right stand for the contributions from strain hardening, strain rate hardening and thermal softening. In other words, the shear instability or ASB occurrence is a competition among these three terms. The temperature rise within the material was estimated to be [34]

$$\Delta T = \frac{\alpha}{\rho C_p}\int_0^{\gamma} \tau \, d\gamma \tag{1.4}$$

if 90 % or more plastic deformation work is transformed into thermal energy; where α is a constant and is 0.9 for a Kolsky bar system. ρ is the material density, and C_P is the heat capacity (specific heat). As seen in Figure 1.4 (a), for the WHA, the shear band does not show a well-defined central region; this is different from other shear bands, such as the shear bands formed in severe plastically deformed steel, because the temperature rise within the bands might not be sufficiently high to cause extensive recrystallization. [26].

1.3.3.4 Susceptibility to adiabatic shear banding

A rough estimate of susceptibility of ASB from Wright [26] is given by

$$\frac{\chi_{SB}}{a/m} = \min\{1, \frac{1}{\left(\frac{n}{m}\right)+\left(\sqrt{\frac{n}{m}}\right)}\} \tag{1.5}$$

where χ is the susceptibility to ASB, a is a non-dimensional thermal softening parameter $a = -\frac{\frac{d\sigma}{dT}}{\rho c_P}$, m is the strain ate sensitivity, n is the strain hardening exponent, σ is the flow stress and σ_0 is the yield stress. Wei et al. [35] rewrote the above equation as

$$\frac{\chi_{SB}}{a} = \min\{\frac{1}{m}, \frac{1}{n+\sqrt{nm}}\} \quad (1.6)$$

under the assumption that thermal softening parameter is independent of temperature for a constant microstructure. From Eq. 1.6, the susceptibility to ASB can be discussed as a function of m and n. In general, vanishingly small m and n contribute to a high susceptibility to adiabatic shear banding.

1.1.4 Rate sensitivity of deformation of Face Centered Cubic (FCC) and Body Centered Cubic (BCC) metals

1.1.4.1 Strain rate sensitivity and activation volume

Strain rate sensitivity (SRS) and activation volume υ^* are two important parameters that are used to examine and describe the deformation kinetics quantitatively in metals with refined grain structure. The SRS depicts how a material's plastic flow behavior is sensitive to the strain rate. The higher the SRS value m, the more sensitive the plastic flow to the strain rate. For rate-sensitive materials, the presence of the strain rate sensitivity of flow stress, m, helps to sustain the homogeneous deformation

There are two ways to express the SRS of flow stress, and one of them is widely used in engineering community assuming a power law rate dependence,

$$m = \frac{d\ln\sigma}{d\ln\dot{\varepsilon}}. \quad (1.7)$$

The other one is [36-38]

$$m = \frac{\sqrt{3}k_B T}{\sigma v^*}, \quad (1.8)$$

where k_B is the Boltzmann constant and the activation volume υ* is defined as [38, 39].

$$v^* = \sqrt{3}k_B T\left(\frac{\partial \ln \dot{\varepsilon}}{\partial \tau}\right) \quad (1.9)$$

Activation volume is usually described as a measure of the Burger's vector multiplying the area swept out by dislocations during the thermal activation process. It is an activation enthalpy with respect to flow stress at a specific temperature, influencing the rate-related mechanics during the plastic deformation. Elmustafa and Stone [40] summarized the physical significance of studying activation volume. First, the activation volume differs from material to material even under the same class of materials. Second, the activation volume can be predicted in terms of the effects of parameters, such as dislocation density and solid solution concentration. Eq. 1.9 is a way to interpret activation volume physically from a uniaxial compressive stress or shear stress.

1.1.4.2 Body Centered Cubic (BCC) and Faced Centered Cubic (FCC) metals after severe plastic deformation

SRS and activation volume have been widely studied to understand the deformation kinetics of face centered cubic (FCC) and body centered cubic (BCC) metals with ultrafine scale grain (UFG, 100 nm < d < 1 μm) or nanocrystalline (NC, d < 100 nm) structure processed by SPD, such as equal channel angular pressing or extrusion (ECAP or ECAE), high pressure torsions (HPT) and low temperature or cold rolling (CR) [35, 37, 41-50]. The SRS of UFG/NC FCC metals is elevated while that of UFG/NC BCC metals is much reduced compared to their coarse-grained (CG) counterparts, and vice versa for activation volume [37, 51]. In other words, BCC metals after SPD with decreased SRS values have a propensity to show ASL at high strain rates. For FCC metals, such as Cu, the SRS values were 0.015 after CR and 0.019 for ECAP + CR while it is 0.004 for CG and annealed FCC

metals, the activation volume was about $45b^3$ for a UFG/NC structure while was ~$1000b^3$ for CG structure [37, 52]. However, ASL was also observed in refractory metals which have BCC lattice structures, such as tungsten (W), tantalum (Ta), vanadium (V), and niobium (Nb) under high strain rate (or DY) loading conditions with their grains refined into the UFG or NC scale through SPD [30, 35, 41, 48, 53-56]. Iron with a BCC structure and refined grains at ambient temperature also shows ASL at high strain rates [57]. The SRS value for CG Fe was 0.045 and activation volume was about $10b^3$ while SRS value for UFG/NC grain Fe was 0.009/0.007 and the activation volume was increased to $26b^3/17b^3$. A summary for BCC and FCC metals can be found in Table 1.1.

In a nutshell, BCC metals with UFG or NC grains processed by SPD yield low m increasing the propensity to show adiabatic shear failure. However, just having the low m value is inadequate to provide sufficient propensity to the shear banding instability. It is the lack of both strain hardening and strain rate hardening that allows softening mechanisms, either adiabatic or geometric, to function, thus, leading to shear banding as the primary mode of plastic deformation [58].

Table 1.1: SRS and activation volume values for CG, UFG and NC grain FCC and BCC metals [35, 37, 41, 48, 51, 52, 54-57].

			SRS	Activation volume
FCC	Cu	CG	0.004	$1000b^3$
		UFG/UC	0.015/0.019	$48b^3/41b^3$
	Fe	CG	0.045	$10b^3$
		UFG/NC	0.009/0.007	$26b^3/17b^3$
BCC	Ta	CG	0.046	$10b^3$
		NC	0.007	$12b^3$
	W	CG	0.04	-
		UFG	0.015	$10b^3$
	V	CG	0.05	-
		NC	0.014	-
	Nb	CG	0.045	-
		UFG	0.012	-

1.2 Heterogeneously stacked structure for kinetic energy penetrator application

1.2.1 Cold-rolled tungsten and its limitations

Pure commercial W processed by a cold-rolling (CR) technique exhibited elastic-nearly perfectly plastic deformation behavior under quasi-static (QS) loading and ASL at high strain rates, which meets the prerequisites of being a potential penetrator material [30, 54]. However, UFG or NC W cannot be used for fabricating KE penetrators directly due to the physical dimensional limitations of SPD, which can only process materials with thicknesses of about several hundred micrometer to a few millimeters. The dimensions of a nominal projectile in a prototype as well as at subscales are shown in Table 1.2 [59]. From Table 1.2, one can see that the length of a subscale projectile is about 24 mm at a minimum, while the prototype projectile length is about half a meter. According to current SPD methods, such as ECAP and HPT, as well as CR, it is very hard to manufacture a material with a final thickness from several tens of millimeters to a half meter scale through the use of common SPD laboratory equipment. Therefore, a proof-of-concept study of pure

W with significantly improved susceptibility to ASB having the appropriate dimensions would have an important merit for scientific reasons and demonstrating tits utility for the KE penetrator application.

Table 1.2: Nominal projectiles with prototype and subscale dimensions (L: length, D: diameter).

Scale size		Diameter (mm)
Prototype	L/D=20	25.4
	L/D=3.15	8.063
Subscale	L/D=6.30	4.032
	L/D=12.60	2.016

1.2.2 Diffusion bonding using an interlayer

1.2.2.1 Overview

Welding processes which widely use resistance and fusion can be classified into fusion welding and pressure welding, could bind two or more different metals, alloys and nonmetals together. The workpieces must be brought together within atomic spacing of each other to allow a permanent joint to form. Fusion welding happens when the workpieces are melted at their adjoining edges, then closure to within an interatomic distance takes place spontaneously as a weld pool is built up [60]. In contrast, pressure welding uses force or plastic deformation to bring the work piece to within the atomic spacing and joins the workpieces, via processes such as accumulative roll-bonding (ARB) [61, 62]. However, the metal that will be used for joining in this study is pure W that has a very high melting point and was severely deformed by rolling at temperatures lower than the homologous temperature of less than a quarter or so. Considering the melting point of W as well as the KE penetrator application, the aforementioned welding methods are excluded because the welding temperature may ruin the refined microstructure achieved by low homologous temperature rolling and, likewise, the stress wave propagation could

be stopped by intermetallic compounds that could form at the weld zone. Similarly, the ARB process may not provide a bonding interface which is strong enough to sustain the tensile stresses which are experienced during the projectile gun launching process.

Diffusion bonding is a solid-state welding technique used in metalworking, capable of joining similar and dissimilar metals. It involves the interdiffusion of atoms across the interface of a weld in the solid and, sometimes, the liquid state (when a molten interlayer is created) [60]. The diffusion bonding method has been studied to join dissimilar materials and fabricate a bulk material by stacking workpieces [63-70]. Using an interlayer between the workpieces help to decrease the bonding temperature caused by the large melting point difference between the two different materials or the high melting point of the material itself as well as the thermal expansion coefficient difference between two different materials [65, 66, 69, 70]. Diffusion bonding experiments between W and α-Fe, W and F82H steel using Ti interlayer, W and EUROFER97, W and Cu as well as W and V were widely studied in the literature [64-72]. These research efforts demonstrated that diffusion bonding could be a successful bonding method that may be used for bonding rolled W together using such an interlayer.

1.2.2.2 Diffusion bonding mechanism

There are four mechanisms that are widely used to explain the diffusion process in the literature: exchanging of places between two adjacent atoms, the motion of interstitial atoms, circular exchanging of four atoms and the motion of vacancies [60]. Among these modes, the motion of vacancies is the most popular mechanism with the lowest activation energy and was proved by Kirkendall Experiment where the vacancies in the lattice change places with adjacent atoms and the movement direction of vacancies is opposite to that of

the atoms. The possibility of an atom jump to an adjacent site is a function of the equilibrium concentration of vacancies

$$D = D_0 \exp(-\frac{Q}{RT}) \quad (1.10)$$

where Q is the activation energy of vacancy formation (J/mol or eV/atom), i.e., the energy that could activate an atom thermally so that it can clear the potential barrier between the sites and jump to an adjacent site. D_0 is a temperature-independent preexponential (m^2/s), R is the gas constant (8.31 J/mol·K or 8.62×10^{-5} eV/atom·K). The mathematics of steady-state diffusion in a single direction (x) can be expressed by Fick's First Law [73]

$$J = -D\frac{dC}{dx} \quad (1.11)$$

where J is the diffusion flux, and C is the concentration profile.

The success or failure of the process is determined by the bonding temperature, the bonding pressure (or pressing load) and the hold time (duration of pressure). The bonding temperature is a temperature which is below the recrystallization point but is sufficiently high to bring about the diffusion of atoms and molecules. It should be anywhere between 50% and 70% of the melting point of the most fusible metal in the composition. Elevated temperature helps the diffusion atoms across the interface of the weld as well as assists in the surface deformation by crushing or reducing the height of surface asperities.

Bonding pressure breaks up and removes the brittle surface oxide film and contaminants. Additionally, it brings the mating surfaces physically closer together, thereby enhancing atom-to-atom contact and atomic interactions. In the case of diffusion in a vacuum or an inert gas environment, deformation is only needed to crush the asperities on the mating surfaces so that an actual and successful contact can be formed. More specifically, the purpose of the pressing load is mainly to produce a micro-plastic deformation which would

lead to a maximum contact area between the mating surfaces and promote inter-diffusion. If the bonding pressure is insufficient, voids will be left unfilled, which will impair the joint strength.

Bonding time should be sufficient for an intimate contact to be formed and for diffusion processes to take place. It should be just sufficient for an intimate contact to be formed and for diffusion bonding to take place considering the economic efficiency of the process. An excessive diffusion time might leave voids in the weld zone or even change the chemical composition of the metal or lead to the formation of brittle intermetallic phases which could have a detrimental effect on the mechanical strength and consequently the quality of the joint [60, 63].

Surface roughness or asperities also affect the joint quality. For a sound joint to be formed, the surface roughness should be no more than 40 to 80 μm high for soft materials while no more than 2.5 μm high for hard alloys, refractory metals, high temperature alloys and tool metals [60]. Additionally, edges must be smooth and fit to each other for a good surface contact. Last but not least, a vacuum environment is preferred during diffusion bonding process and it should be maintained at a range between 10^{-1}-10^{-3} Pa. Inert gas environment, such as dry argon or dry helium, could also be the medium in the chamber.

1.2.2.3 Fe-W and V-W phase diagrams

The Fe-W and V-W phase diagrams can be seen in Figure 1.6 (a) and (b). There are three types of intermetallic phases in the Fe-W phase diagram: δ phase FeW, μ phase Fe_7W_6 and λ phase Fe_2W as a metastable phase. The δ phase FeW has an orthorhombic structure, μ phase Fe_7W_6 has a trigonal structure and the λ phase Fe_2W has a hexagonal structure. The W compositions (in wt.%) in δ phase FeW, μ phase Fe_7W_6 and λ phase Fe_2W are

50.7 %, 42.1 % and 33.3 %, respectively [74]. Different from the Fe-W phase diagram, the V-W system belongs to the binary isomorphic category. As such, a continuous series of solid solutions with a BCC structure can occur between W and V at all temperatures.

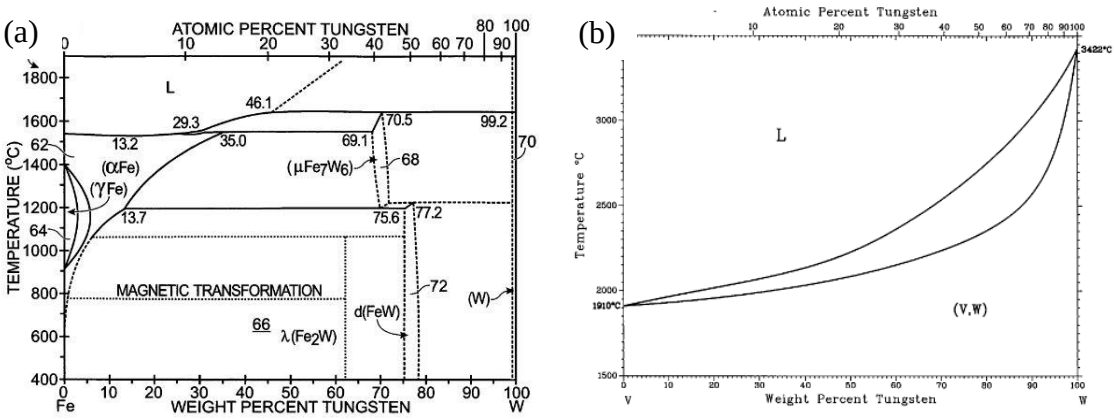

Figure 1.6: Phase diagrams of the Fe-W system (a) and V-W system (b) [74].

As such, V and Fe are two potential interlayers that could be used for creating the heterogeneously layered structure and extending the geometry to the desired dimensional scale of a proof-of-concept projectile through diffusion bonding. First, both of V and Fe have comparatively low melting temperatures which are 2183 K and 1811 K, respectively. As discussed before, using an interlayer between the workpieces helps to decrease the bonding temperature caused by the high melting point of the W material itself. Second, α-Fe, V and W, all have BCC structures with similar atomic radii as 0.127 nm, 0.135 nm and 0.137 nm, respectively. Third, the Fe-W system has a partial solid solution phase diagram while V-W system has unlimited solubility. Potentially, a certain amount of intermetallic in the Fe-W system could help in increasing the bond strength to some extent.

In a short, UFG W pieces processed by low homologous temperature rolling could be joined together by diffusion bonding using an Fe or V interlayer. Through this technique, a heterogeneously layered structure could be achieved by stacking W and the interlayer

alternatively to a desired geometry, which could overcome the inherent geometrical size limitation of rolled W and thus lead to a bulk manufacturing method for KE penetrator materials based on SPD W.

1.3 Armor materials

1.3.1 Overview

An armor is a protective covering that could be used to prevent perforation, piercing, or damage from being imparted upon by dissipating the impact, shock and blast energy from objects, individual or vehicle-borne by direct contact weapons or KE projectiles [75]. Monolithic plates or multi-layer materials or composites have been widely used for body armor or personnel armor, light armor used for vehicular, aircraft and heavy tank armor [76]. Textile based materials using high performance fibers can be classified into soft armor for personnel armor application [77].

Ti-6Al-4V was used as the commander's hatch and top protection armor on the M2 Bradley Fighting Vehicle [78]; previously, aluminum 5000 series armors were commonly used in Army land systems such as the Paladin Self Propelled Howitzer and armored personnel carriers while aluminum 7000 series armors were applied to the upper half of the Bradley fighting vehicle [79]. Concurrently, armor steels which have been extensively studied for ballistic impact resistance fall into two categories. One type is called rolled homogeneous armor steel (RHA), providing maximum resistance to penetration and shock, has been used to provide the protection of tanks, military sites, etc. because of its greater ductility preventing brittle fracture. To date, MIL-A-12560 under Class 1 specification, has been widely used to describe standard steel armor materials for comparison and determining the performance improvements of new candidate armors. Another type of

armor steel is face-hardened steel which is processed to have one face worked as the impact face to be much harder than the remainder of the plate thickness [80]. Carburizing and nitriding are commonly used as processing methods. However, the main deficiencies of faced-hardened armor is the inherent brittleness and difficulty in its manufacturing.

In addition to metallic armor types, ceramics, such as alumina, SiC and B_4C with high hardness and lower densities make them ideal candidates for high specific strength armor design. However, ceramics, if used as monolithic layers against projectile impact, easily fracture due to their lack of toughness [81].

1.3.2 Properties of armor steel

An armor steel which has a superior ballistic performance must be resistant to cracking, spalling and fracture upon impact while maintaining structural integrity. Hardness and toughness are taken into consideration in evaluating the ballistic performance of the armor steel. One should note that an upper limit on armor hardness has to be established to prevent shattering of the armor due to the embrittlement introduced by the high hardness [80].

In addition to hardness and toughness, the armor steel has to provide an excellent thermomechanical behavior and be resistant to a catastrophic deformation-adiabatic failure at high strain rates. As discussed previously, ASB occurs at high stain rates when thermal softening overcomes strain hardening and strain rate hardening. In other words, strong strain hardening behavior under QS and DY loading conditions is a prerequisite for any armor steel to be resistant to adiabatic shear failure. Moreover, a high SRS value and strong strain rate hardening behavior are preferred for armor steel for the purpose of preventing the formation of ASL.

1.3.3 Twinning induced plasticity steel

1.3.3.1 Introduction about twinning induced plasticity steel

TWIP steel, a current acronym used to describe twining induced plasticity steel, refers to the occurrence of mechanical twinning during straining. TWIP steels are fully austenitic steels with an enhanced strain hardening rate as well as high strength and good formability compared with other ferritic steels with elongation less than 25 % and relatively low ultimate tensile strength (< 1 GPa) which contribute to the controlling of crystallographic texture. Due to a low stacking fault energy (SFE) of 18 to 35 mJm^{-2} at room temperature, alternate deformation mechanism can occur such as mechanical twining during plastic deformation [82, 83]. In contrast, the SFE of transformation induced plasticity (TRIP) steel is less, ~12 to 18 mJm^{-2}, which allows the austenite to martensite transformation as the dominant deformation mechanism [84, 85].

TWIP steels primarily are composed of Fe-Mn-C which was developed based on Hadfield steels. In 1882, R. Hadfield [86] created a single phase austenitic steel alloy (Fe-Mn-C) with a chemical composition of 1.0 to 1.4 wt. % carbon (C) and 10 to 14 wt. % manganese (Mn) exhibiting strong work hardening. Since then, Fe-Mn-C based alloys have been widely studied. These include the effects of chemical composition on mechanical properties, work hardening and high strain rate property under tension, interaction between dislocations and the twin structure during straining, texture generation and evolution, and so on and so forth. Experiments and modeling of TWIP steels have been done in a variety of application fields, such as railroads, crusher jaws and cones, impact hammers and bullet-proof helmets because of their high strength, high toughness, good ductility, extraordinary strong work hardening and diminished instability during straining [82, 87-100]. Figure 1.7

(a) provides the fracture elongation as a function of tensile strength for many types of steels where high Mn austenitic steels, i.e. TWIP steels, demonstrate an outstanding combination of both of the elongation and strength among other types of steel that include dual phase steels, complex phase steels, TRIP steels, high-strength low-alloy steels (HSLA), etc.

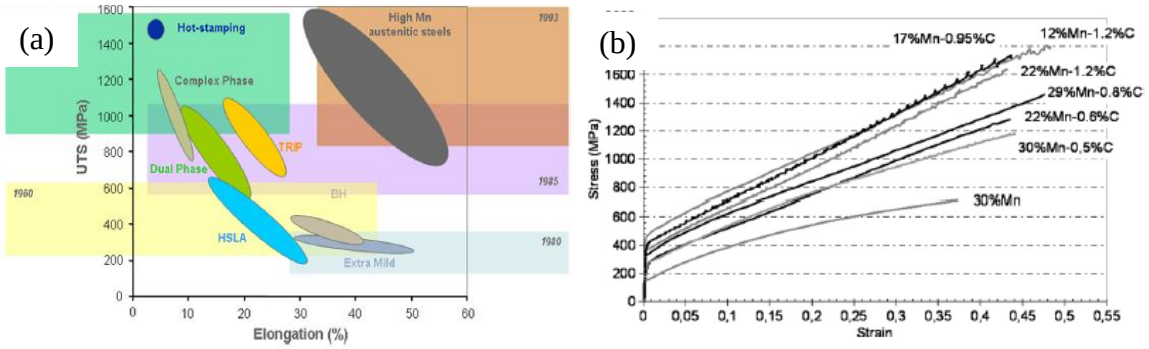

Figure 1.7: Fracture elongation in tension as a function of the ultimate tensile strength for steels (indicated years correspond to the approximate beginning of real development by steelmakers) (a). Tensile behavior of TWIP steels with coarse grains (between 20 µm and 40 µm) (b) [99, 101-104].

The remarkable balance between strength and ductility as well as the strong strain hardening make lightweight TWIP steels being exploited in the automotive industries with greatly enhanced formability. However, macroscopic plastic instability or serrated flow or jerky serration has been observed during the deformation of the austenitic high-Mn TWIP alloy [105]. The serrated flow or jerky serration in Figure 1.8 (b), caused by dynamic strain aging (DSA), can lead to deformation instability, cracking during forming or delayed fracture after forming. Silicon (Si) and aluminum (Al) are commonly added to TWIP steel, and, with a decreased Mn content to improve the formability, they effectively suppress the delayed fracture and, at the same time, also decrease the density of the TWIP steel. Addition of Al can raise the SFE of the steel alloy which decreases the tendency for twin formation and activating slip as well as promoting the dislocation movement [92]. However,

adding Si can decrease the SFE of the system and destabilize the austenite phase. Moreover, addition of both Al and Si increase strength of the TWIP steel by solid solution hardening and overall stabilize the austenite phase owing to their ability to slow down the precipitation of carbides, especially cementite, leaving more carbon available for enrichment of the austenite phase [82, 106].

Even though mechanical twins occur during plastic deformation, twinning is not the only one or main source of the observed large elongations before failure. Qin [107] estimated that the true strain resulting from twinning was less than 0.15 while it is usually larger than 0.5 for TWIP steel; the twin volume fraction that contributes to plastic strain usually does not exceed 3% [108]. In turn, the mechanisms of the observed extraordinary work hardening of TWIP steel were then explained by two main contributions: “dynamic Hall-Petch” effect and “dynamic strain-aging” mechanism. “Dynamic Hall-Petch” effect means that the deformation twining that developed during straining prevents dislocation movement and reduces the dislocation mean free path. The dislocations in the matrix can interact with the twins and lead to dislocation glide that may not be favorably oriented with respect to the loading direction. Twining boundaries act as grain boundaries which leads to a refined grain structure. In addition, few dislocation sources can operate inside twins since they are very thin [109-111]. “Dynamic strain-aging” mechanism indicates that the dislocations are pinned and locked by the solute atom dipoles (C-Mn), increasing dislocation density and thus the work hardening rate [112-116].

1.3.3.2 Mechanisms of twin formation in face-centered cubic (FCC) metals

Three fundamental twin formation mechanisms have been categorized according to the way of $\frac{a}{2} < 110 >$ glide dislocation dissociation in an FCC structure: pole mechanism,

model based on a deviation process and models based on SFs [117].

Venables [118] proposed two mechanisms to explain the pole mechanism. One is that the gliding dislocation dissociates into a Frank partial dislocation or the pole dislocation of type $\frac{a}{3} < 111 >$ and a Shockley twinning partial of type $\frac{a}{6} < \bar{2}11 >$ under the applied stress. The equation of this dissociation is:

$$\frac{a}{2}[011] \rightarrow \frac{a}{3}[111] + \frac{a}{6}[\bar{2}11] \tag{1.12}$$

The Frank partial dislocation is sessile while the Shockley dislocation could move away, leaving a wide intrinsic SF behind. The Shockley dislocation winds down and combined at the FCC close-packed plane and then a twin structure forms. This mechanism could explain the twin nucleation process and could also explain why the twin is easy to form at the close-pack plane. The other mechanism [119] could be used to explain the twin growth process in which a Shockley partial dislocation reacts with the perfect $\frac{a}{2} < 110 >$ dislocation during its movement in the matrix. At the same time, a Frank partial dislocation is created and left at the interface plane, as described in the equation:

$$\frac{a}{6}[121] + \frac{a}{2}[\bar{1}0\bar{1}] \rightarrow \frac{a}{3}[\bar{1}1\bar{1}] \tag{1.13}$$

In the deviation process based model, Cohen and Weertman [120] explained that the perfect $\frac{a}{2} < 110 >$ dislocation dissociated into a sessile Frank partial screw dislocation $\frac{a}{3} < 111 >$ and a gliding Shockley partial dislocation $\frac{a}{6} < \bar{2}11 >$, according the equation:

$$\frac{a}{2}[101] \rightarrow \frac{a}{3}[1\bar{1}1] + \frac{a}{6}[121] \tag{1.14}$$

Based on this theory, a deformation twin forms on a conjugated plane instead of the close-packed plane via the pole mechanism.

Last but not least, Mahajan and Chin [121] proposed a model that is based on the

presence of an extrinsic SF. In this theory, if the two co-planar perfect $\frac{a}{2}<110>$ dislocations meet, they could dissociate into three Shockley partial dislocations on three adjacent close-packed planes. Meanwhile, an extrinsic SF forms and plays a role of a three-layer nucleus for twin formation. The equation for this dissociation process is:

$$\frac{a}{2}[011]+\frac{a}{2}[\bar{1}01]\rightarrow 3\times\frac{a}{6}[\bar{1}1\bar{1}] \tag{1.15}$$

In the above model, Idrissi et al. [90, 117] confirmed this deviation model using TEM results to explain the twin formation process. A Shockley partial dislocation reacting with the perfect $\frac{a}{2}<110>$ dislocation could then be used in terms of the twin growth process explanation.

1.3.3.2 Strain hardening behavior

Strain hardening and strain rate hardening, usually described by the SRS, are two factors which influence necking or strain localization in metals under tension. Strain hardening or work hardening describes that when the dislocation density is increased during straining, the accompanying continued plastic deformation is responsible for the work hardening process, which means that dislocations themselves act as obstacles to the movement of other dislocations whereby a ductile metal becomes harder and stronger [122]. The true stress-strain relationship in the plastic region of deformation from the onset of the plastic deformation to the point of necking can be approximated by the flow stress equation

$$\sigma_T = K\varepsilon_T^n \tag{1.16}$$

where K is a material's strength constant and n is the strain hardening exponent which has a value less than unity. Materials with higher n values have better formability than those with low n values. The slope of the stress-strain curve, $d\sigma/d\varepsilon$, is used to define the strain hardening rate. The higher the strain hardening rate, the larger uniform elongation and

greater ultimate tensile strength. The theory of SRS was discussed in chapter 1.2.3.

The extraordinary strong strain hardening property of a variety of TWIP steels is clearly observed in Figure 1.8 (b) with different chemical compositions. Figure 1.9 (a) and (b) shows the four strain hardening stages of Fe-17Mn-0.4C-1.3Al TWIP steel interpreted by the way of the strain hardening rate. Stage A in Figure 1.8 (b) is the initial strain hardening stage with a decreasing strain hardening rate where the dislocation generation rate is relatively constant and dislocation annihilation rate by dynamic recovery is increasing while the role of twinning is absent. At stage B, the slip of dislocations and the interaction between dislocations start occurring and act as the role of twin initiation sites. The highest strain hardening rate is observed at the beginning of stage C and the strain hardening rate continuously decreases with strain. The reason could be explained as a reduction in the rate of primary twin formation. At stage D, secondary twin systems such as multiple twin-twin intersections are formed which considerably limit dislocation glide distances so that the strain hardening rate keeps decreasing with greater strains as a consequence. However, not all TWIP steel may exhibit stage D as shown, and the lack of stage D could be attributed to the absence of secondary twinning [108].

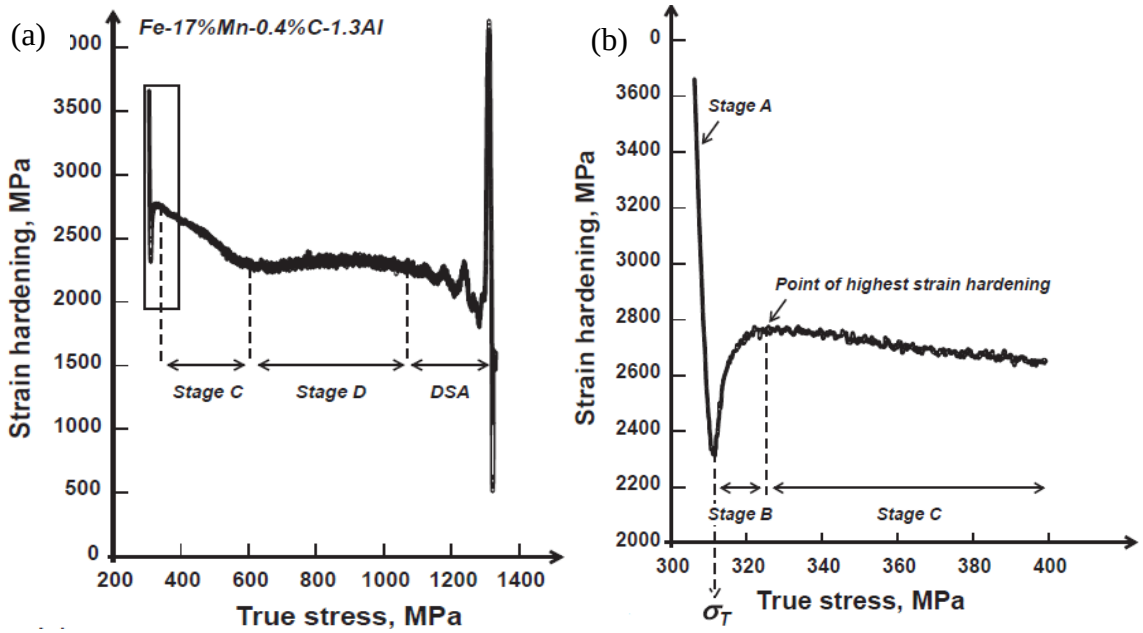

Figure 1.8: Fe-17Mn-0.4C-1.3Al TWIP steel showing four stages of strain hardening (a). Enlargement of initial strain hardening state (b) [108].

1.3.3.3 High strain rate behavior

The SRS value m in Eq. 1.5 and 1.6 are closely related to the activation volume which governs the dislocation glide. The m value is positive since the dislocation glide may be associated with thermally activated overcoming of dislocation forest junctions, stationary solute atoms or their clusters, or Peierls barriers [108]. Interestingly, researchers found that Fe-18Mn-1.5Al-0.22Si-0.6C TWIP steel exhibit a positive SRS when the strain was smaller than 0.1, but negative SRS as strain increases [90]. One of the dominant explanations to the negative SRS in the literature attributes this to dynamic strain aging (DSA) which requires a certain degree of coupling between the intermittent motion of dislocations and the evolution of mobile solute atoms [123-126]. It is important to suppress the occurrence of Portevin-Le Chatelier (PLC) bands and DSA because it was found that DSA leads to a rapid edge cracking during the whole expansion [124, 127, 128].

Besides DSA, the time-dependent twinning rate process, twin nucleation and twin

growth, should also be taken into consideration when discussing TWIP steel in the context of its strain rate hardening or its SRS [129, 130]. Fe-25.4Mn-2.55Si-2.28Si TWIP steel was sensitive to the strain rate under DY tensile loading, i.e., as the strain rate increased, the yield strength and ultimate tensile strength increased remarkably [131]. The investigation on an Fe-29.85Mn-2.98Si-3.07Al-0.059C also demonstrated a positive relationship between the strain rate and the stress as well as work hardening rate [132]. Fe-22Mn-0.4C TWIP steel at the strain rate of 10^3 s^{-1} has higher flow stress (maximum strength: 2265 MPa) than at a lower strain rate of 10^{-3} s^{-1} (maximum strength: 1798 MPa) [133]. Fe-(25-28) Mn-1.6Al -0.08C TWIP steel tested at the strain rate of 1250 s^{-1} showed higher flow stress at room temperature compared to the one tested at the strain rate of 10^{-3} s^{-1} [82]. However, the mechanism behind the increased flow stress at high strain rate or the strain rate hardening behavior of the TWIP steels have not been explored and explained in detail in the literature yet.

1.4 Objectives of this dissertation

After reviewing the rate sensitivity of BCC and FCC metals with UFG or NC structure processed by SPD, we acknowledged that W after rolling, has developed a propensity to ASB under high stain rate loading, which makes it a potential KE penetrator material, including other advantages, such as high mass density, high melting point, etc. However, no one has successfully fabricated UFG or NC W that has a suitable KE penetrator dimension using standard SPD laboratory equipment.

In this work, the low homologous temperature rolled W layers will be stacked together using Fe or V interlayers in between to produce three-layer structure and a multi-interlayer bulk material through diffusion bonding. The purpose of this study is to investigate the

microstructure as well as the high strain rate mechanical behavior of the W/Fe (V) /W heterogeneous structures and demonstrate if ASB or ASL could occur at high strain rate. This study is a proof-of-concept if a heterogeneously layered structure would be applied to the fabrication of W based KE penetrators and overcome the geometrical size limitations of SPD processed W. Therefore, the study of a significantly improved susceptibility to ASB of pure W along with the appropriate dimensions will have important implications both technologically and scientifically.

Many studies have been published in the literature on TWIP steels to investigate their high strength, good ductility and strong strain hardening behavior [82, 87-94, 97-99, 108, 117, 129, 131, 132, 134-145]. However, the mechanism behind the negligible instability under tension, strong strain hardening and strain rate hardening under both QS and DY loading conditions have not been discussed in depth yet. Therefore, revealing the mechanisms that dominate these outstanding properties have important merit both theoretically and practically from an application perspective.

CHAPTER 2: MATERIALS AND EXPERIMENTAL PROCEDURE

2.1 Materials

The starting material for rolling was a W slab purchased from the Alfa Aesar Company (Ward Hill, MA) with a purity of 99.95 % (metals basis). The Fe and V foils were purchased from the Alfa Aesar Company (Ward Hill, MA) with a thickness of 25 μm and 75 μm, respectively. The purity of the Fe foil is 99.5 % (metals basis) and 99.8 % (metals basis) for the V foil.

The investigated TWIP steel was manufactured by Salzgitter Mannesmann Forschung (Salzgitter, Germany) with a chemical composition being shown in Table 2.1. The chemical analysis was requested by U.S. Army Research Laboratory and performed by Luvak Inc. (Boylston, MA).

Table 2.1: Chemical composition of the TWIP steel.

Element	Wt. %	At. %
Fe	Balance	Balance
Mn	14.7	14.2
Si	2.49	4.72
Al	2.06	4.06
Cr	0.083	0.085
Cu	0.075	0.063
Ni	0.046	0.042
Ti	0.014	0.016
Mo	0.007	0.0039
Ni	0.0066	0.0038
Co	0.0057	0.0051
V	0.0045	0.0047
	Interstitials	
C	0.636	-
O	0.0009	-
N	0.0006	-
H	0.00033	-
S	< 0.001	-

2.2 Materials processing

2.2.1 Rolling

The sharp corners of the W slab were removed to avoid stress concentrations during rolling. Each surface of the W slab was roughly polished to eliminate surface oxidation and contamination. Then the work piece was sealed in a stainless steel canister to minimize oxidation when heating in a box furnace to 1073 K for 15 min before rolling. This was necessary since W starts to oxidize in air from 873 K [146].

Rolling was performed on a laboratory rolling mill (FENN, The Horsburgh & Scott Co., Cleveland, OH) with 0.254 mm thickness reduction per pass (Figure 2.1). The W workpiece thickness was reduced to ~0.7 mm with a total equivalent strain of ~1.74. The rolled W was then extracted from the stainless steel canister and cut into squares with dimensions of ~10 mm by 10mm and polished on both sides to a surface finish of ~0.5 μm using SiC sandpapers and diamond lapping films. The Fe foil with a thickness of ~25 μm and V foil with at thickness of ~75 μm were used in their as received condition. Before bonding, both of the W piece and foils were cleaned for 15 min in an ultrasonic bath with acetone at room temperature.

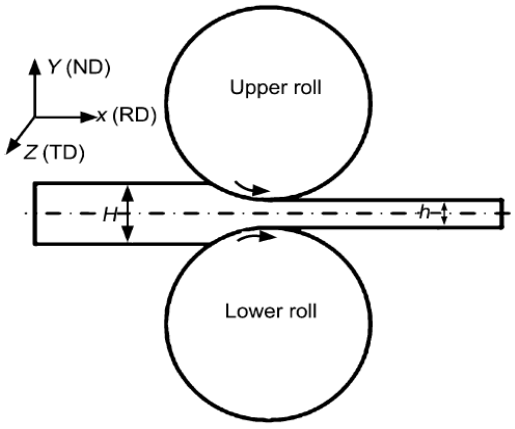

Figure 2.1: Schematic of the rolling system. Normal direction (ND), rolling direction (RD) and transverse direction (TD) are shown in figure.

2.2.2 Diffusion Bonding

Rolled W pieces were stacked together with an Fe or V interlayer in between, as seen in Figure 2.2 (a). Diffusion bonding was performed on an MTS 810 hydro-servo system as shown in Figure 2.2 (b). The contact face between W piece and compression platen was lubricated by lithium-based grease to reduce fiction. The model 652 high-temperature furnace with the MIC2000 controller system was used to heat the sample to the bonding temperature and maintained the temperature during bonding. The heating rate was controlled and was set to 20 K/min and the temperature was held at the 1073 K for 1 hr. After bonding, the sample was furnace cooled with an applied pressure. Dry Argon gas was flowing in during the entire bonding and cooling processes. The bonded piece was then EDM cut into specimens for high strain rate compressive mechanical testing.

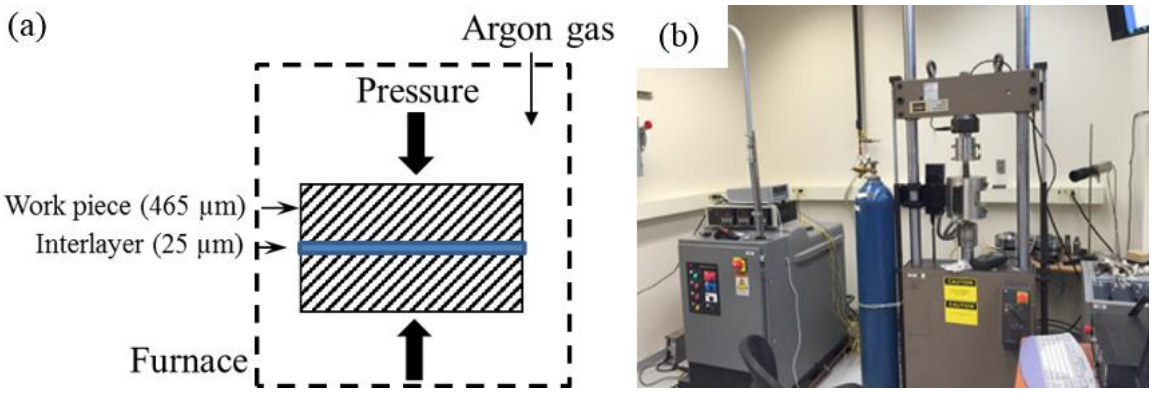

Figure 2.2: Schematic representation of diffusion bonding using hot press (a). The MTS 810 hydro-servo system (b).

The bonding temperature was chosen to be at 1073 K by considering that this temperature falls into the range of 50 %-70 % of the Fe or V interlayer melting point, which is 1846 K and 2147 K, respectively. Note, the bonding temperature cannot be higher than that of rolling. Otherwise, the benefits, such as ductility and propensity to ASB gained from the lower temperature rolling will be diminished [54].

Table 2.2 is the flow stress values of α-Fe at different temperatures and rates for various strains. Bonding pressure was chosen to be at 24 MPa based on the flow stress values of α-Fe at 1073 K, listed in Table 2.2. It was assumed that the selected bonding pressure will deform the asperities of the Fe interlayer and develop actual contact between the W and Fe surfaces. Bonding pressure for W/V/W system was determined to be at 230 MPa based on the values listed in Table 2.3. Bonding time was selected to be 1hr for the W/Fe/W and W/V/W systems for an intimate contact to form and the diffusion process to take place. However, this should not be so long as to change the chemical composition of the metal or lead to the formation of brittle intermetallic phases. Dry Argon gas was flown in the tube furnace to create an inert gas environment during the diffusion bonding.

Table 2.2: Flow stress values (in MPa) of α-Fe at different temperatures and rates for various strains [147].

Strain	Strain rate, s^{-1}	Temperature, K		
		973	1073	1173
0.1	0.001	48.6	22.8	20.1
0.2		54.2	24.4	21.3
0.3		54.9	24.8	21.9
0.4		56.5	24.1	22.4
0.5		57.9	23.6	22.7

Table 2.3: Tensile properties of vanadium sheet deformed at an engineering strain rate of 6.67×10^{-4} s^{-1}. Tests at 1173 K and 1273 K were repeated twice [148].

Temperature, K	UYS, MPa	LYS, MPa	0.2 % offset	UTS, MPa
1073	128.92	112.385	-	119.969
1173	91.011	82.048	-	110.316
1173	106.869	89.632	-	106.869
1223	-	-	72.965	91.431
1273	-	-	54.882	63.914
1273	-	-	63.975	78.124

Three types of heterogeneously stacked structures were prepared by diffusion bonding: a three-layer W/Fe/W structure, a three-layer W/V/W structure and a fifty-one layer

W/Fe/W bulk sample. The three-layer structures with a total thickness of ~1.5 mm were intended for testing at high strain rates using a split-Hopkinson pressure bar (SHPB) or Kolsky bar system. The fifty-one-layer W/Fe/W structure with a total thickness of ~12 cm was intended for the subscale ballistic test.

2.3 Microstructural characterization

Microstructural characterization before and after mechanical testing is crucial for understanding the microstructure-mechanical property relationship. Microstructure characterization tools, such as X-ray diffraction (XRD), scanning electron microscopy (SEM)/energy-dispersive X-ray spectroscopy (EDX)/Electron backscatter diffraction (EBSD) and transmission electron microscopy (TEM), were used to examine the microstructural and crystallographic properties of both the W based-heterogeneously stacked structure and the TWIP steel.

2.3.1 X-ray diffraction

A Bruker AXS D8 Discover X-ray diffractometer (XRD) with CuKα target ($\lambda = 0.154$ nm) was used to study the crystallographic texture and phase identification of TWIP steel. The TWIP steel sample that was used for the XRD examination has dimensions of about 9 mm × 4 mm × 3mm, wherein the 3 mm was the thickness. The surface was polished to a 0.5 μm finish and then lightly etched with a 10 % of Nital solution (10 % Nitric acid and 90 % ethanol) for releasing the surface stress concentration that was introduced by mechanical polishing.

2.3.2 Optical microscopy/scanning electron microscopy/energy-dispersive X-ray spectroscopy/electron backscatter diffraction

Optical microscopy (OM) was frequently used to identify the microstructure of the

metals before and after deformation with appropriate polishing and etching procedures. The contrast between different phases, grain size, micro twins and the morphology of ASB can be observed from OM. In this work, an Olympus BX51 OM was used for optical examination of the W/Fe (V)/W structure and TWIP steel. The W/Fe (V)/W structure and as-received TWIP steel before and after mechanical testing were polished to a 0.5 μm surface finish, followed by etching with Murakami's solution and 3 % Nital solution, respectively. The purpose of performing optical examination on W/Fe (V)/W is to reveal the grain size change before and after rolling, bonding interface quality and the morphology of ASB in the heterogeneously stacked structure. TWIP steel was studied for the microstructure change, especially the occurrence of mechanical twins, before and after the mechanical tests.

The W/Fe (V)/W samples after diffusion bonding and high strain rate test were examined with a JEOL 6480 SEM/EDX. Post-loading SEM observations were performed on the dynamically tested samples in order to reveal flow lines within and around the shear bands. An EDX spectrometer attached to the SEM was used to identify the chemical composition and atomic diffusion across the W/Fe (V) bonding interface. Field emission SEM with an attached EBSD detector was used to study the crystal orientation and phases of the W/Fe/W sandwich sample. The EBSD sample was prepared first through mechanical polishing down to 0.05 μm using a series of sand papers and alumina suspensions. Then, a vibration polishing process using a colloidal silica polishing suspension was carried out for 4hr. A step size of 0.05 μm was in use. Fracture analysis of the tension and compression tested TWIP steel samples was also studied by the JEOL 6480 SEM.

2.3.3 Transmission electron microscopy

TEM specimens from the W/Fe/W sample after bonding, away from and inside the ASB were prepared by focused ion beam (FIB). The TWIP steel TEM samples were prepared by mechanical polishing down to a thickness of less than 100 μm followed by a twin-jet electrochemical polishing (Struers, Westlake, OH), using a chemical solution of 90% CH_3COOH and 10% $HClO_4$. A JEOL JEM 2100 with a LaB_6 filament was used to take the bright field (BF) image, dark field (DF) image, diffraction pattern (DP) and selected area diffraction pattern (SADP). A Field emission TEM (Titan, Hillsboro, OR) with STEM and EELS was used to analyze the intermetallic compounds within the W/Fe/W structure.

2.4 Mechanical testing

2.4.1 Nanohardness

Nanoindentation test was performed on the sample with a surface finish of 0.5 μm using MTS Nano Indenter G200. The W/Fe (V)/W structure and TWIP steel surfaces were slightly etched by Murakami solution and 3 % Nital, respectively, for surface stress releasing, which was introduced by mechanical polishing. During the test, the Berkovich indenter tip approached the sample surface with a velocity of 10 nm/s starting from a distance 1000nm above the sample surface. The allowable thermal drift rate was 0.5 nm/s or lower and surface detect stiffness criteria was 125 N/m. The maximum load used for the W/Fe (V)/W structure was 9.8 mN, while it was 500 mN for the TWIP steel.

2.4.2 Tension and compression tests

Flat, dog-bone tensile specimens were machined from the as-received TWIP steel with a gauge length of 25 mm, width of 6 mm and thickness of 5mm (ASTM E8/E8M) along the RD and TD. The tensile test was carried out on an Instron 5580 load frame at room

temperature. A non-contact video extensometer was used to measure the strain of the sample upon tensile loading. The gauge section of tensile sample was carefully polished to 6 μm surface finish to remove any defects or stress concentrations.

QS compressive test samples were machined from the TWIP steel with dimensions of ~2.5 mm × 2.5 mm × 5 mm with the gauge length being 5 mm. QS uniaxial compression test was performed on the Instron 5580 with a strain rate of ~10^{-3} s^{-1} at room temperature. An Instron 5900R was used for QS compression test inside an environmental chamber at cryogenic and elevated temperatures (145 K to 588 K). The compressive strain of the specimen was derived based on the cross-head displacement of the loading system. The interfaces between the loading surfaces and platens were lubricated by a lithium-based grease to reduce friction effects.

2.4.3 High strain rate compression test

High strain rate compression test was conducted on an SHPB system as shown in Figure 2.3. A sample was sandwiched between two co-axial, same diameter steel bars. The striker bar, launched from the gun barrel by high compressive gas, impacted the free end of the incident bar and a stress wave was generated. The stress wave traveled along the incident bar and loaded the sample. Part of the stress wave was reflected and part of it was transmitted. Two strain gauges were cemented on the incident and transmitted bars to record the stress wave signals, which were recorded by a high speed multi-channel oscilloscope. The stress history could be evaluated by capturing and analyzing the transmitted signal and the equation is shown as

$$\sigma_s = \frac{A_0 E \varepsilon_t}{A_s} \tag{2.1}$$

where σ_s is the stress of the sample, A_0 and A_s is the cross sectional areas of the bars and

specimen respectively, E is the Young's modulus of the specimen and ε_t is the transmitted strain. Capture and processing of the reflected signal yields the strain history of the specimen. The strain at any time t can be determined by integrating the strain rate from 0 to t,

$$\varepsilon_s = 2\frac{C_0}{L_s}\int_0^t \varepsilon_r dt \tag{2.2}$$

where ε_s is the strain of the specimen, C_0 is the wave propagation velocity in the steel bar, L_s is the specimen's original gauge length and ε_t is the reflected strain. Together they provided the high strain rate stress-strain data. Strain rate of the specimen is given by $\Delta\upsilon/L_s$, where $\Delta\upsilon$ is the velocity difference across the specimen. The interfaces between the specimen and the bars were carefully lubricated to minimize friction effect because friction at the specimen and bar interfaces causes the state of stress to deviate from the the uniaxial stress condition and leads to spuriously stiff results [149]. Details of the Kolsky bar technique can be found in Ref. [150].

Two SHPB systems were used in this work, one with a bar diameter of 8 mm and the other with a bar diameter of 5 mm. Except for the bar diameter, the rest of the main components are the same in these two systems. The SHPB system could be used for the testing at strain rate ranging from ~1×10^3-5×10^4 s^{-1}. [149].

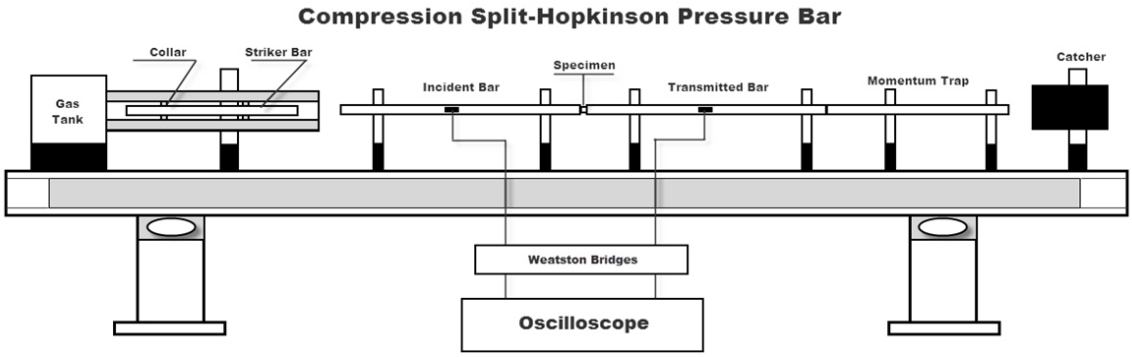

Figure 2.3: Schematic of a compression Kolsky bar system with the major components shown.

High strain rate test samples were machined from the W/Fe (V)/W structure and TWIP steel with dimensions of 1.5 mm × 1.5 mm × 1 mm and 2.5 mm × 2.5 mm × 2 mm with gauge length being as 1 mm and 2 mm, respectively. Surfaces of the specimens were polished to a surface finish of 0.5 μm before mechanical loading for direct post-loading microscopic examinations. W/Fe (V)/W samples were tested by the SHPB system with a bar diameter of 5 mm and TWIP steel samples were tested by the SHPB system with a 8 mm bar diameter.

2.4.4 Ballistic performance

Ballistic testing was conducted at an indoor small-scale test range facility at the U.S. Army Research Laboratory (Aberdeen Proving Ground, MD). A laboratory gun consisting of a Bofors 40 mm gun breech assembly with a custom-mode 40 mm smoothbore barrel was used for projectile launching (Figure 2.4). The gun was positioned approximately 3 m in front of the RHA targets and the propellant weight was adjusted to achieve the desired nominal velocity which was about 1500 $m \cdot s^{-1}$ [5, 151]. The positions of the projectile was recorded and the depth at which each scale model penetrator came to rest in the target was also measured for evaluating its penetration capability. After ballistic testing but before

sectioning the target, Bi-Sn was filled in the penetration cavity to secure the residual for follow-up microstructure characterization. However, sometimes residual was to be removed from the RHA target and examined separately. Not only the residual but also the target block, especially the projectile-target interface and the rear of the projectile position in the target block, was carefully polished and exanimated to achieve the information about ASB.

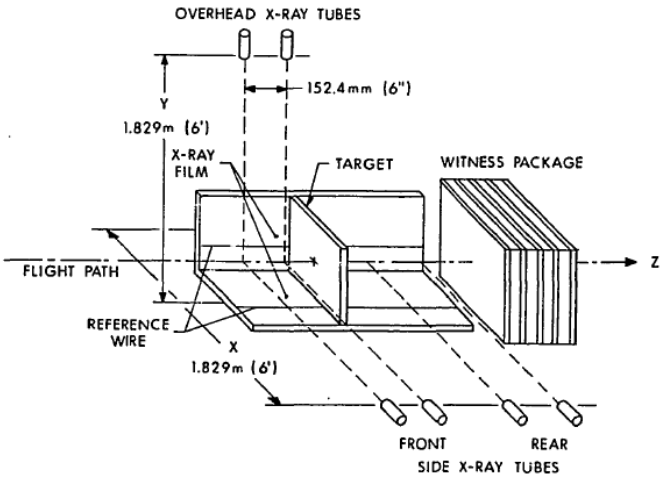

Figure 2.4: Schematic of ballistic test experimental setup [2].

The W/Fe/W multi-layered structure with a 12 mm thickness was EDM machined into 2 projectiles with 4 mm in diameter and 12 mm in length. A mild steel target with a hardness of 1.67 GPa was used, considering the small geometry of the projectile as well as the projectile consumption rate during penetration process. A sabot was used to keep a sub-caliber flight projectile in the center of the barrel during the acceleration from the gun tube. A steel “pusher plate” supported the projectile from the rear and distributes the set-back force over the plastic obturating plug [2]. Figure 2.5 is a schematic of the sabot that used for the forward ballistic test. The shaded area at the core indicates the position of W/Fe/W projectile.

Table 2.4 lists the ballistic test parameters of the two W/Fe/W projectiles against the mild steel target. The velocity was about 1000 $m \cdot s^{-1}$ and the depth of the penetration in the mild steel target was 14 mm for both shots 1 and 2, and the α, β and γ angle listed Table 2.4 are also shown in Figure 2.6, which provide pre-impact and post-impact ballistic measures. Specifically, α indicates the striking pitch, orientation of the projectile relative to its flight path, measured in the vertical plane. β is the striking yaw, orientation of the projectile relative to its flight path, measured in the horizontal plan and γ means the total solid angle orientation of the striking penetrator to its initial flight path ($\alpha^2 + \beta^2 = \gamma^2$).

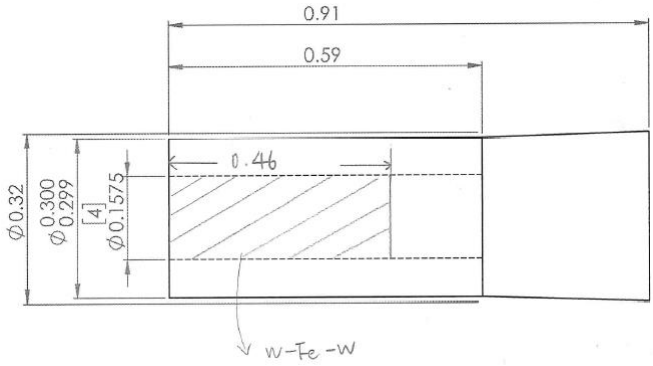

Figure 2.5: Schematic of a sabot for forward ballistic test.

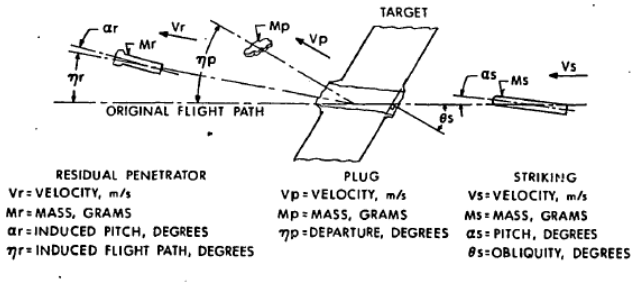

Figure 2.6: Pre-impact and post-impact ballistic measures [2].

Table 2.4: Parameters of W/Fe/W projectile against the mild steel target.

Shot	Mass (g)	D × L (mm)	α (deg.)	β (deg.)	γ (deg.)	Velocity ($km \cdot s^{-1}$)	Depth of penetration (mm)
1	2.54	4.01 × 12.50	1.94	2.63	3.27	1.09	14
2	2.41	3.76 × 11.76	− 1.68	3.98	4.31	1.09	14

CHAPTER 3: W/Fe (V)/W (BCC)-PROPENSITY TO ADIABATIC SHEAR BANDING AT HIGH STRAIN RATES

In this chapter, the W/Fe/W sandwich structure fabricated by diffusion bonding will be discussed first in the context of its microstructure and atomic diffusion, followed by its mechanical properties, such as its nano-hardness and high strain rate deformation behavior. Then, the occurrence of ASL at high strain rates and intermetallic phase analysis at the interface before and after loading will be examined in detail using OM, SEM, and TEM. Similarly, the W/V/W sandwich system with a V interlayer will be investigated to demonstrate the universality of ASL in these heterogeneously stacked structures.

3.1 Three-layer structure (Fe interlayer)

3.1.1 Microstructural analysis

Figure 3.1 (a-c) displays the optical micrographs of the W/Fe/W structure after diffusion bonding and the corresponding RD, TD and ND views are shown in Figure 3.1 (d). From Figure 3.1 (a) which is the microstructure image of the W layer, the grains are elongated and parallel to the RD. This typical, stretched grain structure was introduced by the low homologous temperature rolling, and the W grain width is ~5 μm-10 μm. Since the bonding temperature is 1073K which is lower than the recrystallization temperature of W, no nucleation and grain growth should be expected to be seen. However, a large number of dislocation annihilation is expected to happen during the bonding process, which will be demonstrated by the TEM results in chapter 3.1.5.

Optical images at the W/Fe bonding interface are presented in Figures 3.1 (b) and (c) at low and high magnifications. The Fe foil which is sandwiched between two W sheets can be seen as a white stripe in the images. Because of the lack of chemical reactivity between

Fe and Murakami's solution, no Fe grain or grain boundary is revealed or shown in the microstructural images. From the low and high magnification images at the interface, intact bonding faces were formed during diffusion bonding without any obvious cracking, voids or debonding being observed at or near the interfaces. However, some dark areas inside the Fe foil, close to the interfaces are seen in Figure 3.1 (c). An explanation could be that intermetallic compounds formed during diffusion bonding and most of them were formed within the Fe layer. This argument could be supported by the fact that it is easier for W atoms to diffuse into Fe than Fe into W. More details will be discussed in section 3.1.2.

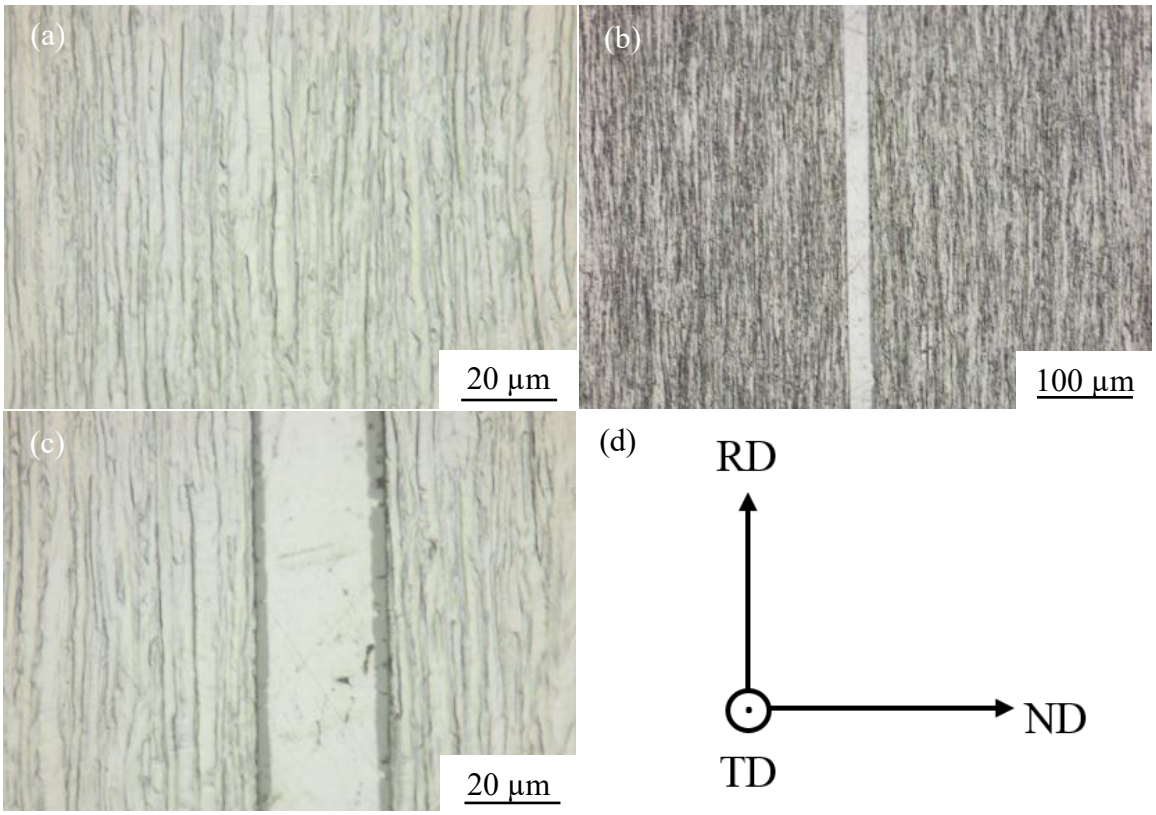

Figure 3.1: Optical micrograph of W part in W/Fe/W system after bonding (a). Optical micrographs of W/Fe/W at low and high magnifications (b, c). Schematic of corresponding RD, TD and ND (d). The light strip in (b) and (c) indicates the Fe interlayer which is sandwiched between two W layers. Images were taken after etching with Murakami solution and parallel to the TD.

EBSD examination was conducted on the W/Fe/W sample with results being shown in

Figure 3.2. Figures 3.2 (a) and (b) are SEM images of the W/Fe/W layred system at a tilt angle of 0° and 70°, respectively. A tilt angle of 0° is used to perform normal SEM examination while a tilt angle of 70° is used for EBSD examination which is shown in Figure 3.2 (c). The region highlighted in a dashed box in Figure 3.2 (b) indicates the position where EBSD scanning was performed.

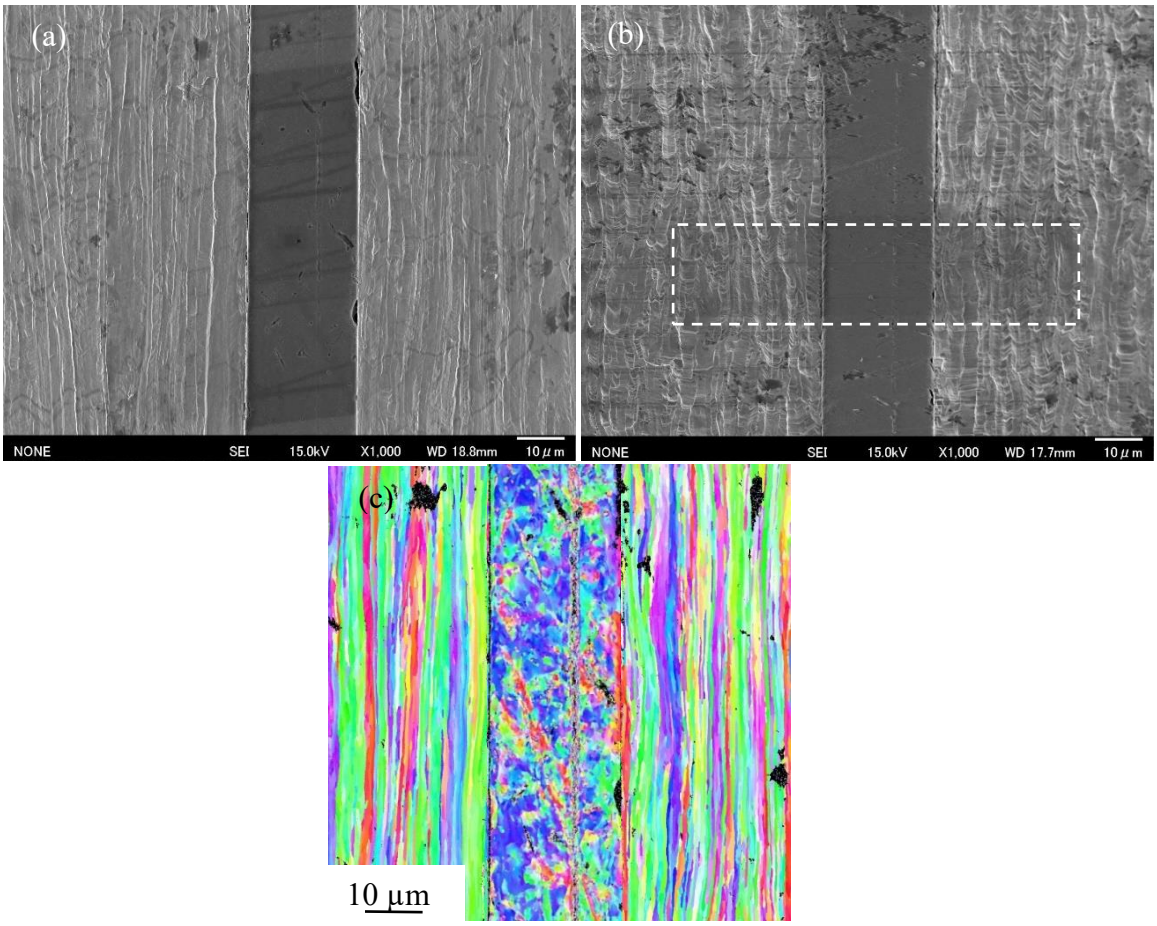

Figure 3.2: SEM images at a tilt angle of 0° (a) and 70° (b). EBSD result from both of the W and Fe parts (c). The EBSD scanning was performed separately for W and Fe layers. Only part of W sheets was scanned.

From the EBSD images and the scanning results, the elongated W grains are clearly revealed and the grain morphology is consistent to those under OM in Figure 3.1. A few localized voids with a micrometer scale along the bonding faces are observed and the voids may contribute to the gaps between asperities which were not completely closed during

diffusion bonding. The nonuniform Fe grain morphology in Figure 3.2 (c) could be caused by recrystallization and grain growth at the 1073 K bonding temperature, since the recrystallization temperature of Fe is only about 888 K.

3.1.2 Atomic diffusion across the interface

During diffusion bonding, inter-diffusion occurred between the W and Fe at an atomic scale upon the applied compressive stress, as well as the high temperature and then, intact bonding face could be formed. Since the bonding quality and the microstructure change may have an effect on the interface strength and the following high strain rate test, it is important to investigate the atomic inter-diffusion across the W/Fe interface.

Two interfacial junctions between the W and Fe contact surfaces formed during diffusion bonding are displayed in Figures 3.3 (a) and (b). Line scans were conducted across the bonding faces with a length of 5.5 μm from the left end to the right end. The scanning paths are drawn as yellow lines in Figure 3.3 (a) and (b) where W is the section with the lighter color. Figures 3.3 (c) and (d) show the diffusion analysis at the interfaces. The horizontal axes in Figures 3.3 (c) and (d) represent the scanning lengths which correspond to the scanning paths in Figures 3.3 (a) and (b). The vertical axes in the Figure 3.3 (c) and (d) express the W and Fe atom counts that were received by the detector. The gradual concentration decrease or increase for either W or Fe indicates that mutual atomic diffusion occurred in the interface region.

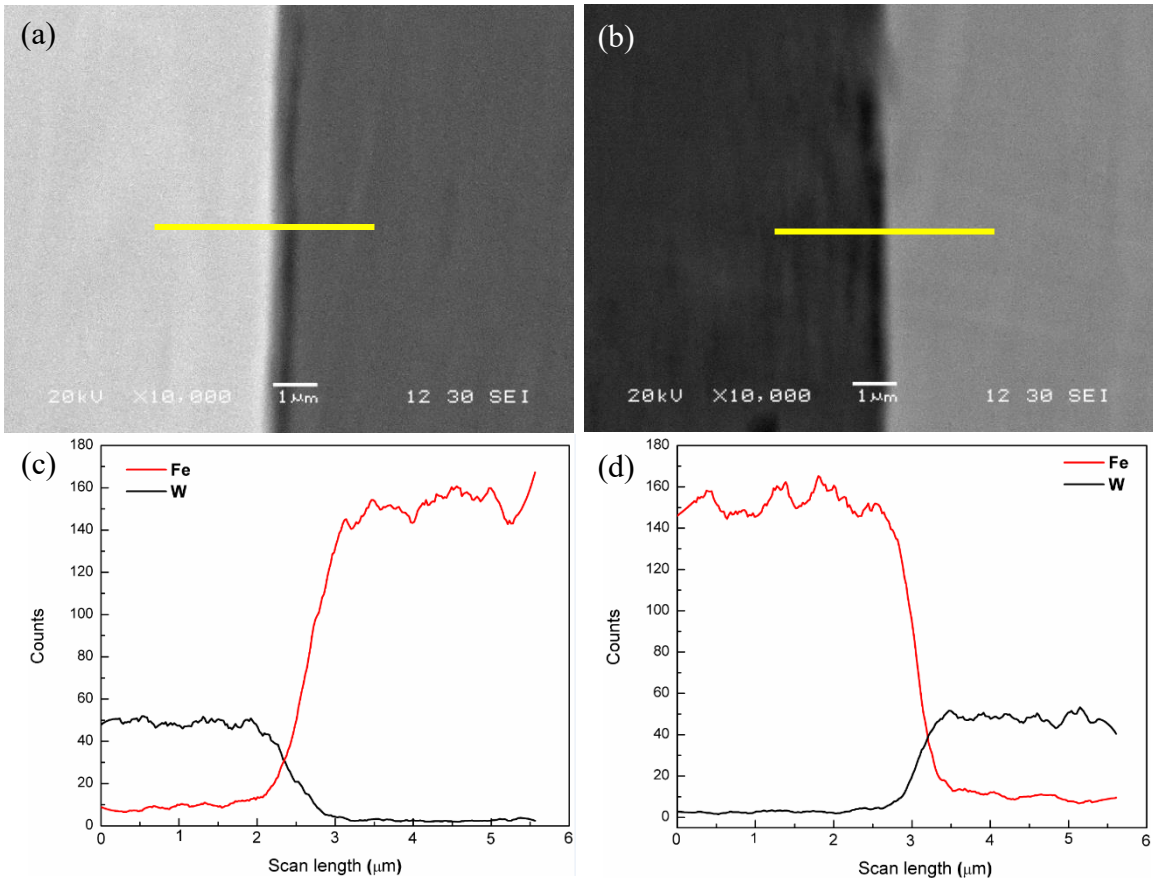

Figure 3.3: SEM images of two bonding junctions formed at W and Fe bonding faces with a darker area being as Fe part and a lighter area being as W part (a, b). EDX analysis of Fe and W atoms couple diffusion at two bonding interfaces (c, d). Image (c) displays the results from image (a) while (d) is the results from image (b). Yellow lines in (a) and (b) indicate the EDX line scan length and positions.

The concentration gradient in the interface region indicated by the EDX results clearly shows and demonstrates the occurrence of inter-diffusion across the bonding face. However, the elemental concentration or concentration profile is not revealed by EDX line scan. In order to provide a better understanding of the atomic diffusion quantitatively, nine-point elemental composition analyses were conducted along the yellow line in Figure 3.4 (a) with the corresponding concentration profile being shown in Figure 3.4 (b). Table 3.1 displays the elemental concentration from point A to B in weight %. From the Table 3.1 and Figures 3.1 (a) and (b), the W concentration is 2.6 % at point A (inside Fe foil) which

is 4.6 µm away from the interface. When the point analysis is conducted at the point 1 µm away from the interface but still inside the Fe foil, the Fe concentration decreases to 96.7 % while W concentration increases to 9.3 %. Right at the interface, the chemical composition of W and Fe is about half and half, where Fe is about 48.2 % and W is about 51.9 %. However, no Fe atom was detected when the point analysis was performed inside the W region.

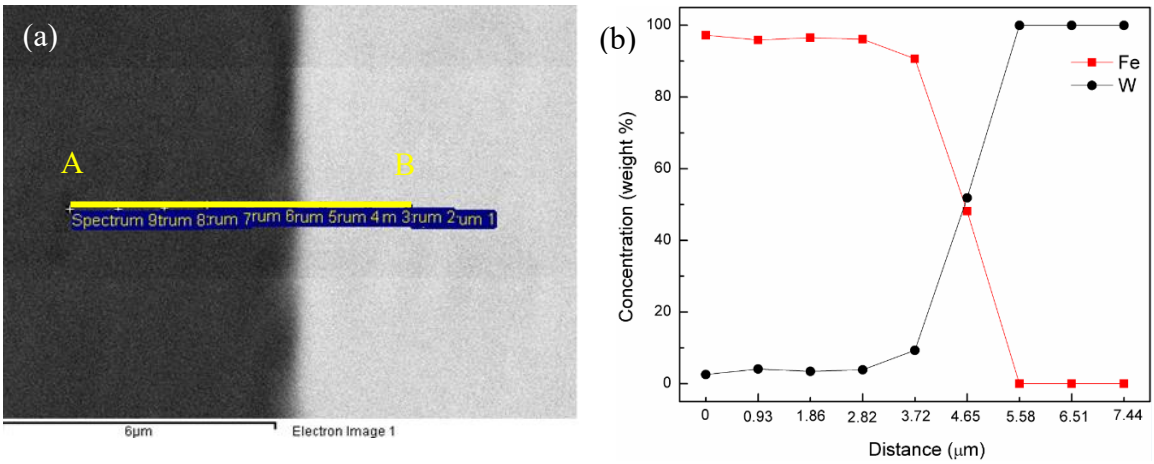

Figure 3.4: SEM micrograph of an Fe/W interface with a yellow line indicating the positions of nine point EDX analyses (a). Point A (spectrum 1 in Table 3.1) is at the left end of the yellow line while point B (spectrum 9 in Table 3.1) is the ninth point at the right end. The distance between each point was ~0.93 µm. Elemental concentration profile of W and Fe along the interface (b). Darker area on the left in image (a) is the Fe part while lighter part on the right is W part.

Table 3.1: Element concentration from A to B in weight % in Figure 3.4.

Spectrum	Fe	W	Total
Spectrum 1	97.25	2.57	100.00
Spectrum 2	95.93	4.07	100.00
Spectrum 3	96.56	3.44	100.00
Spectrum 4	96.13	3.87	100.00
Spectrum 5	90.67	9.33	100.00
Spectrum 6	48.15	51.85	100.00
Spectrum 7	0.00	100.00	100.00
Spectrum 8	0.00	100.00	100.00
Spectrum 9	0.00	100.00	100.00

From the point analysis and concentration profile performed by EDX, it may be concluded that W atoms are easier to diffuse into Fe than Fe into W, which is consistent with the optical observations in Figure 3.1, where suspected intermetallic phases or solid solution formation might have occurred at the interface, but only inside the Fe foil. This is reasonable as in couple diffusion scenario, W atoms have a greater possibilities to squeeze into the vacancies in the Fe foils because the atomic bonds in the Fe foil are more active and easier to break at the bonding temperature. In Peterson's work in 1960 [152], the diffusion coefficient of W in to Fe was provided at a series of temperatures. From Eq. (1.10), the activation energy for W diffusion into Fe is calculated to be 243 kJ/mol, and the temperature-independent preexponential is 5.26×10^{-4} m^2/s. Then the diffusion depth of $\sqrt{Dt}$ is roughly calculated to be 1.68 μm, which falls on the same order of magnitude of the experimental observation.

3.1.3 Nanoindentation hardness examination

Tightly formed W/Fe interfaces were observed and analyzed from OM and SEM images. Atomic interdiffusion was demonstrated to exist at the interfaces, which were further examined by EDX line scan analysis as well as point chemical analysis in previous examinations. However, the existence of intermetallic compounds or solid solutions that appear in the W/Fe phase diagram has not been examined yet. In this section, nanoindentation hardness measurements are performed at the interface and in the surrounding W and Fe layers for the purpose of identifying the presence of intermetallics or solid solutions; it is known an intermetallic compound would have a higher hardness value than that of either pure metal. Upon bonding at high pressure and temperature, Fe and W would have a propensity to form intermetallic compounds, Fe_2W and FeW, as was

depicted in Figure 1.6 (a).

Nanoindentation tests were performed on the cross-sectional surface of the sandwiched W/Fe/W sample, as shown in Figure 3.5 (a). The distance between consecutive indentations is ~10 μm and the angle between the array of indentations and the horizontal line is ~80°. The indentations were then projected to the horizontal line with a distance between consecutive indentations being ~1.74 μm. The hardness values across the interface and surrounding W and Fe regions are shown in Figure 3.5 (b). The average hardness of W is 8.22 GPa, while the 3.06 GPa for Fe. The values in the interface region fall between the hardness of W and Fe, as shown in Table 3.2. The intermediate hardness value at the interface could reflect that solutionizing occurs, i.e., the dissolution of W into the Fe matrix. There is no steep hardness increase observed at the W/Fe interface. However, it is possible that the intermetallic phase is too small to be detected by a nanoindenter.

Table 3.2: Nano indentation hardness values of the composite.

Materials	Hardness values (GPa)
W	8.22
Interface	6.75
	5.1
	4.18
	3.06
Fe	3.06

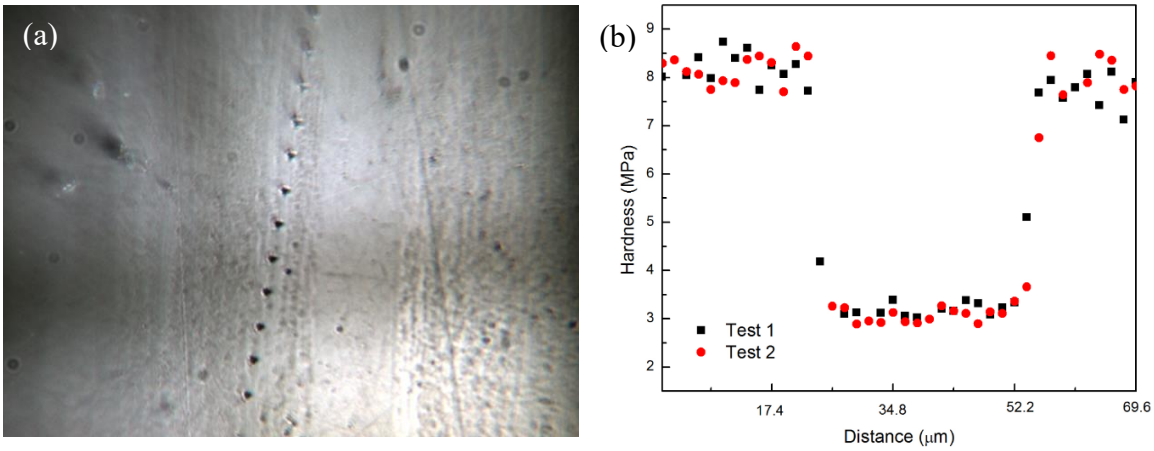

Figure 3.5: Indentation image (a) and nanoindentation hardness test (b) across the bonding interfaces (b). Two nanohardness trials in image (b) were conducted across the interface and surrounded W and Fe parts.

3.1.4 High strain rate compressive mechanical properties

Figure 3.6 represents the uniaxial high strain rate true stress-strain curves of the W/Fe/W layered structure at various strain rates (~6×10^3 s^{-1} to ~1.0×10^4 s^{-1}). A peak flow stress value of ~4000 MPa has been reached. Another profound observation from these stress-strain curves is that all of the stress-strain curves show an extraordinary flow softening which is favorable to the ASB formation. One should note that the flow stress fluctuation at high strain rates is inevitable upon high rate loading which has been also observed and documented in other literature [132].

Due to the adiabatic heating, the global temperature rise in the sample can be calculated by Eq. (1.4). The mass density ρ was taken as 19.25 g/cm^3 for this hierarchical structure since the thin Fe foil mass could be negligible compared with the mass of W, the C_p is 0.134 J/g K. For a plastic strain of 0.1, the temperature rise of the W/Fe/W sandwiched structure under DY loading is expected to be ~113 K.

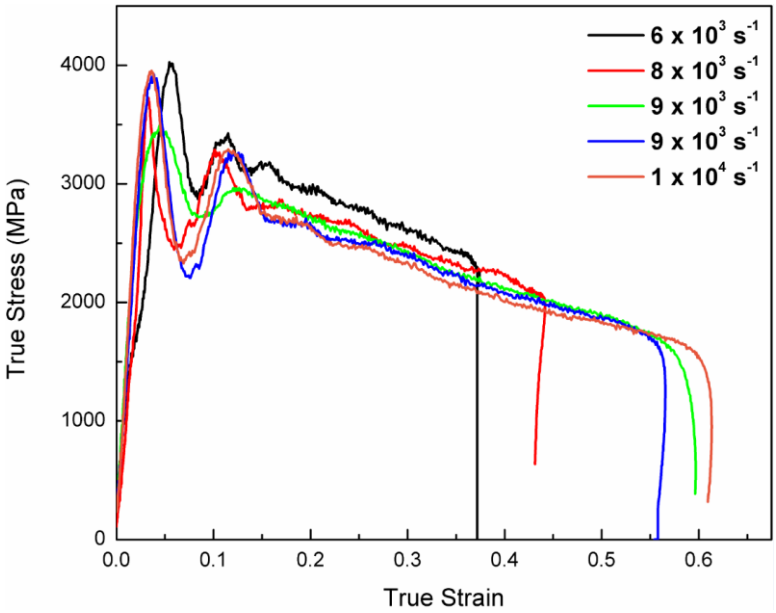

Figure 3.6: High strain rate true stress-strain curves under compressive load of sandwiched W/Fe/W structure at strain rate of ~6 × 10^3 s^{-1} to 1 × 10^4 s^{-1}. The last stress drops were caused by unloading.

3.1.5 Post-loading examinations

3.1.5.1 Optical microscopy/Scanning electron microscopy observations

Post-loading SEM images of the W/Fe/W sample at the strain rate of ~6 × 10^3 s^{-1} are shown in Figures 3.7 (c-f) while the SEM images of the same sample before loading are provided as Figures 3.7 (a) and (b). Before loading, the sandwiched structure is clearly seen in an overview image in Figure 3.7 (a) and the zoomed-in interface area is shown in Figure 3.7 (b). Under the applied strain rate as ~6 × 10^3 s^{-1}, the sample was loaded and a light colored shear band was formed on the left side of the sample in Figure 3.7 (c). Shear localization initiated from the left bottom corner of the specimen, propagated through the bonding area and, then reached to the other W layer. From a zoomed-in image in Figure 3.7 (d), the Fe interlayer only sheared to a minimum extent with the bonding remaining intact and exhibiting little localized delamination at ~6 × 10^3 s^{-1}. From Figure 3.7 (e) and (f) which are the zoomed-in images of areas A and B in Figure 3.7 (c), the Fe layer was

partially sheared inside the shear band. Those close-up views further confirm that the bonding was intact with little localized delamination at the bonding faces.

Post-loading SEM images of the W/Fe/W sample at the strain rate of ~8×10^3 s^{-1} are displayed in Figure 3.8. From Figure 3.8 (a), two significant shear bands at an angle of about 45° with respect to the loading direction are formed. A subsequent crack on the left band as a consequence of the severe shear localization can also be observed in a zoomed-in image in Figures 3.9 (b) and (c). The width of the shear band is ~100 μm after a rough measurement. Note, the Fe foil was sheared to failure inside the shear band, while the bonding interfaces at the surroundings are intact. The right shear band delaminated the bonding face between W and Fe and part of Fe foil was squeezed out of the plane.

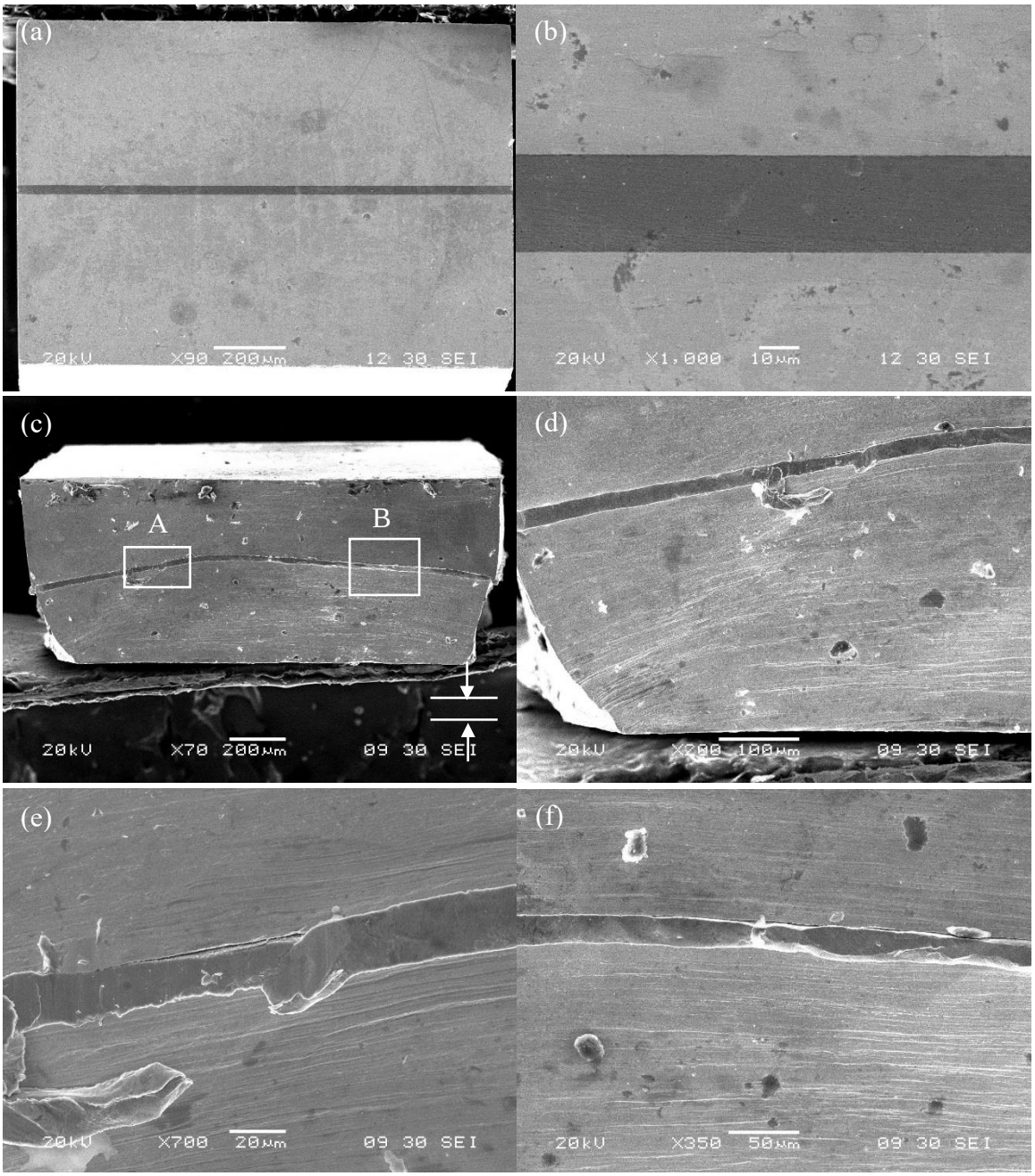

Figure 3.7: SEM images before high strain rate loading (a, b). Post-loading SEM images of the W/Fe/W sample at the strain rate of ~6×10^3 s^{-1} (c-f). Image (e) and (f) are the zoomed-in images of the areas A and B in image (c), respectively. Loading direction is indicated by arrows in images (c).

The adiabatic nature of the shear bands can be indicated by comparing the thermal conduction length scale over the time of the DY loading with the width of the shear band [46]. A simpler but closer estimate of the thermal conduction length scale is $\sqrt{2\alpha \cdot \Delta t}$,

where α is the thermal diffusivity of W (0.662 cm^2/s at room temperature and 0.226 cm^2/s at melting point) [46], and the Δt is the time elapsed during DY loading (~52 μs). As such, the estimate of the thermal conduction length scale is on the order of about 40 μm, which is smaller than the apparent shear band width (~100 μm). This suggests that the shear bands observed in this work are indeed adiabatic in nature.

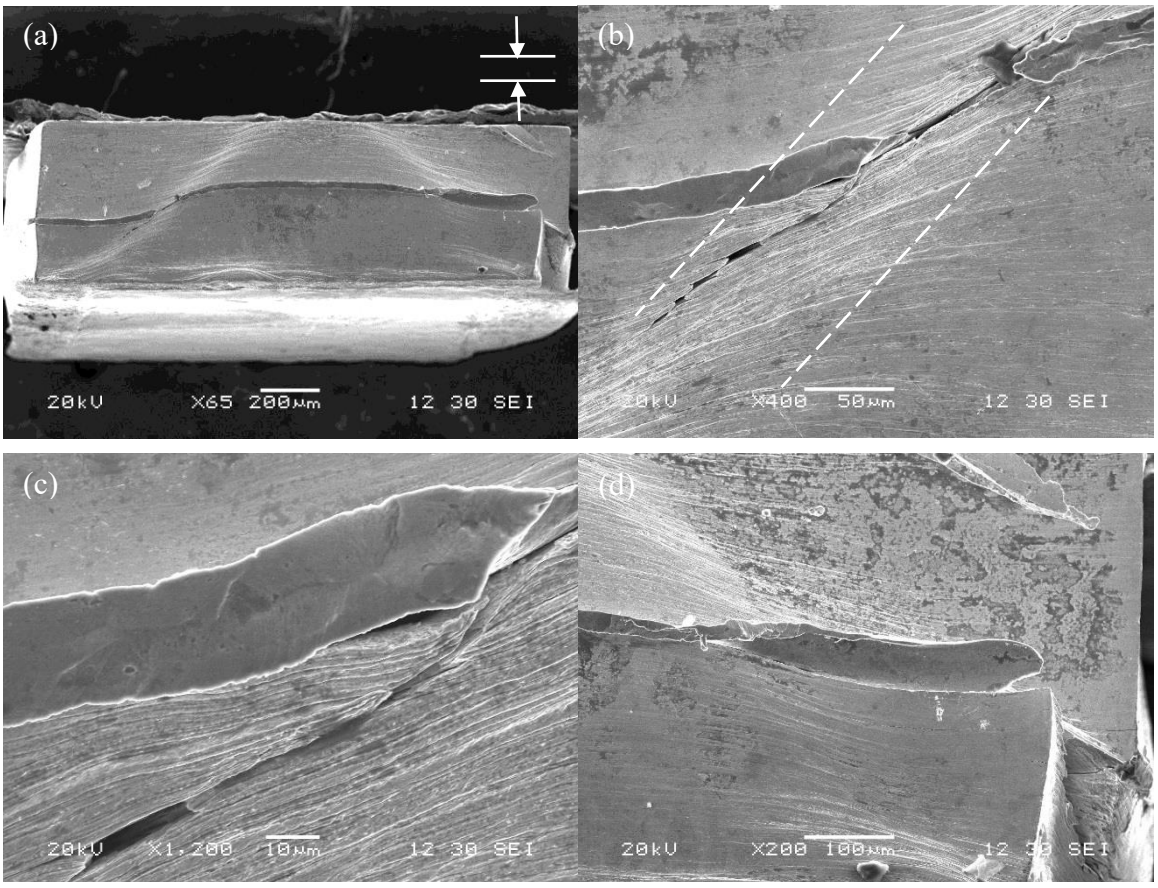

Figure 3.8: Post-loading SEM images of the W/Fe/W sample at strain rate of ~8×10^3 s^{-1} (a-d). The edges of the left shear band are highlighted by two dashed lines in (b). A close view of the Fe layer tip inside the left band (c). Shear band on the right with localized delamination (d). Loading direction is indicated by arrows in image (a).

The underlying morphology of the shear bands was revealed by polishing and Murakami's etching on the loaded sample (~8×10^3 s^{-1}) and is shown in Figure 3.9. Figure 3.9 (a) provides an overview optical micrograph of the ASB. The bright thin layer is the

Fe foil in-between two W sheets. The superficial crack and localized delamination of the as deformed surface were removed by mechanical polishing with two symmetric shear bands now being clearly seen. Figure 3.9 (b) and (c) are close-up views of the left and right shear bands, respectively. The Fe foil is sheared and thinned severely inside the band. The thickness of Fe foil within the band is ~4 μm while the thickness outside the band is ~14 μm, compared to the original thickness which is 25 μm. In other words, the thickness reduction of Fe foil inside and outside the shear band is 84 % and 44 %, respectively. Flow lines in Figure 3.9 (b) and (c) suggest a canonical structure which describes the ASB of W, where the flow lines bend down through the boundary into the band and then curve away on the other side forming an antisymmetric pattern [26].

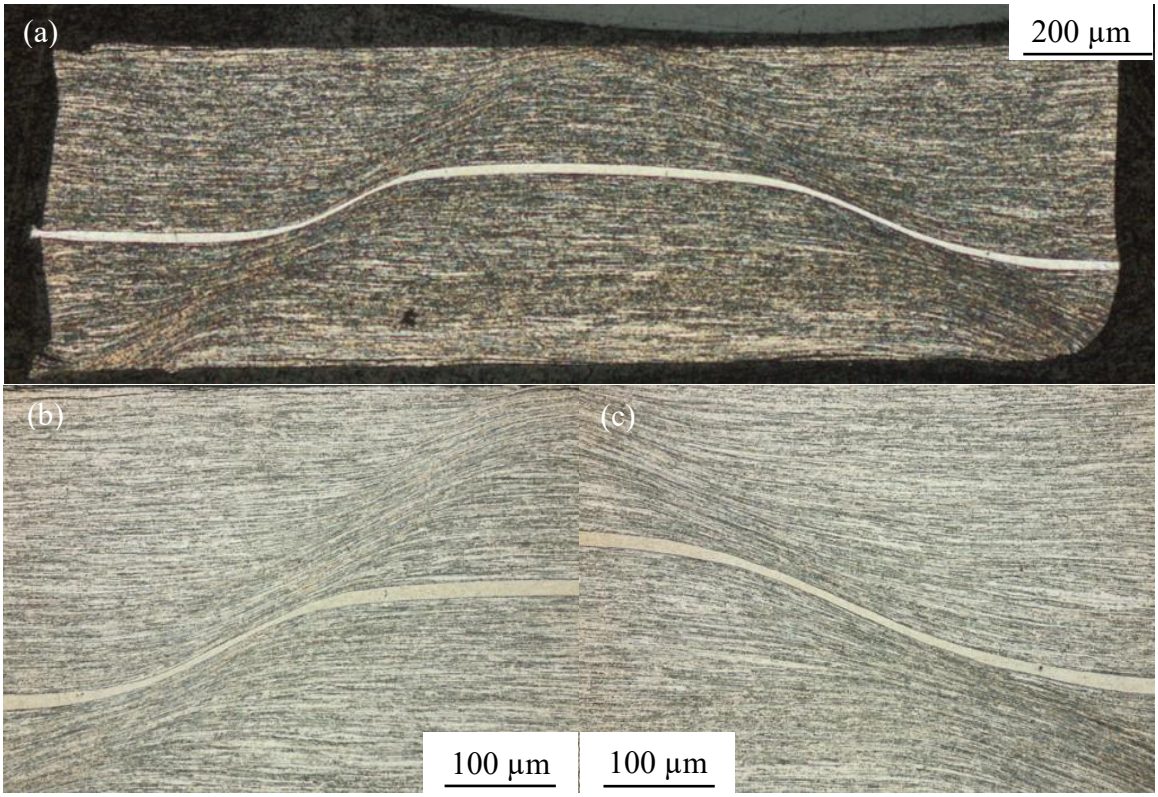

Figure 3.9: Optical micrographs of the ASB (~8×10^3) revealed by Murakami solution (a-c).

The morphology of ASB at higher magnifications is shown in SEM images in Figure

3.10. The interfaces between W and Fe are tightly joined around the shear band areas and even within the ASB. These shear bands with canonical structure do not show a very well-defined edge because the temperature rise would not have been sufficient to cause extensive recrystallization in W at the center of the ASB. However, recrystallization in Fe layer may be expected to see which is confirmed by TEM images.

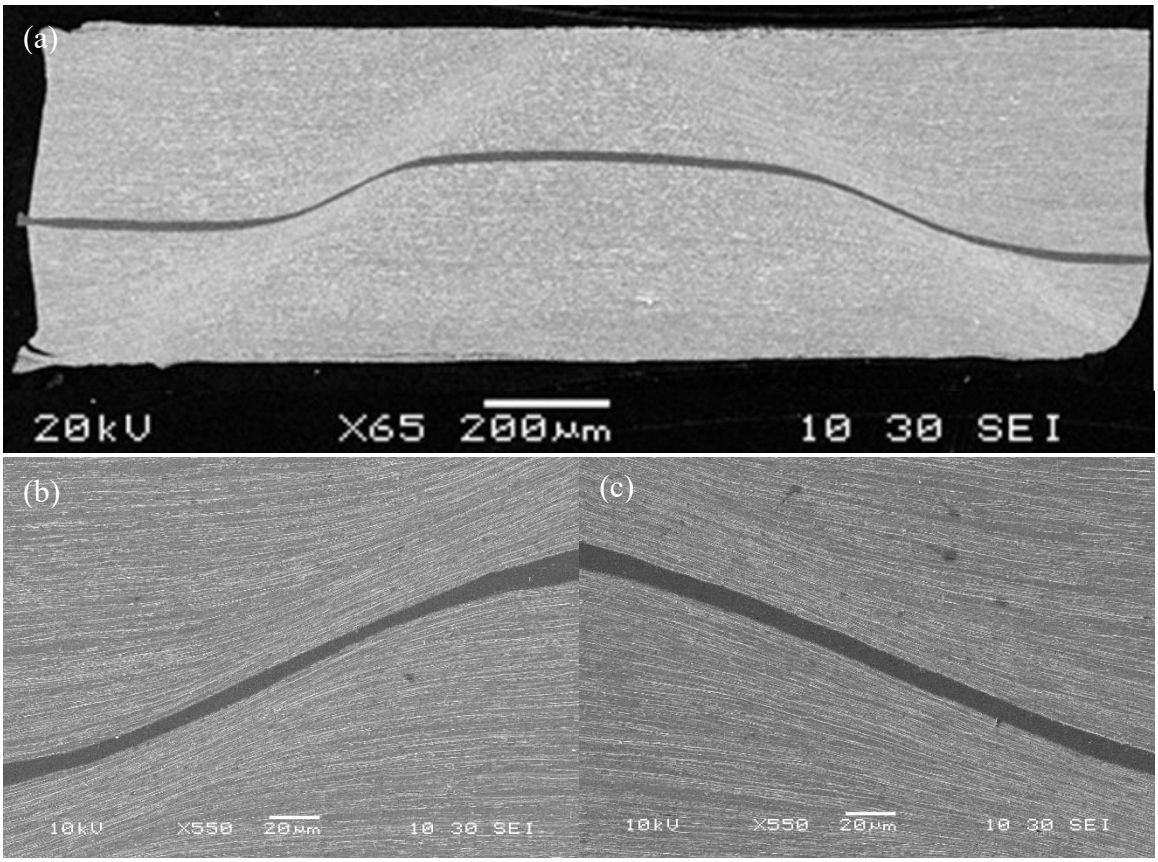

Figure 3.10: SEM images of ASB (~8×10^3 s^{-1}) revealed by Murakami solution (a-c).

The reason for triggering ASB at high strain rate is that the thermal softening overcomes the strain hardening and strain rate hardening. As such, it is necessary to evaluate the adiabatic temperature rise within the shear bands. As discussed in previous context, the temperature rise of the whole sample was calculated to be about 113 K when the compressive strain was 0.1 and flow stress was 3250 MPa. While within the shear band,

the angle between the Fe layer or the flow lines outside and inside the shear band is measured to be about 40°, i.e. the shear strain within the band is calculated to be 0.84. From Eq. (1.4), when the shear stress is about 1600 MPa, the temperature rise inside the shear band was calculated to be ~467 K. However, this calculation could still underestimate the temperature rise inside the shear band, which will be discussed in the next subchapter.

3.1.5.2 Transmission electron microscopy observations

With the intention of further studying the microstructure of the sandwiched W/Fe/W sample before and after high strain rate loading, TEM examinations were performed on the bonded sample and the high strain rate tested sample. Figure 3.11 (a) is a BF TEM image at the bonding interface before high strain rate loading. The top light part with three grains inside is the Fe layer, whereas the bottom darker region is the W layer with multiple elongated grains. There is a gap at the W/Fe interface which could be attributed to a localized area of insufficient bonding pressure. However, this localized gap should not affect the stress wave propagation or the strength of the bonding according to the results in the context of the previous discussion.

From Figure 3.11 (a), the Fe grain size is larger than 2 μm at minimum because of the grain growth during bonding. The elongated W grain structure introduced by rolling is also shown in the image. The interior of the W grains is clean with few dislocations being observed. The reason could be explained that during the diffusion bonding process at 1073 K, the bonding temperature annihilates the dislocations that were introduced by the SPD and the one hour bonding contributes to the possible Fe grain growth. Figure 3.11 (b) is the EDX map which shows that Fe (red) and W (green) atom cross the interface during bonding. An overlapped region formed at the interface is zoomed-in in Figure 3.11 (c). The

overlapped region at the interface further demonstrates the inter-diffusion at the interface.

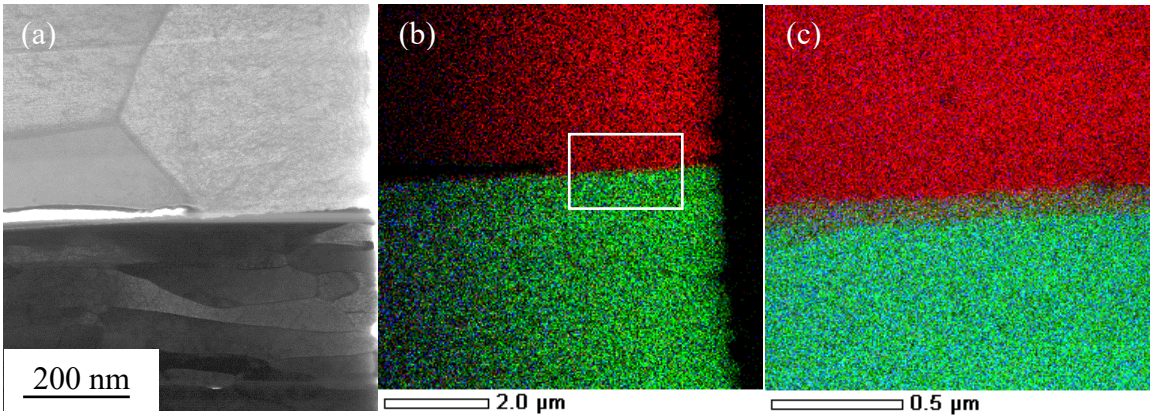

Figure 3.11: TEM BF image of the W/Fe/W sample as bonded (a). EDX mapping shows that Fe (red) and W (green) atoms across the interface during bonding (b). An overlapped region formed at the interface in the zoomed-in image (c)

Another TEM observation from the bonded sample is revealed in Figure 3.12. A strip of suspected intermetallic phase at the interface with a width of ~100 nm was observed and displayed in the BF image in Figure 3.12 (a). From the corresponding DP in Figure 3.12 (b), the Fe_2W phase was identified and marked in red. The DF image from the selected spot in Figure 3.12 (d) indicates the formation of Fe_2W phase. One can say that under this bonding condition, Fe_2W intermetallic phase forms, but it does not continuously exist along the W/Fe interface. The width of the Fe_2W phase is ~100 nm. The existing small amount of intermetallic compound would have a positive effect on strength the bonding face. However, excessive intermetallic phase formation could lead to a brittleness at the interface and impede the stress wave propagation.

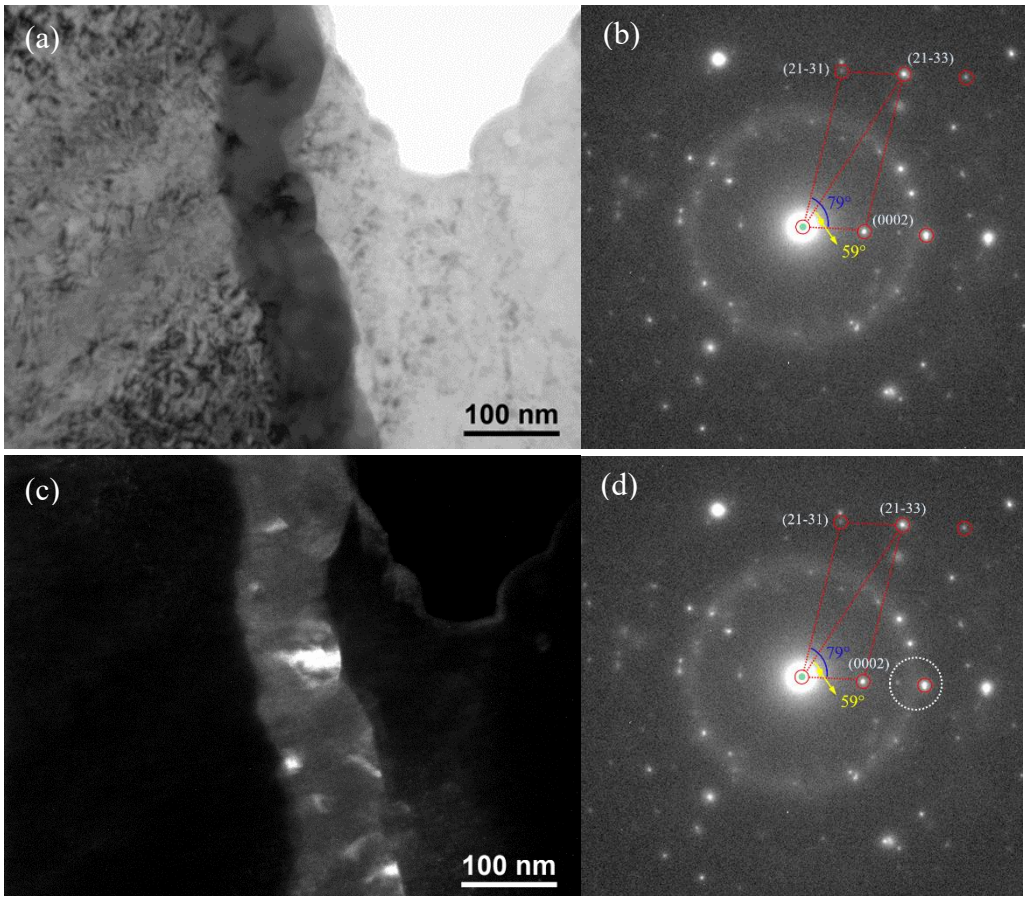

Figure 3.12: TEM BF image of the W/Fe/W interface (a) and corresponding diffraction pattern (b). DF image (c) from the selected spot in (d) indicates the formation of Fe_2W intermetallic compound.

Figures 3.13 (a-f) are the TEM results from the specimen tested at 8×10^3 s^{-1}. The TEM sample is from the location away from ASB. A BF image and SADP of the bonding face are shown in Figures 3.13 (a) and (b) with the dark bottom part being W and the bright top part being Fe in Figure 3.13 (a). A few gaps at the interface are visible between the W and the Fe asperities with a gap width of ~150 nm, which were probably introduced by mechanical polishing. The gaps between the W and the Fe asperities could have been closed by the bonding pressure. The corresponding SADP is displayed in Figure 3.13 (b) with an identifiable Fe DP. W and possible intermetallic phase are not identified in the DP.

The TEM BF image and SADP of W and Fe regions of the sample tested at 8×10^3 s^{-1}

are shown in Figures 3.13 (c, d) and (e, f), respectively. From Figure 3.13 (c), the W grains outside the shear bands also display the characteristic elongated morphology. Moreover, a large number of dislocations are trapped inside the W grains as well as accumulated near the W grain boundaries upon a compressive strain of ~0.43. The corresponding SADP of the W region and its identified DP is shown in Figure 3.13 (d). The BF image of Fe at 8×10^3 s^{-1} is presented in Figure 3.13 (e) showing a totally different grain morphology compared to those after bonding in Figure 3.11 (a). Due to the SPD at high strain rates, an excessive number of dislocation cells appears inside the Fe grains in Figure 3.13 (e).

The microstructure inside the ASB should display different features compared to those after bonding and outside the ASB if the shear strain and temperature rise are considered. The shear strain inside the ASB was ~0.84 and temperature rise within the band was calculated to be ~467 K for the W/Fe/W sample at 8×10^3 s^{-1}. Since the temporal scale of the shear deformation is much shorter than that of heat conduction, 90 % of the heat converted from plastic deformation was confined within the band. Because of the extreme small loading duration which was ~52 μs, the Fe grains inside ASB could undergo recrystallization if the temperature rise is high enough and then is suddenly quenched by the surroundings as the global temperature rise was only ~113 K.

Figure 3.14 provides the TEM BF images and SADPs of the W/Fe/W sample at ~8×10^3 s^{-1} but inside ASB. The W/Fe interface inside the ASB and its SADP are shown in Figures 3.14 (a) and (b). At the interface region, no asperity or gap can be observed and it is possible that the severe shear stress forces the gap to close. From the SADP in Figure 3.14 (b), both of the W and Fe DPs can be identified. However, no intermetallic phase DP is identified in Figure 3.14 (b). This could be explained that the amount of intermetallic

compound (Fe_2W or FeW) is too small to appear in the DP or does not exist in the selected area in Figure 3.14 (a).

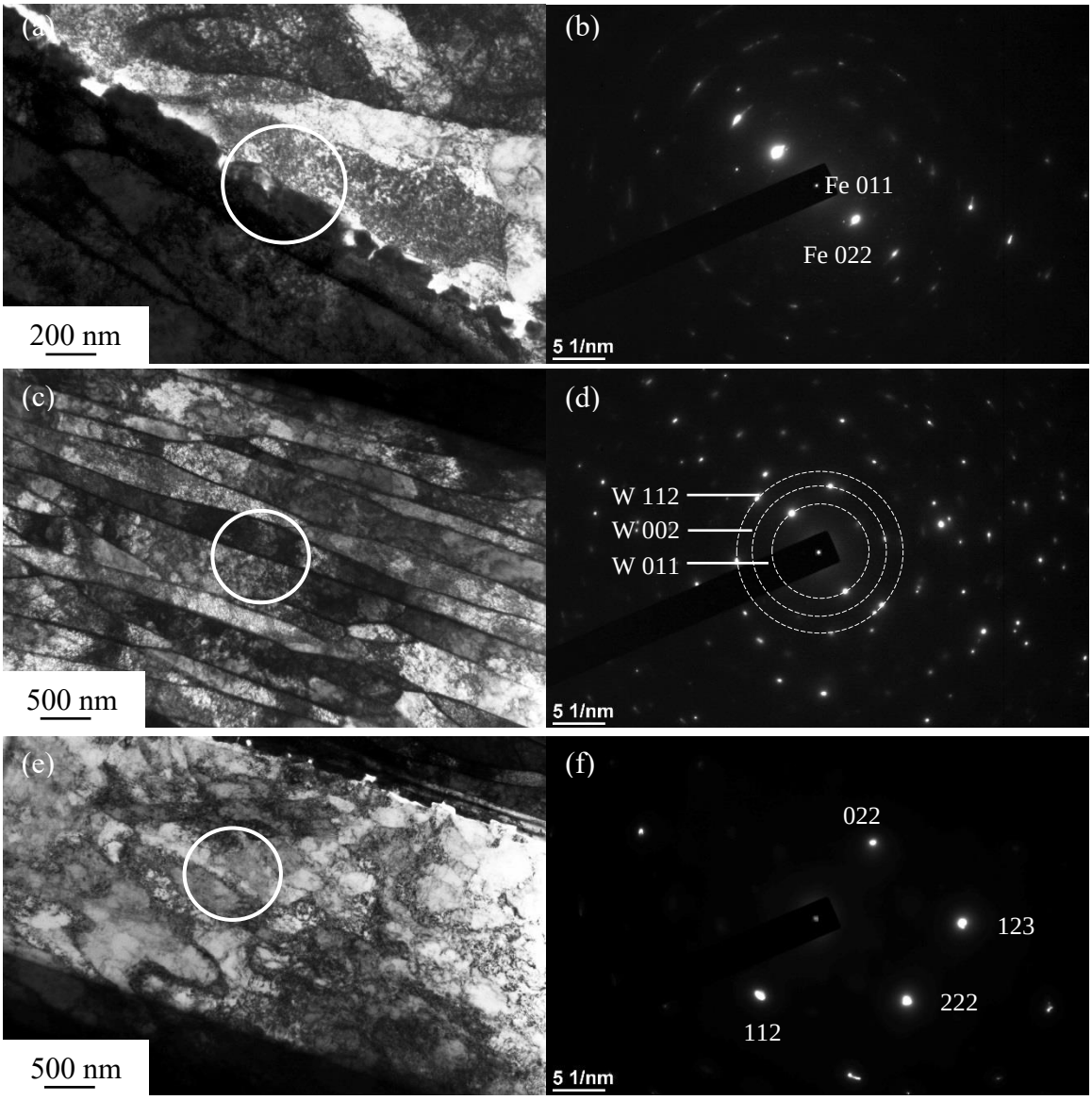

Figure 3.13: TEM BF image (a) and SADP (b) of the W/Fe/W sample interface. TEM BF image (c) and SADP (d) of W part. TEM BF image (e) and SADP (f) of Fe part. The strain rate was~8×10^3 s^{-1} and the TEM sample is from the location that outside ASB.

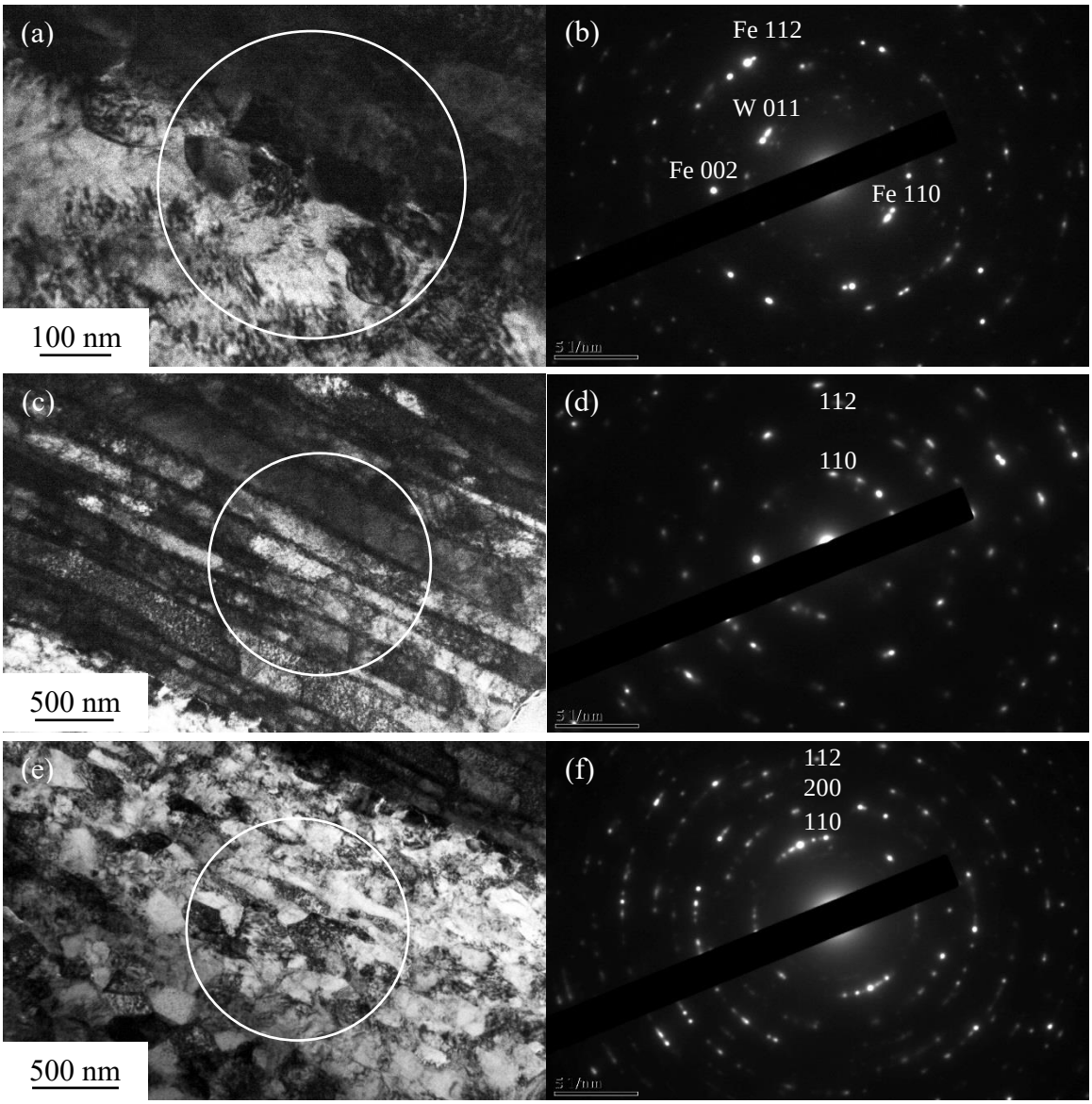

Figure 3.14: TEM BF image (a) and SADP (b) of the W/Fe/W sample interface. TEM BF image (c) and SADP (d) of W part. TEM BF image (e) and SADP (f) of Fe part. The strain rate was~8 × 103 s-1 and the TEM sample is from the location that inside ASB.

As for the W region in Figure 3.14 (c), the W grains with the ASB are totally developed into a layered structure with a width of each layer of ~200-300 nm. Thick dislocation walls establish upon loading which is consistent with previous research [153]. The SADP of the W region in Figure 3.14 (d) displays an approximate diffraction halo which confirms a smaller grains of W inside the ASB. Moreover, a significant change is observed in Figure

3.14 (e) where the Fe grains are refined into NC regime. The Fe grain size is ~100-200 nm compared to its ~4 μm CG counterpart before loading. The DP of Fe part in Figure 3.14 (f) shows the shape of rings which further confirms its NC grain structure inside the ASB. It is the temperature rise within the band recrystallized the Fe grains during a short loading time frame and then the grains were quenched by the surroundings. The temperature rise inside the ASB was calculated to be ~467 K while the Fe recrystallization temperature should be ~888 K for its melting temperature is 1811 K. One could say that the calculation underestimates the temperature rise within the ASB in this scenario.

3.2 Three-layer structure (V interlayer)

3.2.1 Microstructural analysis

In the W/Fe/W system, ASB was demonstrated to propagate through the heterogeneously layered structure upon high rate loading. The Fe foil, as the interlayer in between W sheets, plays a role of bonding the rolled W sheets together into an integral structure. It is encouraging that the Fe interlayer facilitates the formation of intact bonding faces and the W/Fe/W structure also survived the high rate loading with ASB being observed. This heterogeneous structure that has ASL under high rate loading could be optimized in terms of different interlayer materials as well as bonding conditions. A W/V/W structure with a V foil sandwiched between two adjacent W layers was fabricated and studied in this section to evaluate if the ASB/ASL propagation is universal in the heterogeneous layered structure. Moreover, there should be no intermetallic phase formation in the W/V/W layered system according to the isomorphous phase diagram in Figure 1.6, which is favorable to form an intimate contact and wave prorogation upon high strain rate loading.

Two tight junctions between the W and V contact surfaces were formed during diffusion bonding and one of the interfaces is displaced in Figure 3.15 (a). Ten point elemental concentration analyses were conducted across the W/V bonding face from the left end (point A) to the right end (point B). Figure 3.15 (b) shows the concentration profile with the horizontal axis being the distance and the vertical axis being the chemical composition. The gradual concentration decreases or increases at the interface region for either W or V indicating that a mutual atomic diffusion occurred at the interface region. Table 3.3 displays the elemental concentration from point A to B in weight %. From Table 3.3, the V concentration at point A (within W) is 0.62 % and increases to 1.44 % when it is ~1.5 µm away from the interface. However, the concentration of W atoms in the V matrix is much higher than V atoms in W matrix. Similar to that observed in the W/Fe/W system, W atoms are easier to diffuse into V than V into W.

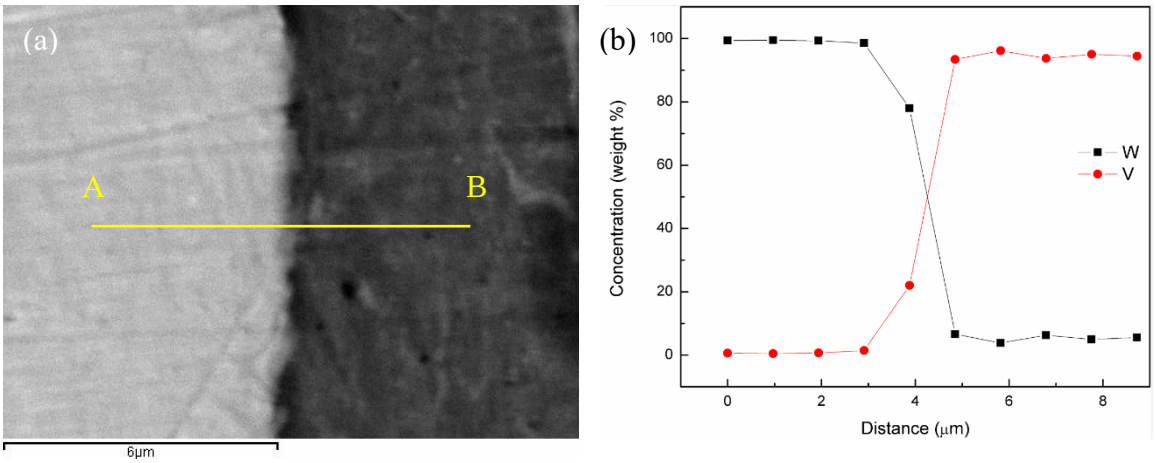

Figure 3.15: SEM micrograph of an Fe/V interface with a yellow line indicating the positions of ten point EDX analyses (a). Point A (spectrum 1 in Table 3.3) is at the left end of the yellow line while point B (spectrum 10 in Table 3.3) is the tenth point at the right end. The distance between each point is ~1 µm. Elemental concentration profile of W and V along the interface (b). Darker area on the right in image (a) is the V part while lighter part on the left is W part.

Table 3.3: Element concentration from A to B in weight % in Figure 3.15 (a).

Spectrum	V	W	Total
Spectrum 1	0.62	99.38	100.00
Spectrum 2	0.51	99.49	100.00
Spectrum 3	0.7	99.3	100.00
Spectrum 4	1.44	98.56	100.00
Spectrum 5	22.01	77.99	100.00
Spectrum 6	93.39	6.61	100.00
Spectrum 7	96.16	3.84	100.00
Spectrum 8	93.73	6.27	100.00
Spectrum 9	95.04	4.96	100.00
Spectrum 10	94.44	5.56	100.00

3.2.2 High strain rate compressive mechanical properties

The uniaxial high strain rate true stress-strain curves of the W/V/W structure at various strain rates (~6×10^3 s^{-1} to 7×10^3 s^{-1}) are shown in Figure 3.16. The peak flow stress has reached ~3500 MPa at a strain rate of ~7×10^3 s^{-1}. One should note that the samples indicated by black and blue traces were tested by a shorter 76 mm striker bar and samples indicated by green and red traces were tested by a longer 127 mm striker bar. Since the length of the sticker bar is linearly proportional to the deformation of the sample, there will be a strain variation at the same strain rate. Significant flow softening has been observed in the stress-strain curves, which was also observed in the W/Fe/W system results. Hence, the flow softening phenomenon that proceeds ASB is not unique to the W/Fe/W system only, but also universal for any heterogeneous layered structure of W/M/W, M being the interlayer metal. Due to adiabatic heating, the global temperature rise in the sample could be calculated using Eq. (1.4) and the global temperature rise is calculated to be ~181 K when the plastic strain is 0.1.

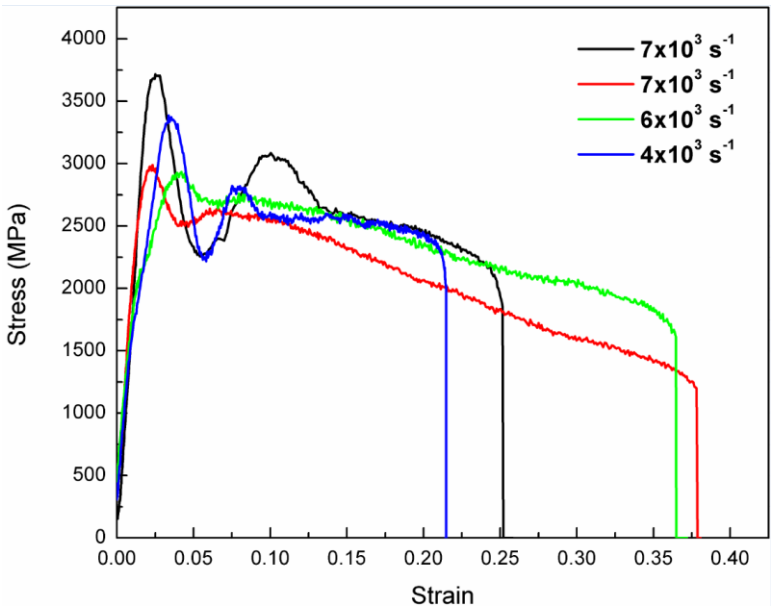

Figure 3. 16: High strain rate true stress-strain curves under compressive load of sandwiched W/V/W structure at strain rate of ~4 × 103 s-1 to 7 × 103 s-1. The last stress drops were caused by unloading.

3.2.3 Post-loading examinations

Post-loading SEM examinations of the W/V/W sample at the strain rate of ~6×10^3 s^{-1} are displayed in Figure 3.17 (b-f). Figure 3.17 (a) is a SEM image the W/V/W structure before DY loading where a 75 µm thick V layer is in between two rolled W sheets. From Figure 3.17 (b), a primary shear band developed on the left of the sample at an angle of ~45° with respect to the loading direction which is displayed at the top right of the image. A deep crack with a width of ~10 µm runs through the left shear band as a consequence of the severe shear strain gradient that accumulated inside the band and outside the band. The occurrence of the shear band and subsequent crack cross these heterogeneous layers demonstrate the propagation of the stress wave through the inhomogeneous structure without impediment. From the zoomed-in image in Figure 3.17 (c), it can be seen that the V foil is completely sheared into two inside the band. The flow lines of the ASB are clearly observed in Figures 3.17 (d-f) demonstrating the typical canonical structure.

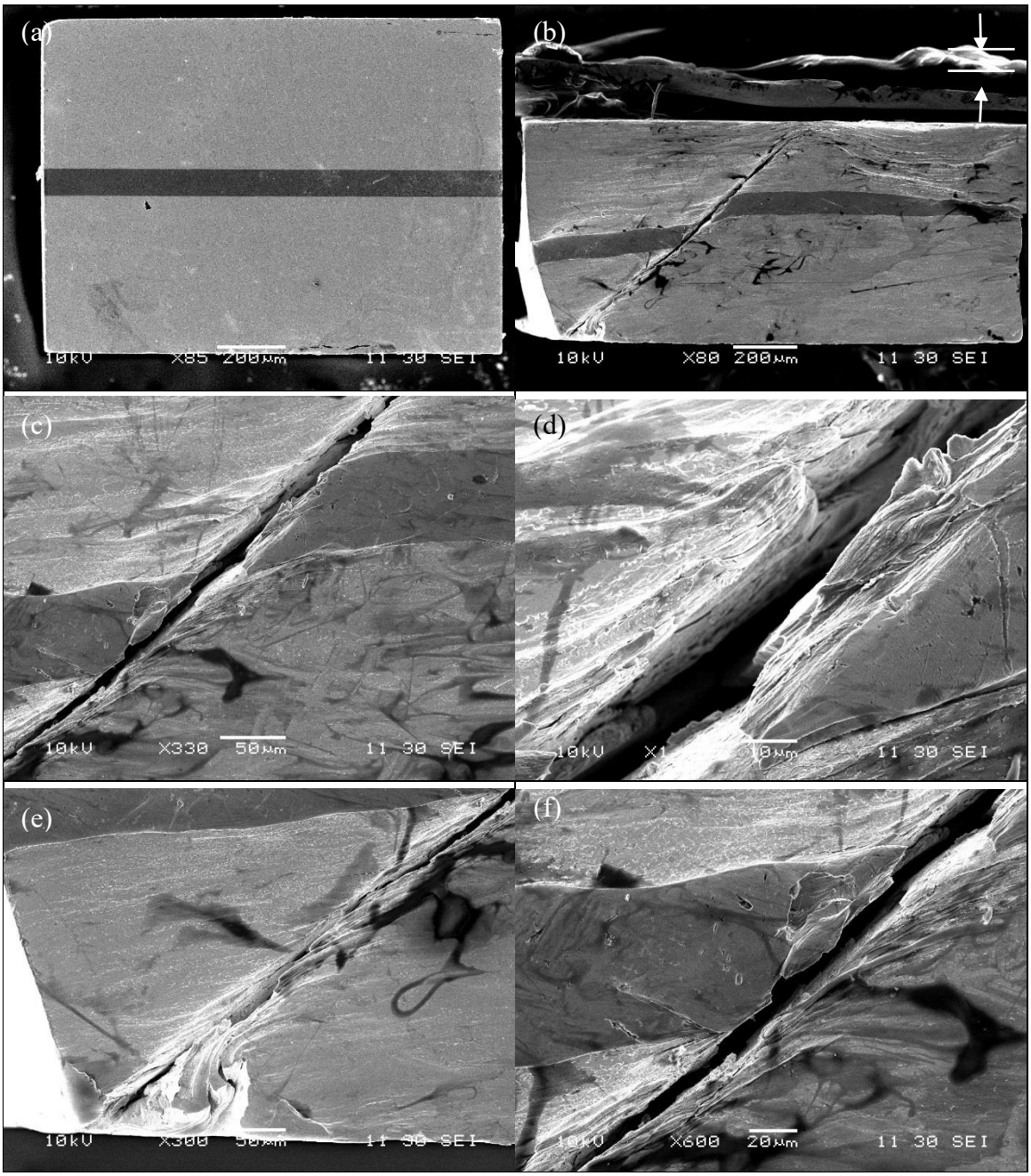

Figure 3.17: SEM image of the W/V/W sample after bonding (a). Post-loading SEM images of the sample at the strain rate of ~6×10^3 s^{-1} (c-f). Images (c-f) are the zoomed-in images of image (b). Loading direction is indicated by arrows in image (b).

Figures 3.18 (a-d) depict the morphology of ASB under SEM after mechanical polishing and etching. The superficial crack was removed during polishing and the primary ASB is shown in Figure 3.18 (a). The V interlayer is sheared within the band but still intact upon

high rate loading. From a close-up view of the interface region in Figure 3.18 (b), the V layer is sheared heavily within the band with a thickness reduction of about 86 % compared to its original thickness of 75 μm. The bonding faces remain integral and no obvious delamination between W and V is observed at the interfaces. The width of the shear band is ~100 μm and the band is adiabatic in nature if considering the characteristic heat conduction length which is ~ 40 μm. The typical canonical structure is also clearly revealed in Figure 3.18 (c, d).

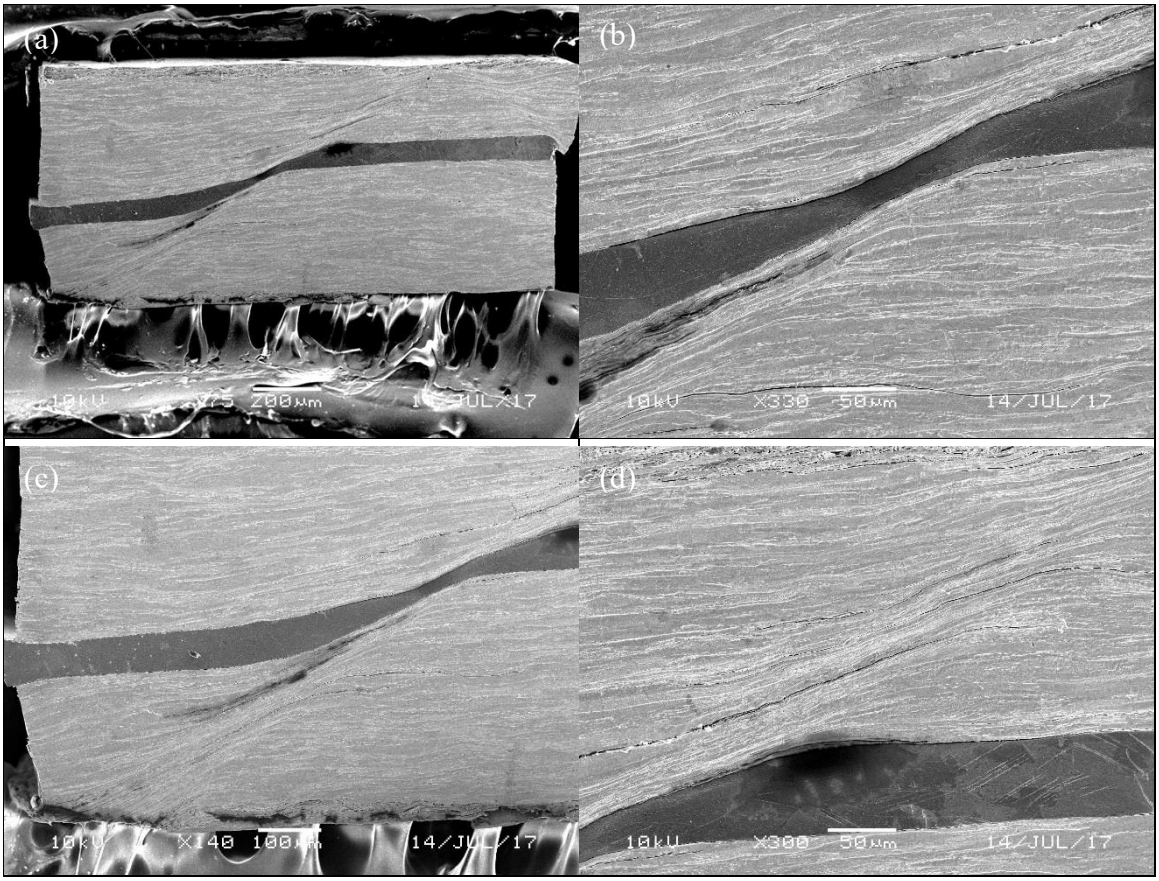

Figure 3.18: SEM images of an ASB morphology in W-V-W system tested under strain rate of about 6×10^3 s^{-1} (a-d). The sample was revealed by standard Murakami solution.

3.3 Conclusions

Three-layer inhomogeneous structures, W/Fe/W and W/V/W, were fabricated using rolling and diffusion bonding, which were then investigated comprehensively in the aspects

of microstructure examination and mechanical properties analysis. The observed flow softening as well as the occurrence of ASB demonstrate that these structures are ASB susceptible materials. Moreover, the bonding interfaces, W/Fe and W/V, remain intact upon high rate loading with localized delamination being observed only at the interface.

Low homologous temperature rolling and diffusion bonding were used to create the three-layer structures of, W/Fe/W and W/V/W. The bonding interfaces of W/Fe and W/V were examined under OM, SEM and TEM. No void or delamination was observed after bonding. The W grains in the W/Fe/W structure display an elongated microstructure with a width of 5-10 μm which was introduced by low homologous rolling. During diffusion bonding, dislocations that were introduced by rolling were annihilated and the interior of W and Fe grains were clean after bonding.

Inter-diffusion between W and Fe (V) across the bonding interfaces occurred during diffusion bonding. This inter-diffusion is a prerequisite for developing a tightly bonded and strong interfaces. W atoms have a higher ability to diffuse into the interlayer materials in the three-layer structure because W belongs to refractory metal category and it has a stable atomic bonding at 1073 K. According to the nanoindentaion results, no significant hardness increase has been observed at the interface, which indicates that no excessive amount of intermetallic compound has formed during diffusion bonding.

Upon DY compressive loading, the stress-strain curves of the W/Fe/W and W/V/W samples display significant flow softening. The peak flow stress of the W/Fe/W sample reached ~4000 MPa at a strain rate of ~ 8×10^3 s^{-1}. The peak flow stress of the W/V/W sample reached ~3500 MPa at a strain rate of ~7×10^3 s^{-1}. ASBs as well as cracks have been seen on the cross-sectional surface of the W/Fe/W and W/V/W samples upon high

rate loading. The width of the ASB was identified as ~100 μm. At a plastic strain of 0.1, the global temperature rise of the W/Fe/W sample at 8×10^3 s^{-1} was calculated to be ~113 K while the temperature rise inside the band was conservatively calculated to be ~467 K.

After bonding, the W grains in the W/Fe/W system show an elongated structure with few dislocations being observed inside the grains. However, an excessive numbers of dislocations accumulated within the grains after high rate compression. Inside the ASB, thick dislocation walls formed in the W layer, leading to a laminar structure.

The Fe grains after bonding grew into a CG structure with dislocation annihilation during this process. The Fe grains outside of the shear band after loading were severely deformed with dislocation walls and sub-grains being seen due to the SPD. However, the Fe grains inside the ASB were recrystallized and refined to the NC regime with an average grain size of ~100-200 nm, which is attributed to the sudden temperature rise and drop inside the band.

CHAPTER 4: W/FE/W BULK SAMPLES AND BALLISTIC PERFORMANCE.

4.1 Multi-interlayer structure

The three-layer sandwiched structures (W/Fe/W and W/V/W) were comprehensively investigated to study aspects of their microstructure and mechanical properties, demonstrating the university of ASB in such heterogeneously stacked structures. This phenomenon indicates that the heterogeneously stacked structure favors stress wave propagation under high rate loading conditions. Therefore, the three-layer sandwiched structures meet one of the prerequisites of being a KE penetrator materials-occurrence of ASB under high rate loading. However, the three-layer structure after diffusion bonding is a two-dimensional material with a thickness of only ~1-2 mm, which could not be used to fabricate a three-dimensional subscale or prototype KE penetrator. Based on the positive experimental results from the three-layer structures, a thicker four Fe interlayers sample and a much thicker multi-interlayer bulk material were studied under high rate loading conditions and a ballistic experiment, respectively, to investigate the effect of thickness scaling on ASB.

4.1.1 Microstructure and atomic diffusion

A sample including four Fe foils and five W layers was prepared by diffusion bonding and then EDM machined into cubes with dimensions of ~2.5 mm × 2.5 mm × 2 mm for the following high rate testing. One of the high rate testing samples is shown in Figure 4.1. The five thick layers are W layers with a thickness of ~400 μm. The four thinner Fe layers are in between the W layers with an individual thickness of ~25 μm. After bonding, the interfaces are intact with no obvious void or delamination being observed under an optical microscope.

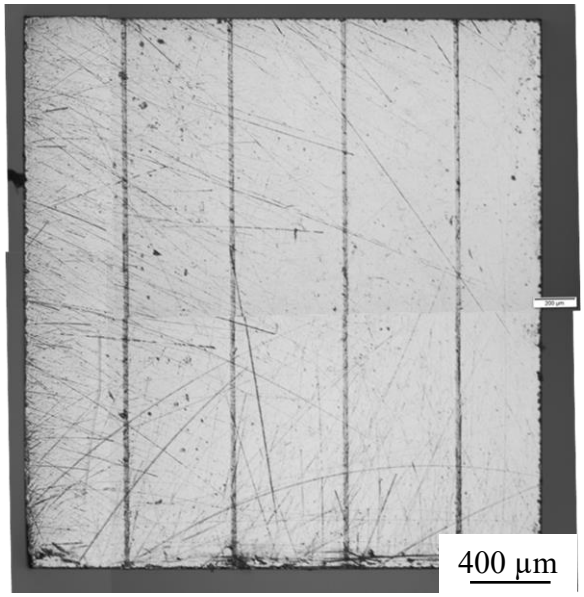

Figure 4.1: Montage of the optical micrographs of four-interlayer (Fe) sample before high rate testing.

Figures 4.2 (a-d) are the bonding face investigation results using EDX line scan along the W/Fe interfaces. The scanning path is shown in each image as a yellow line with a length of ~12 µm. At the four bonding interface locations, the interfaces are intact with closed asperity gaps between the W layer and Fe foil. A few voids that are observed inside the Fe foil could have been introduced during the manufacturing process. At each of the bonding faces, the concentration gradients from W atoms and Fe atoms are displayed in Figure 4.2. This concentration gradient is consistent with the analysis result from the three-layer structure. The concentration gradient at each interface indicates the occurrence of coupled diffusion taking place between W and Fe at the interfaces, which facilitated the formation of tightly bond interfaces. In other words, this scale-up experiment proves that diffusion bonding can also be used to fabricate a much larger multi-interlayer sample.

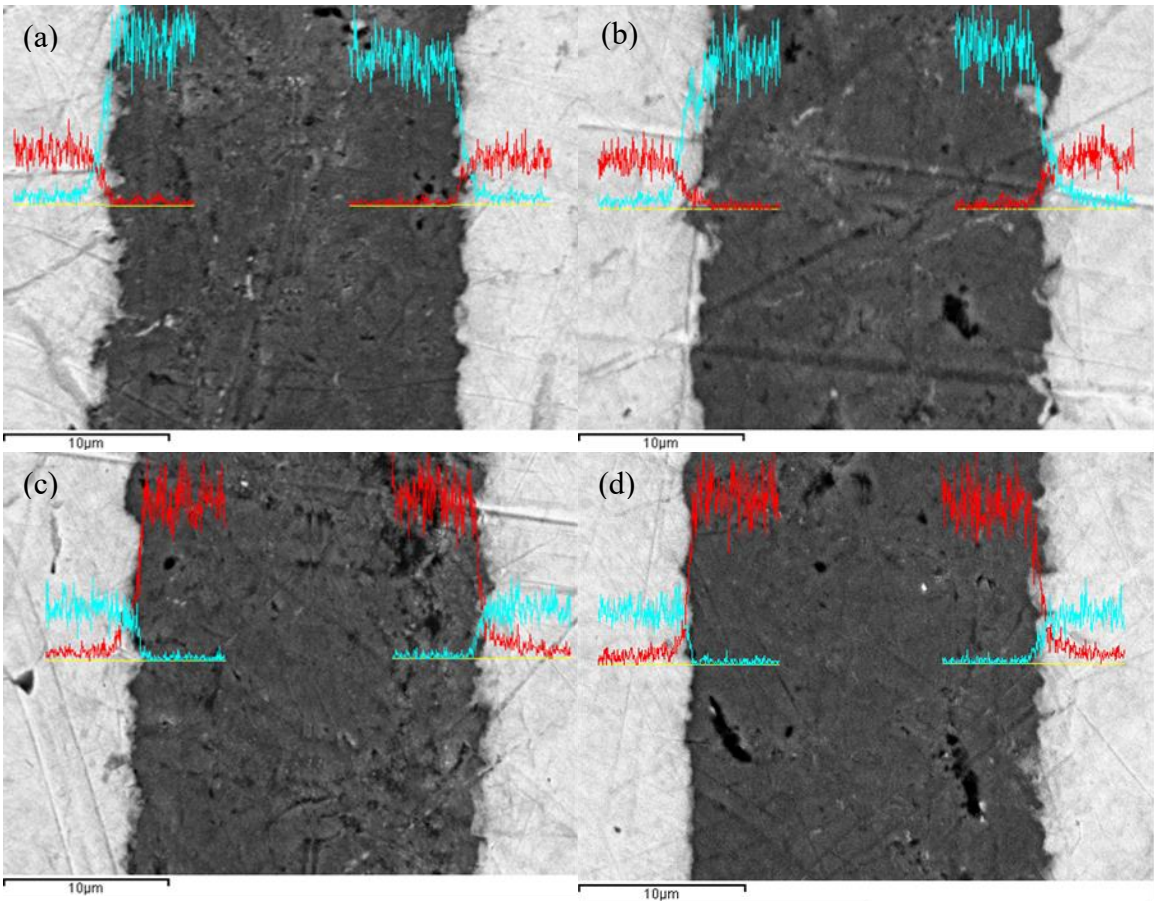

Figure 4.2: EDX line scan of a four-interlayer (Fe) sample at the W/Fe bonding faces. Yellow line in each image indicates the line scan path across the interface. W and Fe atom counts are displayed in red and blue in (a, b) while vice versa in (c, d). The wide black strip in the middle of each image is the Fe foil.

4.1.2 High strain rate mechanical properties

High strain rate uniaxial true stress-strain curves of the four-interlayer structure under various strain rates are displayed in Figure 4.3. The sample cubes after EDM cutting were loaded at strain rates from ~3×10^3 s^{-1} to 4.5×10^3 s^{-1}. The peak flow stress has reached a value near ~2750 MPa at a strain rate of ~4.5×10^3 s^{-1}. Due to the limitations of the applied strain rate, the loading strain rate could not reach closer to those of the earlier sandwiched structures. In order to observe the flow lines clearly, a sample was loaded twice and is shown in green and blue in Figure 4.3. From the high strain rate stress-strain curves of the

multi-interlayer samples, a profound flow softening is also observed as a prerequisite of occurrence for ASB. The adiabatic temperature rising in the multi-interlayer sample at 4.5 × 10^4 s^{-1} was calculated to be ~84 K at the strain of 0.1.

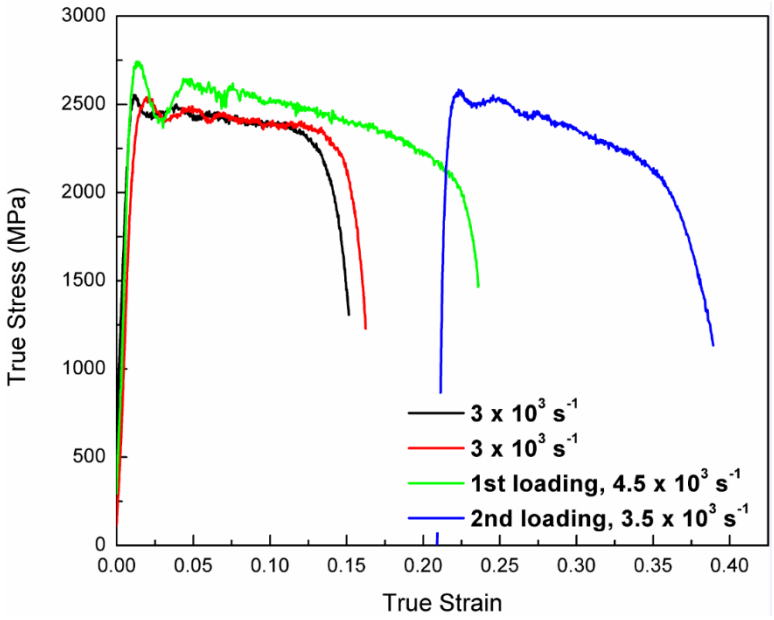

Figure 4.3: High strain rate true stress-strain curves under compressive load of four-interlayer samples at strain rate of ~3 × 10^3 s^{-1} to 4.5 × 10^4 s^{-1}.

4.1.3 Post-loading examinations

Figure 4.4 and 4.5 reveal the post-loading SEM images of the sample at ~4.5 × 10^3 s^{-1} (first loading) and ~ 3.5 × 10^3 s^{-1} (second loading). The four black thin layers in image (a) are the Fe foils. The top and bottom W layers are thinner than the other three W layers which was due to the more severe mechanical polishing. Under the first loading, the sample was loaded to a strain of ~0.24 with multiple light shear bands appearing in Figure 4.4 (a). Those shear bands propagate through the four Fe interlays and the five W layers along the sample diagonal upon high rate loading, demonstrating the possibility of ASB development not only in a sandwiched structure, but also in this thicker multi-interlayer sample or even bulk materials.

Close up views of areas A, B and C in Figure 4.4 (a) are shown in Figures 4.4 (b), (c) and (d), respectively. In Figure 4.4 (b), a shear band propagates through W and Fe and shears the Fe foils in a way of necking. The bonding faces inside and near the band are still intact upon loading. From Figure 4.4 (c), a crack at the W/Fe interface develops within the band and propagates into the W layer. Typical shear band flow lines are clearly observed in Figure 4.4 (d) with a width of ~100 μm and the morphology of shear band is similar to those developed in the three-layer structure. However, after the first loading, the shear bands are not as confined and defined as the ones in the sandwiched structure at 8×10^3 s^{-1}. This could be attributed to the lamination in the applied strain rates that were determined by the sample gauge length and the geometry of the SHPB.

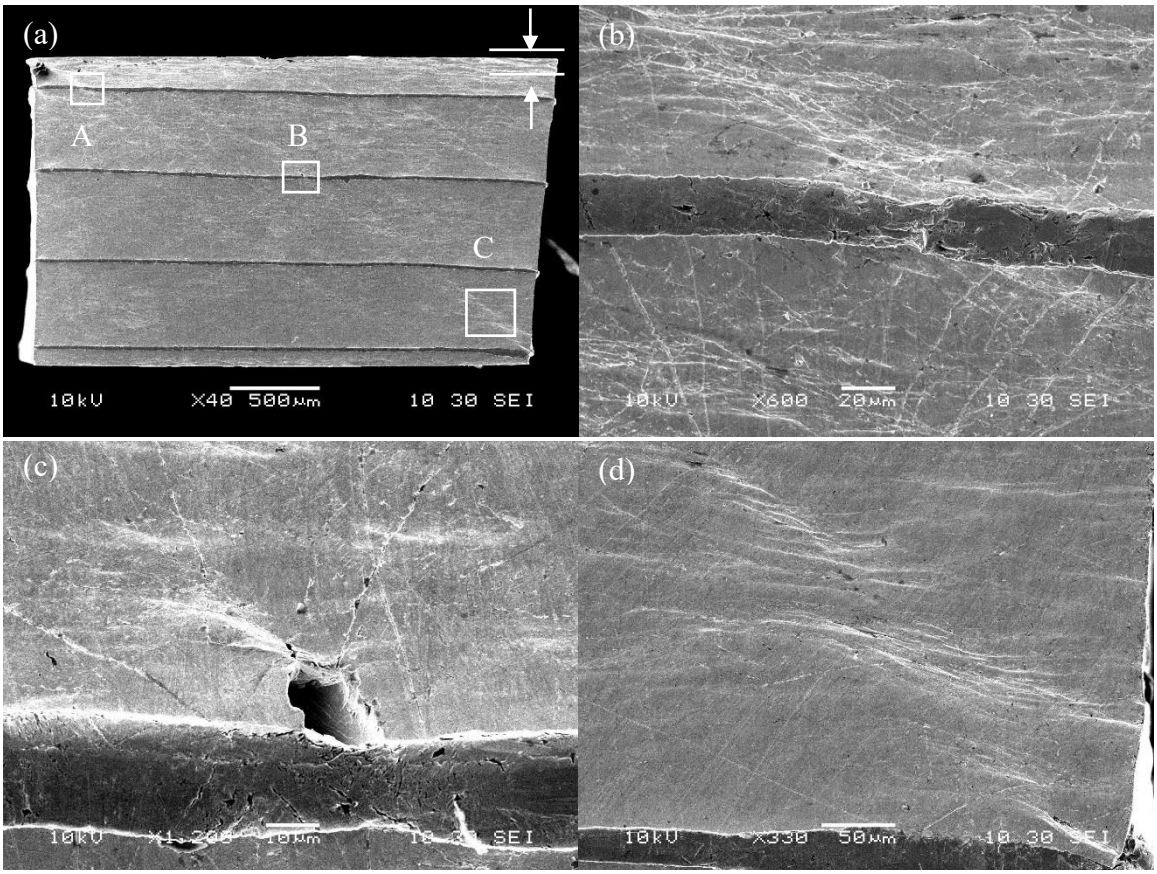

Figure 4 4: Post-loading SEM image of a four-interlayer sample at the strain rate of ~4.5 × 10^3 s^{-1} (a). Zoomed-in SEM observations (b-d) of positions A, B and C in image (a). Loading direction is shown by arrows in image (a).

One way that could introduce better defined shear bands for further investigations is to load the sample again under same strain rate. The second high strain rate loading was implemented on the same sample after the first loading and the loading conditions were unchanged. However, the new strain rate being less, i.e., ~3.5 × 10^3 s^{-1}, was due to a change of the sample geometry. In other words, the sample expanded under the first compressive load with a Poisson's Ratio of 0.27. The contact area between the deformed sample and the impute bar surface was larger than that before loading, which lead to a lower strain rate. Upon the second high rate loading, the four-interlayer sample was deformed to a total strain of ~0.4.

Figure 4.5 (a) displays the post-loading SEM image of the sample after the second loading at the strain rate of ~3.5×10^3 s^{-1}. From the overview observation in Figure 4.5 (a), the four-interlayer sample loaded to a larger strain has more diffusive shear bands on the cross-sectional surface. The Fe foil is also compressed to a larger extent. The diffusive morphology of the shear bands may be attributed to the non-flat surface introduced by the first loading. Shear bands are observed propagating though the W layers, Fe foils and bonding areas. Even after the second loading, the sample is still intact and no delamination is observed at the interfaces.

A close up image from area A in Figure 4.5 (a) is presented in Figure 4.5 (b) where the typical canonical structure with curved flow lines is clearly revealed. Figure 4.5 (c) and (d) are other two SEM images from the W/Fe interfaces. From those two images, the Fe foils have sheared to a large extent with cracks being observed inside the shear band. Localized delamination between W and Fe has been observed inside the shear band where the shear strain is the largest.

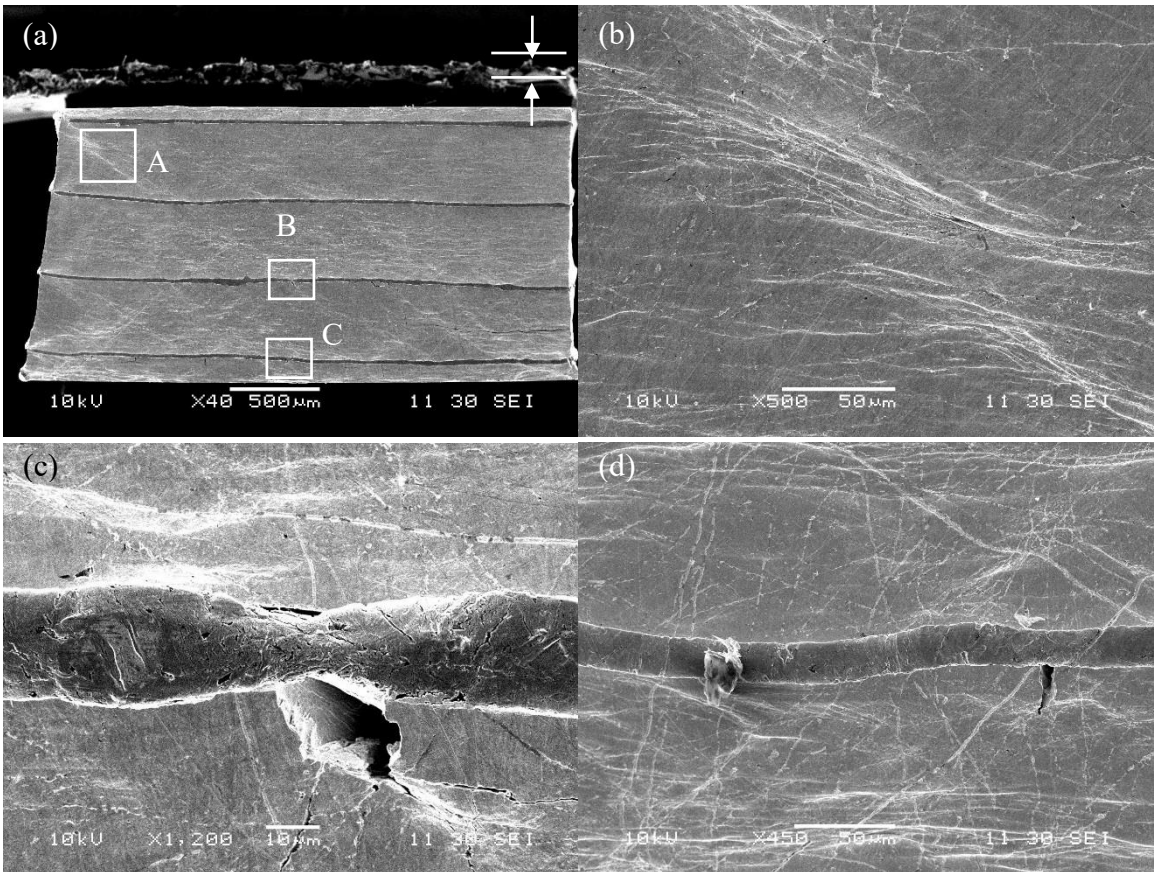

Figure 4.5: Post-loading SEM image of the four-interlayer sample after the second loading at the strain rate of ~3.5×10^3 s^{-1} (a). Zoomed-in images (b-d) of areas A, B and C in image (a). Loading direction is indicated by arrows in image (a).

In general, the four-interlayer sample displays ASL upon high rate loading and only localized delamination was observed at the interfaces which indicates that the bonding strength is strong enough to survive the wave propagation in a multi-interlayer structure. In other words, the occurrence of ASB is universal in heterogeneously stacked structures and the number of interlayer does not have an effect on the wave propagation or the formation of ASB.

4.2 Ballistic performance

4.2.1 Ballistic sample and performance justifications

High strain rate mechanical behavior investigations on the three-layer structure or four-

interlayer structure demonstrated that the heterogeneously layered structure not only has a propensity to adiabatic shear failure, but also could be used to fabricate bulk samples or projectiles to overcome the geometrical limitations of rolled W. The high strain rate mechanical tests in the previous context were conducted on SHPB system at strain rates from 10^3 s^{-1} to 10^4 s^{-1} at most. However, the loading rates for a KE penetrator launched from a high velocity tank gun can reach up to ~10^6 s^{-1}. Under these circumstances, bonding strength and the occurrence of ASBs should be investigated at an extremely high strain rate to simulate the real gun lunching and penetration performance. Therefore, a bulk heterogeneously layered material that has a larger thickness is needed for a ballistic performance study. In this chapter, a bulk material with a total thickness of ~12 mm (25 Fe foils and 26 W layers) was fabricated through diffusion bonding and then EDM cut into cylinders with a diameter of 4 mm for the ballistic tests.

Normally, the observed flow lines and failure behaviors of the penetrator materials can be divided into three general categories: stable plastic flow, plastic flow with “late” plastic localization and rapid localization after small plastic strains, correspond to different levels of penetration performance [3]. Stable plastic flow could indicate no ASB formation during the penetration process which leads to a big mushroom head. This is not favorable at all for the penetration process. Plastic flow with a “late” plastic localization means that adiabatic shear happens at a late stage and the shear bands are usually found at the rear of the projectile, instead at the head of the projectile. The most favorable situation is a rapid localization after small plastic strains. ASB could be identified at the head of the projectile residual or at the edge of the projectile-target interface which shows an earlier shear localization event demonstrating the desired behavior.

4.2.2 Projectile-target interface observations

Figures 4.6 (a) and (b) are the top and cross-sectional views of the bulk heterogeneously layered sample after bonding. 26 W layers and 25 Fe foils were bonded together under applied pressure and temperature. This cuboid was then EDM cut into two cylinders with a diameter of 4 and length of 12 for ballistic testing. Figure 4.6 (c) is one of the steel targets after ballistic test with the penetration direction into the paper. The steel target was then sectioned into halves, as displayed in Figure 4.6 (d) for microstructural investigations of the projectile residual. The material inside the penetration tunnel is the Bi-Sn filler which was used as a fill-in material to secure the loose projectile residuals inside the cavity for metallographic examination.

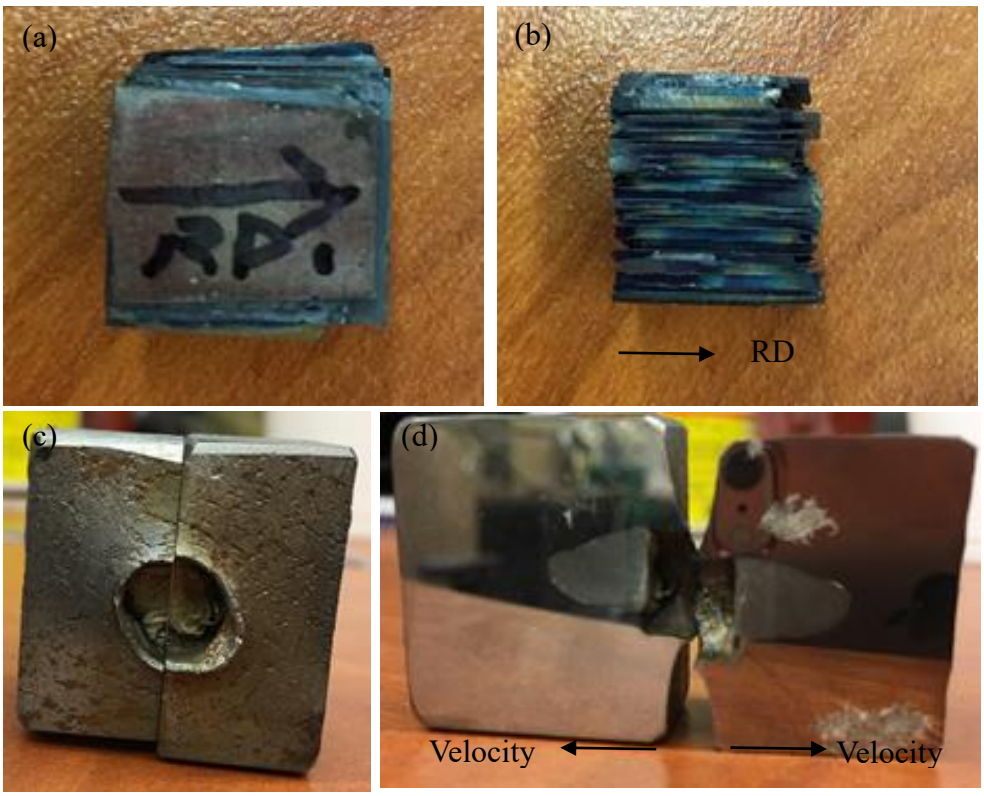

Figure 4.6: Top view (a) and cross-sectional view (b) of a bulk heterogeneously layered sample after bonding with RD being shown in each image. The steel target (shot 1 in Table 2.3) after ballistic test (c). The steel target was sectioned into halves with projectile shooting velocity being shown (d).

In Figures 4.7 (a) and (b), matching halves of the projectile near the projectile-target interface are recognized and highlighted with the red box after mechanical polishing. The center of the tunnel cavity was not included in the image mosaic because it is the place where the Bi-Sn filler is located, and no residual is expected to be observed in that area. SEM observations and EDX analysis will be discussed during the microstructural examination and elemental identification.

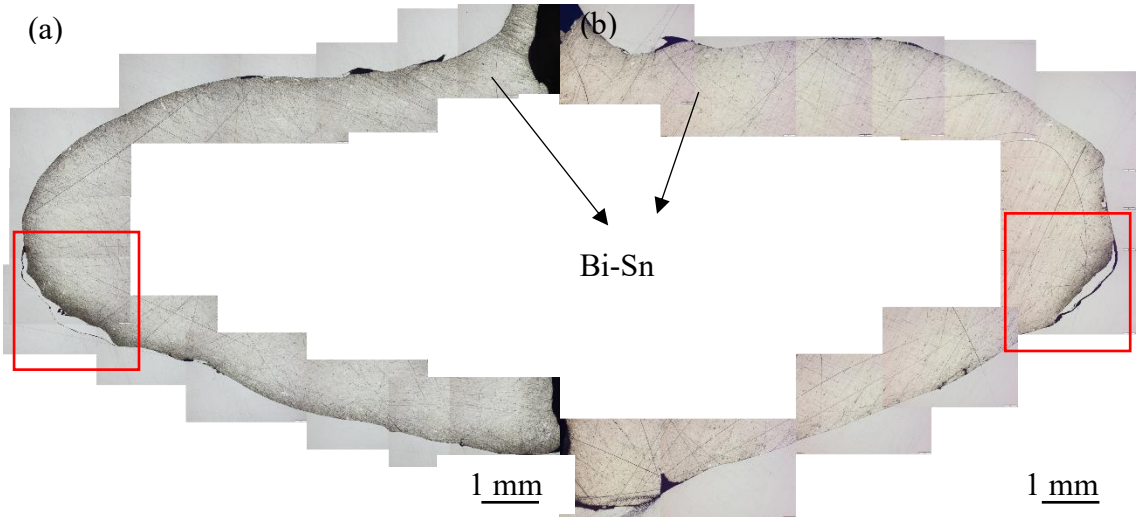

Figure 4.7: Montage of optical images of two halves of the mild steel target (a, b) which was shot at the velocity of ~1 × 10^3 m·s^{-1}. The fill-in material in the cavities is the Bi–Sn filler that was used to seal the projectile residuals. The areas highlighted with red boxes are where the projectile residuals are located, which was confirmed by EDX.

A close-up montage of SEM images of the projectile residal in Figure 4.7 is revealed in Figure 4.8. Two continuous dark thin strips in the SEM image are the Fe foils that functioned as the interlayers in between the W layers. Upon the ballistic test, the thickness of the Fe foil is ~2-5 µm compared to the 25 µm original thickness. The thickness of the W layer in the residual is ~100-150 µm in average while the original thickness was ~465 µm. In other words, the thickness reduction of Fe foil is ~80 % and ~ 60 % for W at least in terms of their original thicknesses. Another observation from Figure 4.8 is that Fe foils

are sheared heavily at some regions and possible shear bands are existing at which the Fe foils have sheared.

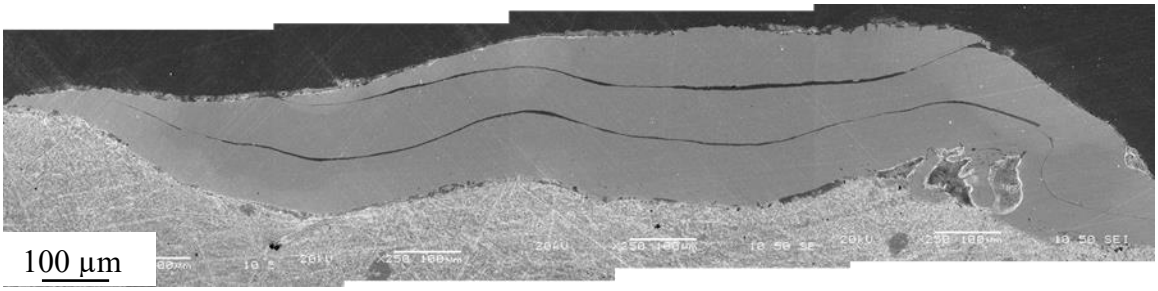

Figure 4.8: Montage of SEM images of the projectile residual in Figure 4.7 (a). The dark thin strips indicate the Fe foils in between W layers.

Figure 4.9 (a) is a montage of optical micrographs of the projectile residual that was shown in Figure 4.7 (a) after etching with Murakami solution. From the overview image in Figure 4.9 (a), the Fe interlayers are visible in some areas but not as clearly as in the SEM images. However, flow lines and shear bands are evidently observed from the optical micrographs. Close ups of areas A-D in Figure 4.9 (a) are shown in Figure 4.8 (b-e), respectively. Figures 4.9 (b), (c) and (e) are the close-up views of areas A, B and D where the edges of the projectile residual are revealed with shear localization, demonstrating the adiabatic shear failure mechanism of the stacked multi-layered material during penetration process. The flow lines bend down through the boundary into the band and yet stop on the other side of the band because of fracture. From Figure 4.9 (d), a complete canonical structure is shown in the image with an Fe foil sheared together with W layers. Moreover, the W/Fe bonding faces are intact in the projectile residual.

The other side of the projectile residual in Figure 4.7 (b) was investigated under SEM and OM for the purpose of revealing and understanding the existence and morphology of ASB on the other half of target. Figure 4.10 (a-c) are the SEM images of the residual after mechanical polishing. Figure 4.10 (a) is the montage of SEM images where W layers and

Fe foils are clearly discerned and distinguished from the target and the Bi-Sn filler. Two Fe interlayers and three W layers are visible in the residual with an Fe foil thickness of ~2-5 μm and W layer thickness of ~100-150 μm. In other words, the thickness reduction of the Fe foil and W layer embedded in the other half of the target are ~80 % and 60 %, respectively. Figure 4.10 (b) and (c) are the close-up images of areas A and B in Figure 4.10 (a). In each image, the Fe foil thickness in some areas is thinner than in other places and this could be caused by severe shear or the existing of ASB in some regions. Besides, the bonding faces in the projectile residual also stay intact in most of the region with only localized delamination being observed.

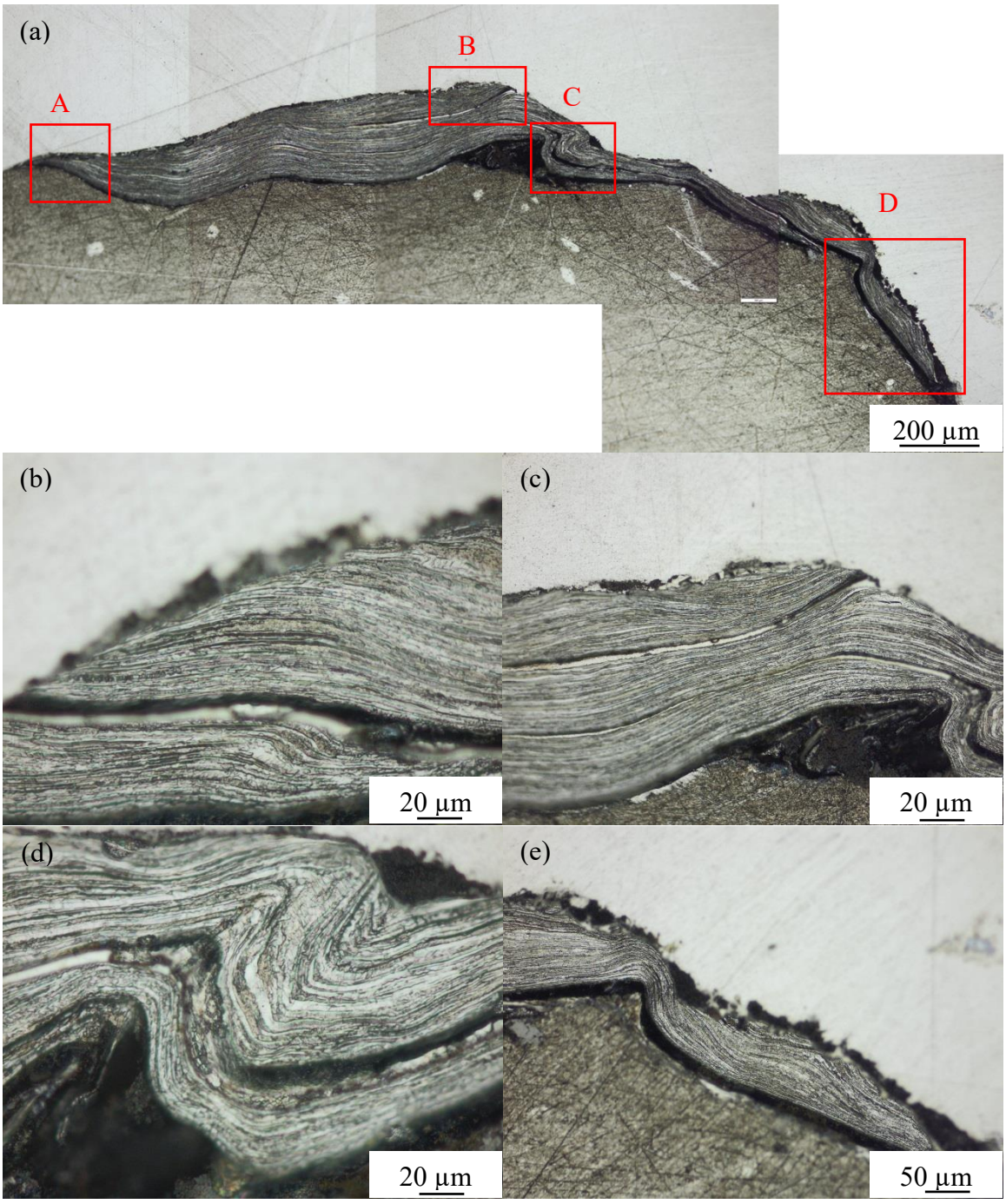

Figure 4.9: Montage of the optical micrographs of projectile residuals in Figure 4.7 (a) after etching with Murakami solution (a). Zoomed-in images (b-e) of areas A-D in (a).

Optical observations after etching were performed on the same projectile residual which is described in Figure 4.7 (b) for flow lines and shear band investigations. Figure 4.11 (a) is a montage of optical images of the projectile residual after etching. From this optical

image, flow lines that are introduced by the ballistic performance are clearly shown inside and at the edge of the residual. Areas A-D in Figure 4.11 (a) are enlarged at high magnifications and displayed in Figures 4.11 (b-e), respectively. From those images, the elongated W grains are attributed to the low homologous temperature rolling are revealed. In Figures 4.11 (b, c), the edges of the projectile residual display features of shear failure due to the formation of shear bands upon the extremely high rate loading. Additionally, W is observed suffering from severe stretching before failure. Shear bands are also witnessed to exist in W layers in Figures 4.11 (d) and (e). A crack that developed at the W/Fe interface is seen in Figure 4.11 (e) as a consequence of severe adiabatic shear with a shear strain being calculated to be as high as 0.7.

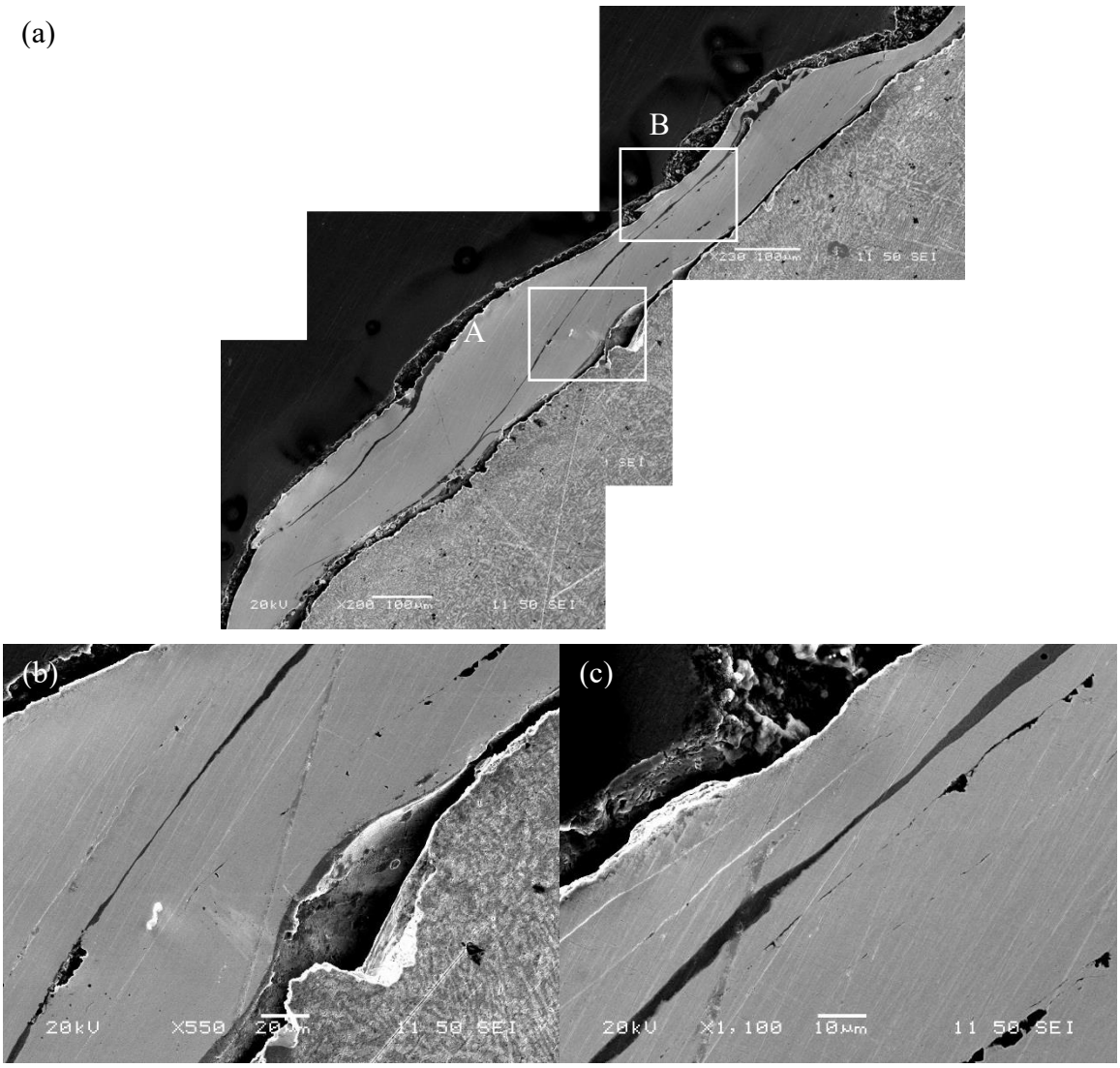

Figure 4.10 Montage SEM images (a) of projectile residual described in Figure 4.7 (b). Close views (b, c) of areas A and B in image (a). The dark lines indicate the Fe foils which are in between W layers.

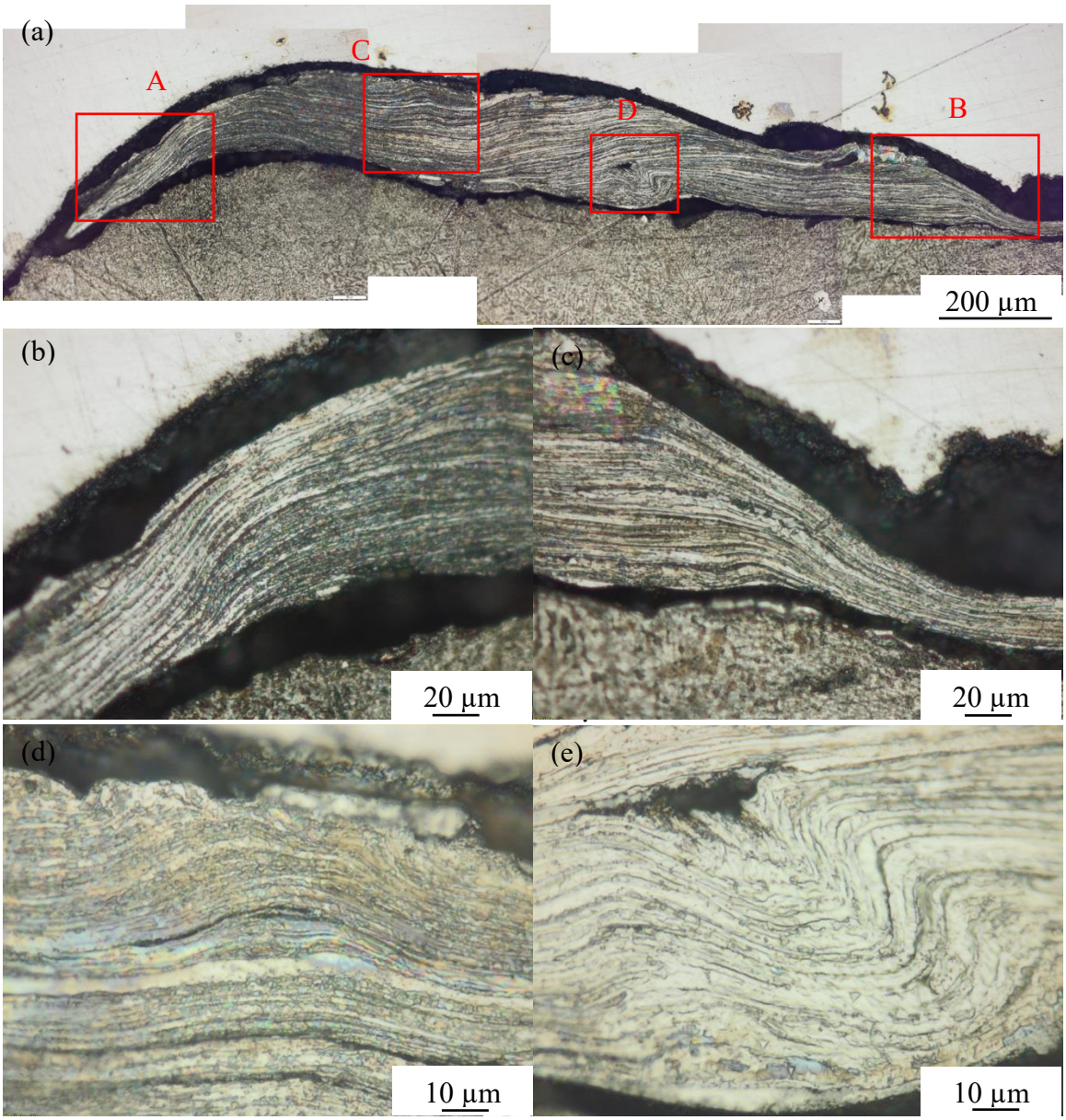

Figure 4.11: Montage the optical micrographs of projectile residual described in Figure 4.7 (b) after etching with Murakami solution. Close-up images (b-e) of areas A-D in (a), respectively.

4.2.3 Observations of the projectile rear

The microstructural analyses using OM and SEM evidently display and reveal the existence of ASB in the projectile residuals at the projectile-target interface. Those observations deliver the information that rapid localizations happened after small plastic strains, and corresponded to an “earlier” shear event during the penetration process. The

target of the ballistic test 2 (Table 2.3) was also sectioned into halves for microstructural investigations. Two pieces of residuals were identified at the rear of the projectile and are shown in Figures 4.12 (a, b). Compared with the shot 2 cavity circumference in Figures 4.12 (a, b), the shot 1 cavity in Figure 4.7 (a, b) is smoother than the one in Figure 4.12 (a, b). The rough tunnel wall in Figures 4.12 (a, b) can be treated as another way to characterize the existing of adiabatic shear failure during penetration.

Close-up views of the residual in Figures 4.12 (a) and (b) are shown in Figures 4.12 (c) and (d), respectively. In Figure 4.12 (c), the residual edge that is embedded in the steel target only displays a massive plastic deformation. However, the residual edge exposed in the air can be identified as the adiabatic shear failure. More adiabatic shear failure evidences are displayed in Figure 4.12 (d). The layered structure is indisputably revealed after polishing and etching with Fe foils and W layers being able to be distinguished. One can say that it is the ASB that shears the projectile when penetrating through the steel target. From the residuals, most of the W/Fe bonding faces remained intact with only localized delamination being observed. In general, the strength of bonding faces survived the extremely high rate loading during ballistic test and the bulk heterogeneously stacked structure delivered the adiabatic shear failure as expected.

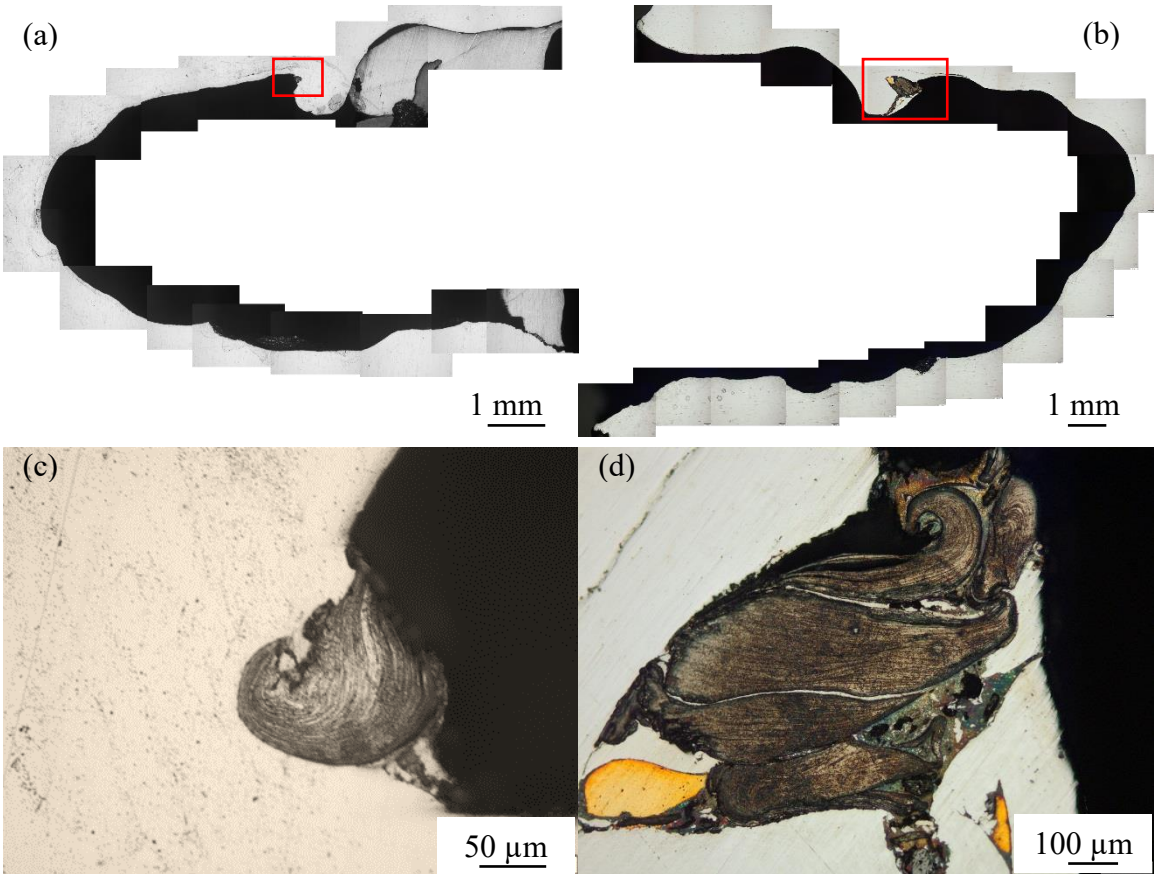

Figure 4.12: Montage of optical images of two halves of the mild steel target (a, b) described as shot 2 in Table 2.3. The fill in material in the cavities is the Bi-Sn filler material that was used to seal projectile residuals in small scale projectiles. The areas highlighted in red boxes are the projectile residuals confirmed by EDX. Optical images (c, d) of the highlighted projectile residuals in image (a) and (b). Two areas in image (d) with a yellow tone are identified as contaminations.

4.3 Conclusions

The geometry of the heterogeneously layered structure was successfully extended to the multi-interlayer structure using diffusion bonding. A high strain rate test was conducted on a multi-interlayer sample with four Fe interlayers from a strain rate of ~3×10^3 s^{-1} to ~4.5×10^3 s^{-1}. The subscale ballistic test was performed on the bulk heterogeneously stacked sample to investigate and more realistically simulate a projectile firing event and thus study and understand the penetration process.

Under OM and SEM observations, the bonding interfaces of the four-interlayer samples

were found to be intact upon high rate loading with no large voids or delaminations being observed. Inter-diffusion between W and Fe atoms was studied by EDX at the interface, which facilitates the formation of the atomic bonding and the strength of the bonding faces.

Upon high rate loading at 4.5×10^3 s^{-1}, four-interlayer sample developed light shear bands and the shear bands propagated through the inhomogeneous layers without impedance. Fe foils were sheared to a little extent due to the lower loading rate and deformation strain.

Projectile residuals at the projectile-target interface and the rear of the projectile were revealed and examined under OM and SEM. Massive ASB and significant shear failure features were discovered under microscopic studies, demonstrating the dominant role of adiabatic shear failure in the heterogeneously stacked structure. The W/Fe interfaces inside the projectile residuals were intact upon the ballistic loading at the velocity of $\sim 1 \times 10^3$ $m \cdot s^{-1}$.

The residuals found at the project-target interface exhibited an “early” plastic localization which is the desired outcome during the ballistic test. This discovery demonstrates that the heterogeneously stacked structure developed a rapid localization after small plastic strains and, as it emulates self-sharpening behavior, it helps to create a smaller ballistic cavity and deliver a superior ballistic preformation.

CHAPTER 5: TWIP STEEL (FCC)-MECHANICAL PROPERTIES UNDER STATIC AND DYNAMIC LOADS

5.1 Microstructural characterization

The optical images of the as-received TWIP steel which has not undergone plastic deformation are shown in Figures 5.1 (a) and (b) at different magnifications. From the images, the grain and grain boundaries are not clearly revealed by etching under the optical microscope. The probable reason could be that the as-received steel has experienced heavy plastic deformation during the belt-casting manufacturing process. As is seen in the images, a quite uniform microstructure can be observed and the grain size is roughly ~5-10 μm.

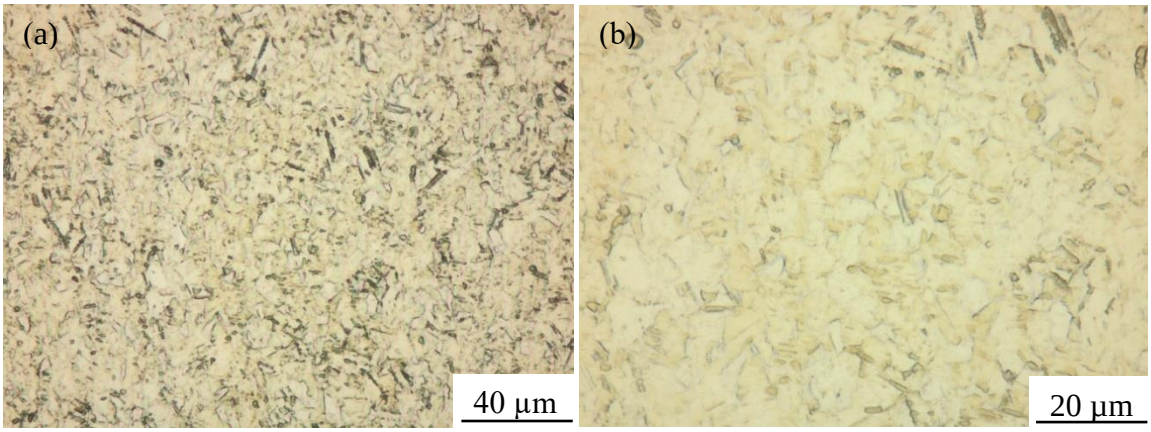

Figure 5.1: Optical micrographs of the as-received TWIP steel under a lower (a) and higher (b) magnifications. The images were revealed by etching with 3 % Nital solution.

Since the microstructure was not well disclosed under OM, TEM was used to reveal the microstructure from dislocation and SF aspects. Figure 5.2 (a) is a BF TEM image of the as-received steel and the corresponding DP is shown in Figure 5.2 (b). The identified diffraction spots show an FCC structure which confirms the lattice structure of the austenitic phase. Dislocations usually emit from the edge of the defects [154, 155], such as grain boundary, twin boundary or stacking faults which is consistent to the observations in Figure 5.2 (c), where dislocations emit from the grain boundaries and possible twin

boundaries. SFs are also observed from the as-received TWIP steel, which are possibly introduced during the manufacturing process. In general, the as-received TWIP steel grains are in the magnitude of several micrometers with a number of twins or stacking faults being observed.

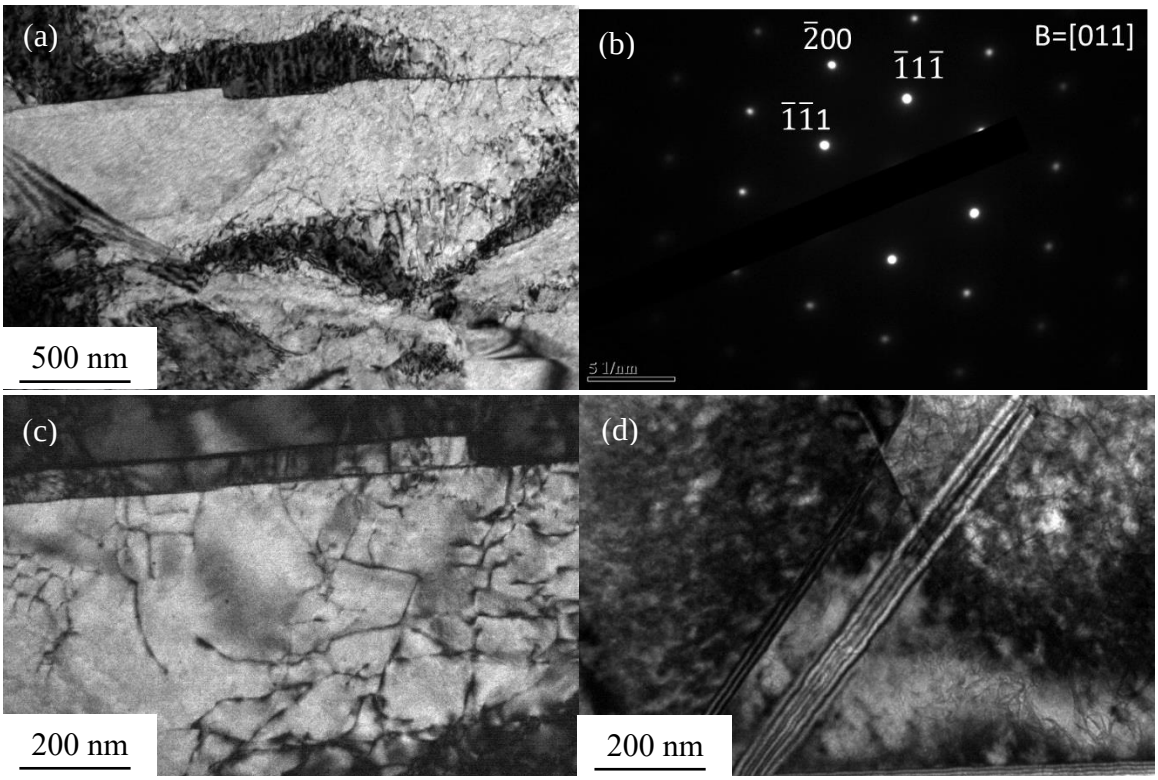

Figure 5.2: TEM image of the as-received TWIP steel (a) and its diffraction pattern (b). TEM image of the as-received TWIP steel showing dislocations (c) and stacking faults (d).

5.2 X-ray diffraction and texture analysis

TWIP steel as studied in the literature and introduced in chapter 1 is a type of steel that has no phase transformation during plastic deformation. XRD is an accurate and widely used characterization method to confirm if any new phase is introduced during straining. Figure 5.3 provides the XRD profiles of the steel before and after tension and high strain rate compression. It is evident that only austenitic phase (γ, FCC structure) peaks were detected in the XRD profiles of the invested steel before and after deformation, i.e. no

phase transformation occurred during deformation. Compared with non-deformed sample, (220) peak and (200) peak under tensile and compression are suppressed, respectively. The reason may be attributed to that the orientations of the grains turn to the directions which favor the formation of deformation twins. Due to the small dimensions of the high strain rate sample, the X-ray signal is significantly lower than that of the other samples.

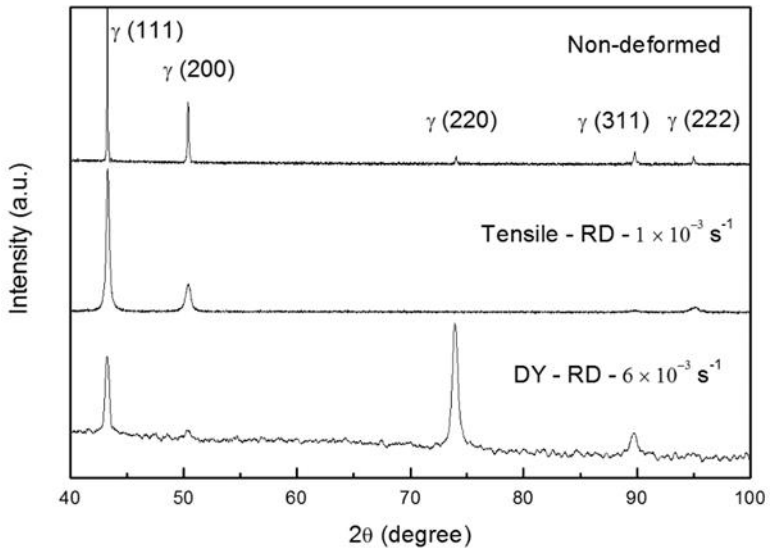

Figure 5.3: XRD (a) of the TWIP steel before (as-received) and after tension and high strain rate compression.

Texture analysis is conducted on the as-received TWIP steel to investigate and predict the mechanical properties under tension, QS and high strain rate compressions. As is seen in Figure 5.4, the pole figures of the as-received TWIP steel shows that the investigated steel is isotropic with only mild {100}<001> and {001}<211> textures which are consistent with other literature studies [105].

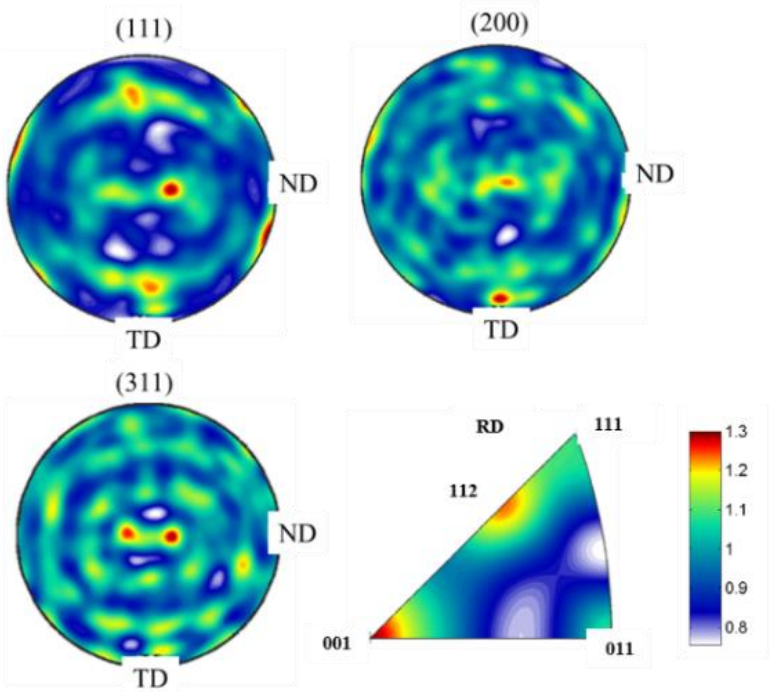

Figure 5.4: {111}, {200} and {311} pole figures of the as-received TWIP steel on the face perpendicular to the rolling direction.

5.2 Tensile properties

As already known, TWIP steels are fully austenitic steels with an enhanced strain hardening rate as well as high strength and good formability. The investigated steel was EDM cut into tensile samples along RD and TD for the following tensile test, as is shown in Figure 5.5. Due to the limitation of the original thickness of the as-received TWIP steel, tensile test along the ND was not able to be performed. Three tests were conducted along each direction for data consistence check.

Figures 5.5 (a) and (b) display the uniaxial engineering and true stress-strain curves under tension along RD and TD with a strain rate of ~1×10^{-3} s^{-1}. The investigated steel is isotropic and exhibits bilinear true stress-strain curves as well as extraordinary strong strain hardening with a yield strength of ~600 MPa and high ultimate tensile strength of ~1000 MPa. A uniform elongation of 0.5 (50%) can be observed from the stress-strain curves and

the strain hardening exponent was determined to be ~0.33 along the RD and TD in Figure 5.5 (c). Another observation from Figure 5.5 (d) is that the investigated steel has a negligible necking or plastic instability under tensile loading no matter the loading direction and this stability should be attributed partly to its strong strain hardening. In general, the investigated TWIP steel shows a great balance between tensile strength and ductility with the partial help of the strong strain hardening.

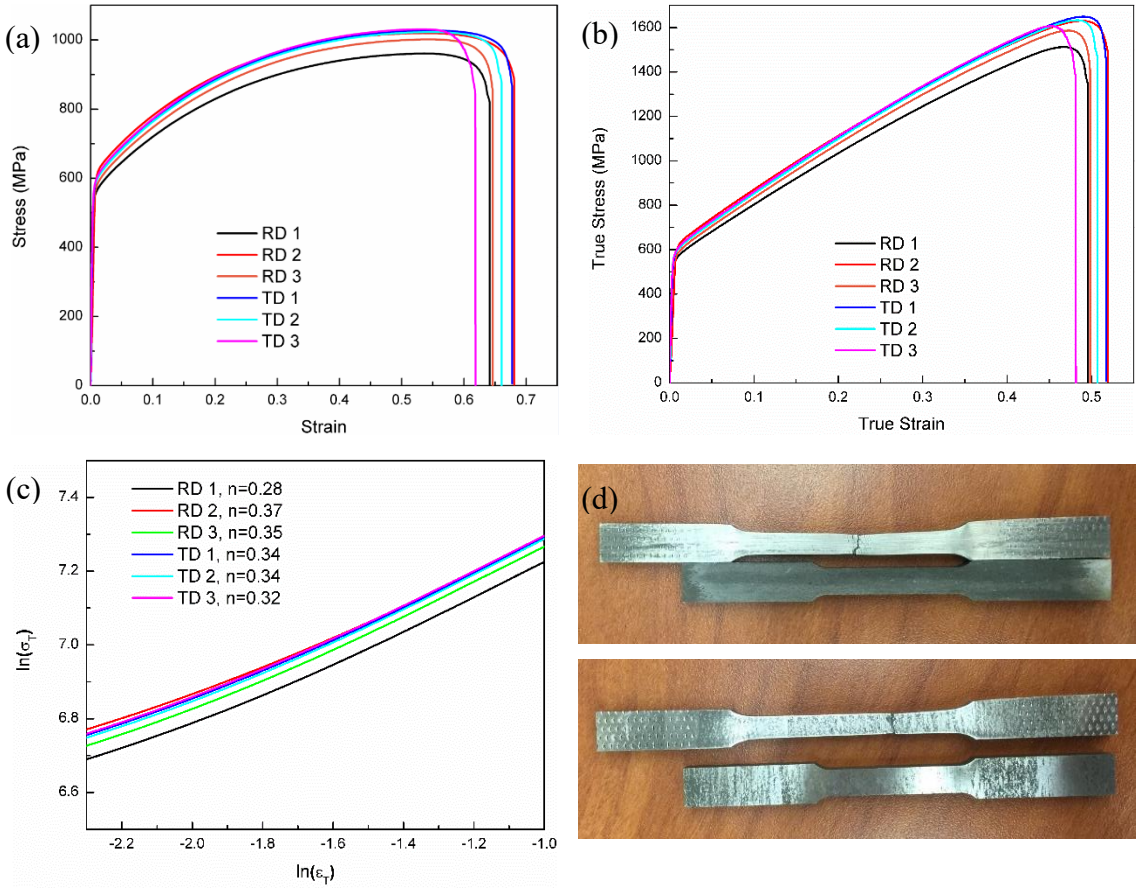

Figure 5.5: Engineering (a), true (b) stress strain curves and strain hardening exponent (c) of the TWIP steel under QS tensile loading. Strain was measured by video extensometer at a strain rate of ~1 × 10^{-3} s^{-1}. Image (d) of a comparison between the samples before and after tension along RD (top) and TD (bottom).

5.3 Quasi-static and dynamic compressive properties

Besides tensile properties, the mechanical performance under compression, such as

under QS and high strain rate compressive loads, also draws a great attention. The compressive mechanical property under both of the uniaxial QS and high strain rate loading were summarized in Figure 5.6. The strain rate of QS compression was ~1×10^{-3} s^{-1} while high strain rates were from ~3.5×10^{3} s^{-1} to 6×10^{3} s^{-1} upon loading. The TWIP steel was tested along RD, TD and ND for isotropic verification. QS compression test was stopped manually at the strain of 0.2 because the sample would buckle or have barreling at a larger strain.

Overall, the TWIP steel is highly isotropic and displays a strong strain hardening under QS and high strain rate compressive loads. The strain hardening rate is high and constant under QS load and yet continuously decreased to a small extent with increased strain at strain rates of ~3.5×10^{-3} s^{-1} and 6×10^{-3} s^{-1}, which should be attributed to the thermal softening at high strain rate. The adiabatic temperature rise describing the global temperature change of the specimen at a strain of 0.1 and 0.4 was calculated to be ~28 K and 160 K, respectively.

The significant strain rate hardening is observed in terms of the yield strength of ~600 MPa and ~900 MPa at the strain rate of ~1×10^{-3} s^{-1} and ~6×10^{3} s^{-1}, respectively. As discussed in previous content, ASB is a phenomenon of materials at high strain rate when thermal softening overcomes the strain hardening and strain rate hardening. Hence, one can draw an assumption that TWIP steel is strongly resistant to ASB at high strain rate because of the outstanding strain hardening and strain rate hardening upon high rate loading, which will be further demonstrated by the microstructural examination.

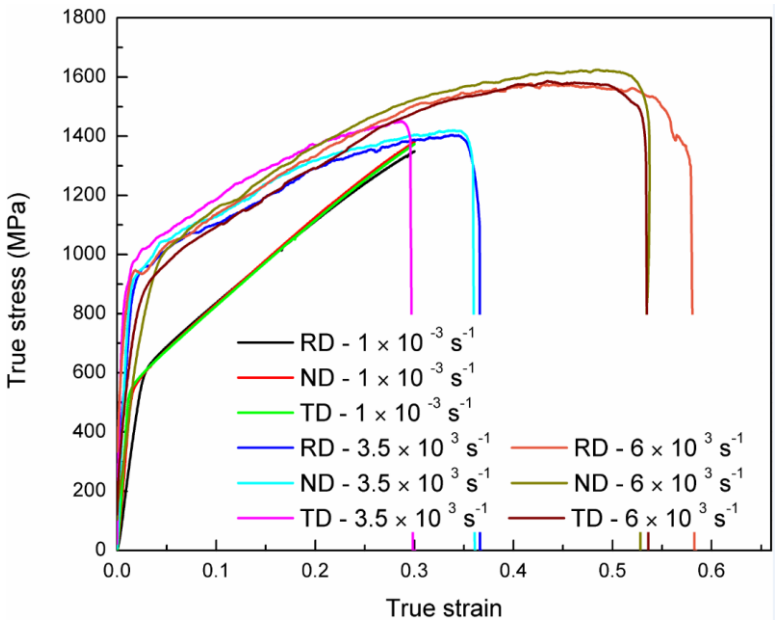

Figure 5.6: QS (strain rate ~1 × 10^{-3} s^{-1}) and high strain rates (strain rate ~3.5 × 10^{3} s^{-1} and ~ 6 × 10^{3} s^{-1}) true stress-strain curves under compression. The sample was loaded to the strain of about 0.2 under QS condition while the stress drop at high strain rate indicates unloading.

In order to reveal the work hardening behavior of the investigated TWIP steel, the work hardening rate versus true strain under QS tension, QS compression and high strain rate compression are shown in Figure 5.7. Strain hardening rates under tension and QS compression are decreased with further strain, followed by a steep decrease in the hardening rate caused by the transition from elastic deformation to plastic deformation. According to Asgari et al. [156], no twinning takes place at this stage, and overlapping of SFs are usually observed which is considered as an incubation stage where dislocation interactions generate twin nuclei. Close inspection of strain hardening rate at high strain rate shows that the initially very high strain hardening rate decreases rapidly after yielding, followed by a steady linear decrease up to a strain of 0.3 and beyond. Under static load, the decreasing of the strain hardening is attributed to a reduction in the rate of primary twin formation while under high strain rate loading, the adiabatic heating also contributes to the

decreasing of the strain hardening rate.

The strain hardening rates of the TWIP steel under QS tension and QS compression at low strain rate show a wider serrated flow, compared to the one under high strain rate loading. This phenomenon could be explained as that high strain rate suppresses the dynamic strain aging [105] which usually displays in a way of serration in the stress-strain curve. On the one hand, the strain hardening rate of the dynamically tested sample is ~1000 MPa lower than that of the samples tested at QS status. On the other hand, the strain hardening rate under dynamic load reaches zero at the strain of ~0.4 which indicates that the thermal softening caused by the adiabatic heating overcomes the strain hardening, displaying as a portion of close flat flow stress in Figure 5.8.

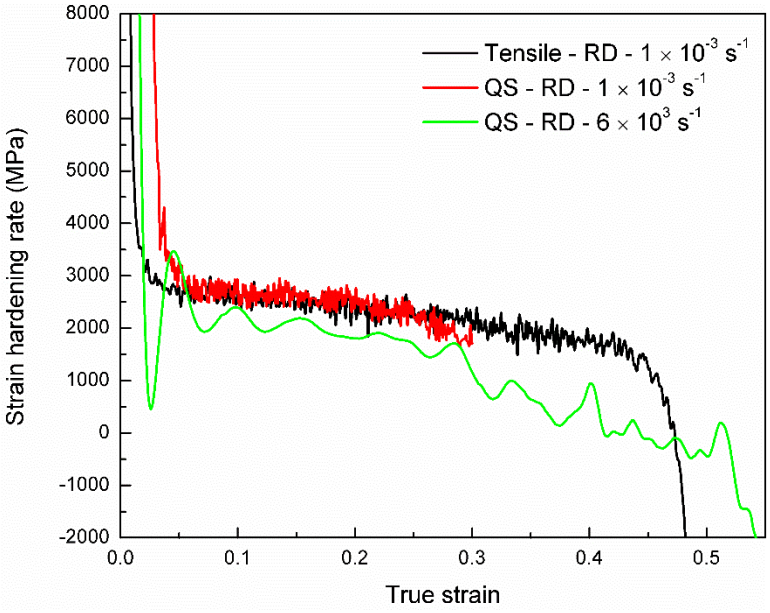

Figure 5.7: Strain hardening rates of the investigated TWIP steel under QS tension, QS compression and high strain rate compression. Loading directions are parallel to RD.

5.4 Post-loading observations

5.4.1 Postmortem observations

Based on the experimental results in previous context, this TWIP steel has a strong strain

hardening and strain rate hardening which suppresses the occurrence of instability, such as necking and ASB at QS and high strain rates. From the tensile post-loading images in Figure 5.5 (d), the loaded sample shows a uniformed elongation and negligible necking near the fracture surfaces is observed, which is consistent to the tensile stress-strain curve with strong strain hardening feature. As for the dynamically tested sample, no stress collapse or flow softening has been observed from the stress-strain curve, which could be used to rationalize the absence of the ASB. The strong strain hardening, strain rate hardening as well as high strength and high ductility facilitate this TWIP steel to be a good armor material. Hence, post-loading observation at high strain rate is indispensable in the future analysis.

Figure 5. 8 (a) is an overview of the TWIP steel fracture surface upon tensile loading. Nearly flat fracture surface with little localized plastic deformation is observed which further demonstrates the strong stability during the plastic elongation. The area highlighted by the white square is closely investigated in Figure 5.8 (b) where a lot of dimples with different sizes are shown in the image. The diameter of the coarse dimples falls in the range of 10 to 20 μm while fine dimples have a diameter less than 5 μm, which can be seen in Figure 5.8 (c). Additionally, coarse dimples are usually deeper than small dimples. Dimples in Figure 5.8 (c) have a circular shape demonstrating a uniaxial tensile load was applied on that area while elliptical dimples indicate the shear failure. Xiong et al. [157] pointed out that course dimples have only been identified in the heterogeneous structure with embedded nanotwin bundles and equiaxed and fine dimples were prominently observed on the fracture surfaces of homogeneous nanocrystalline and UFG materials. Therefore, the coarse dimples could be the place where deformation twin bundles in micrometer or

nanometer size were developed during tension.

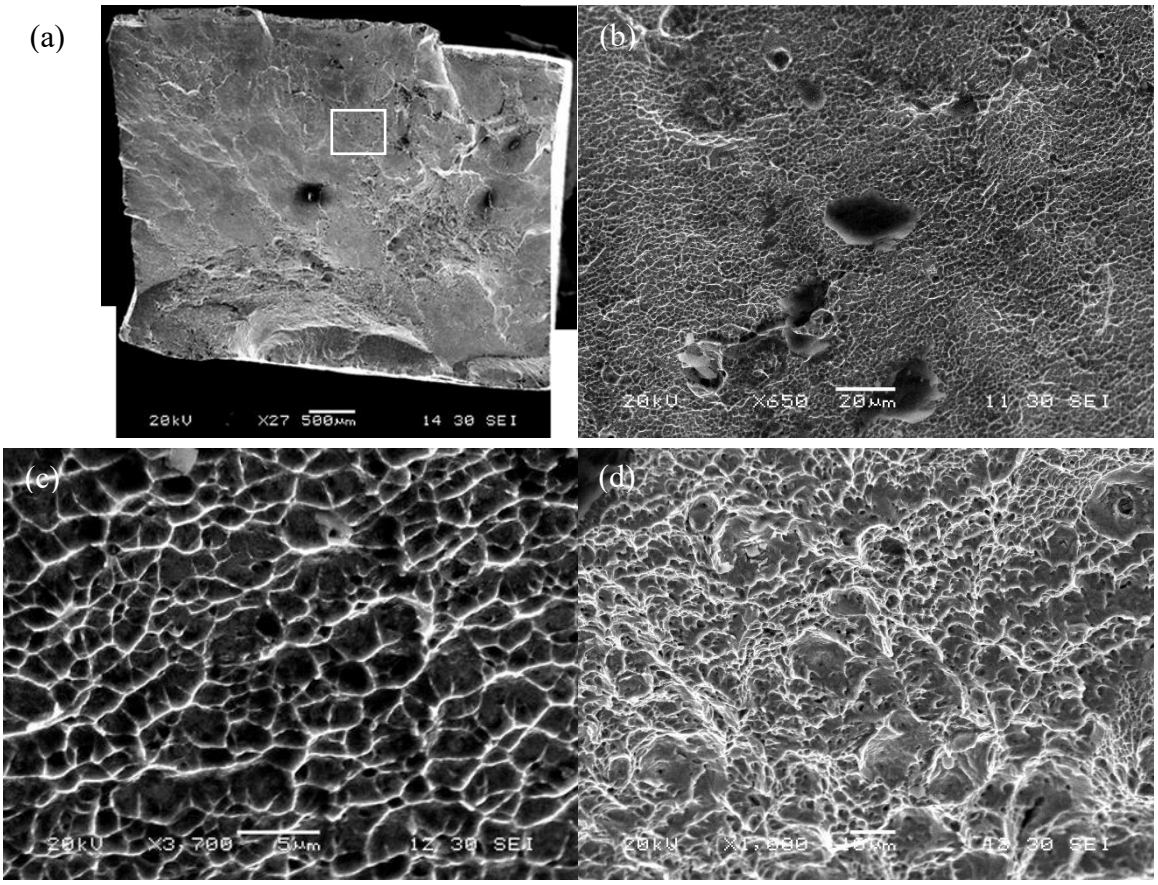

Figure 5.8: SEM fractographic observations of the TWIP steel upon tensile loading (a-d). Zoomed-in image (b) of the highlighted area in (a).

Per discussed in the dynamic mechanical behavior in this chapter, adiabatic shear failure or ASB was not expected to be seen according to the dynamic stress-strain curves with strong strain hardening and strain rate hardening. This assumption will be confirmed by the post-loading SEM observations on the cross-sectional surface of the dynamically tested sample. Figure 5.9 (a, b) and (c, d) are postmortem SEM images of the specimen loaded at the strain rate of ~6×10^3 s^{-1} along RD and TD, respectively. The samples after dynamic loading along RD and TD show the uniform and bulk deformation without any type of shear localization on the side surface even though the strain was reached as high as 0.5.

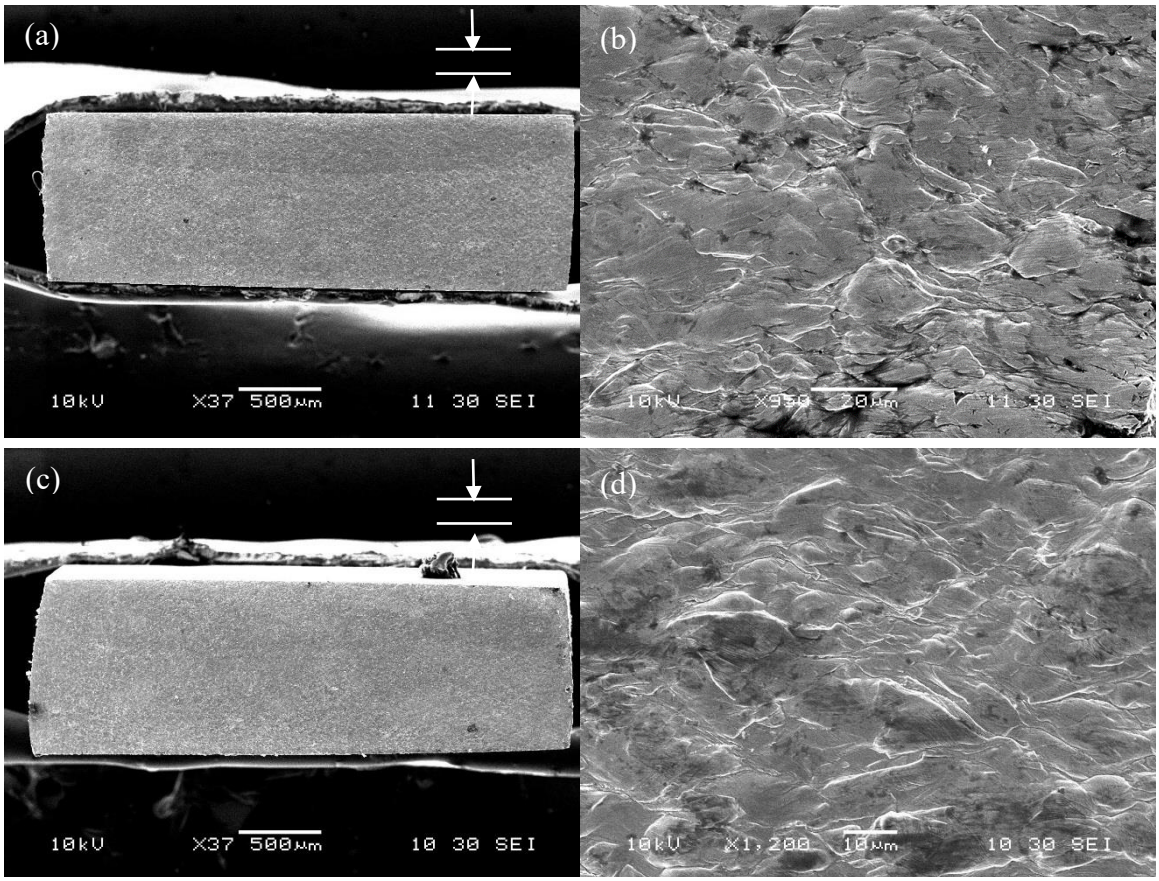

Figure 5.9: Postmortem SEM images of the samples at strain rate of 6×10^3 s^{-1} (a-d). Images show macro (a) and microscale (b) observations of the specimen loaded along RD; micro (c) and microscale (d) views of the specimen loaded along TD. Loading direction is indicated in the images.

5.4.2 Transmission electron microscopy examinations

TEM images of the investigated steel after tension are displayed in Figure 5.10 (a, c) with the SADP being shown in Figure 5.10 (b, d), respectively. Figure 5.10 (a) is a BF TEM image of the TWIP steel after tension and a lot of defamation bands are observed within the individual grains. The elongated diffraction spot in Figure 5.10 (b) demonstrates the strip morphology in Figure5.10 (a). From another spot of the tensile tested sample as shown in Figure 5.10 (c), deformation twins were identified from both the image and SADP in Figure 5.10 (d).

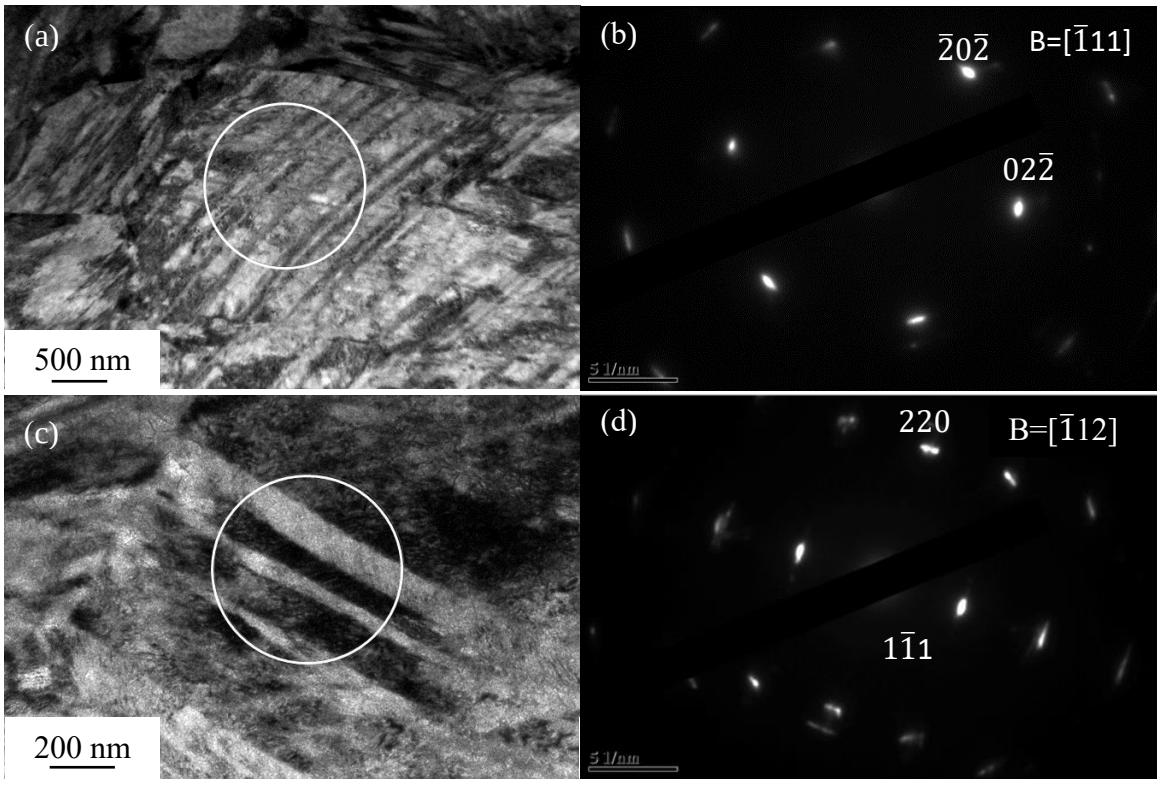

Figure 5.10: TEM image of investigated TWIP steel after tension test (a, b) and its SADP (b, d), respectively.

The TWIP steel specimen loaded at the strain rate of ~6×10^3 s^{-1} was examined under TEM and the results are shown in Figures 5.11 and 5.12. A great density of SFs have been observed upon high strain rate loading, as shown in Figure 5.11 (a) and (c). The corresponding SADP in Figures 5.11 (b) and (d) from the circular area displays a feature of streaking, which further demonstrates the existence of SFs. Compared with the twin morphology under tesnion in Figure 5.10 (c), high rate loading refines the deforamtion twins in Figure 5.11 (a). This large amount of SFs could be the source of twinning embyro.

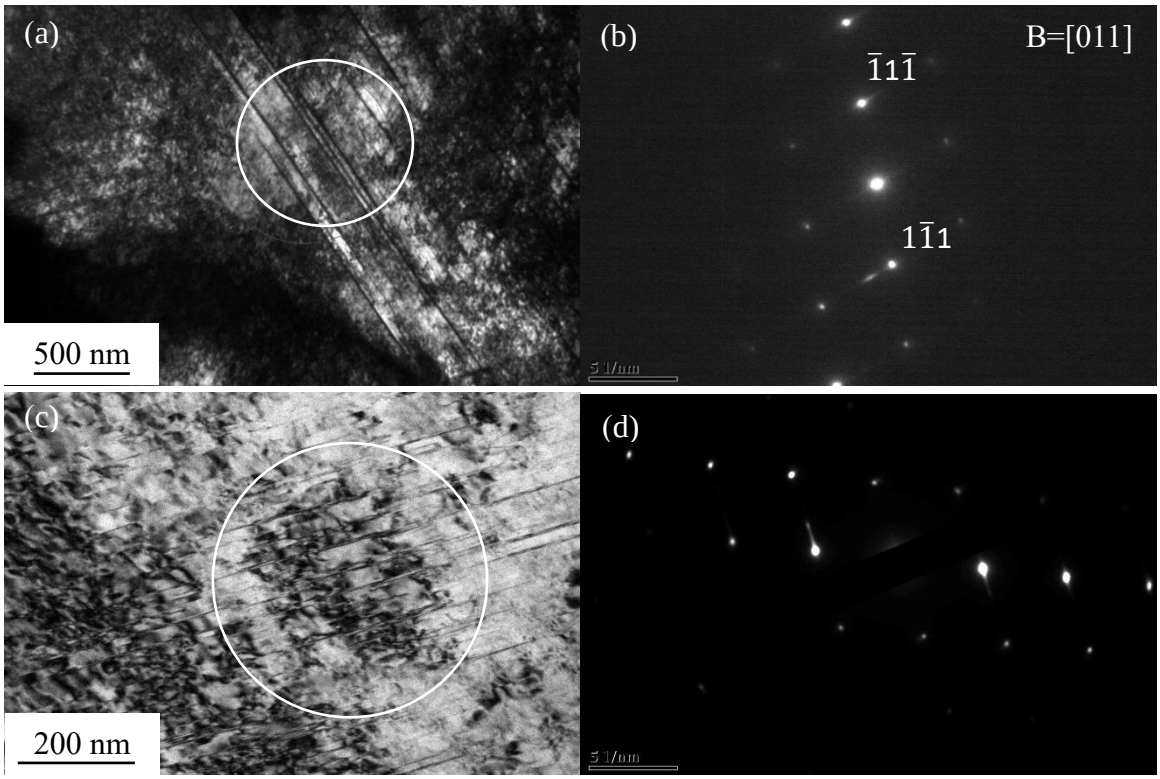

Figure 5.11: TEM images of stacking faults (a, c) and SADP (b, d), respectively, of the dynamic tested sample at strain rate of about 6×10^3 s^{-1}.

Figures 5.12 (a, c) are the TEM BF and DF images of the deformation twins developed at the strain rate of ~6×10^3 s^{-1}. The twin thickness is ~100 nm in Figure 5.12 (a) and is much thinner compared with the ones progressed during tension. This phenomenon is known that less time was given for twin embyro and twin growth under high strain rate compressive load. Figure 5.12 (c) is the DF image of deformation twins and they were identified at the grain boundaries as pointed out by the arrows.

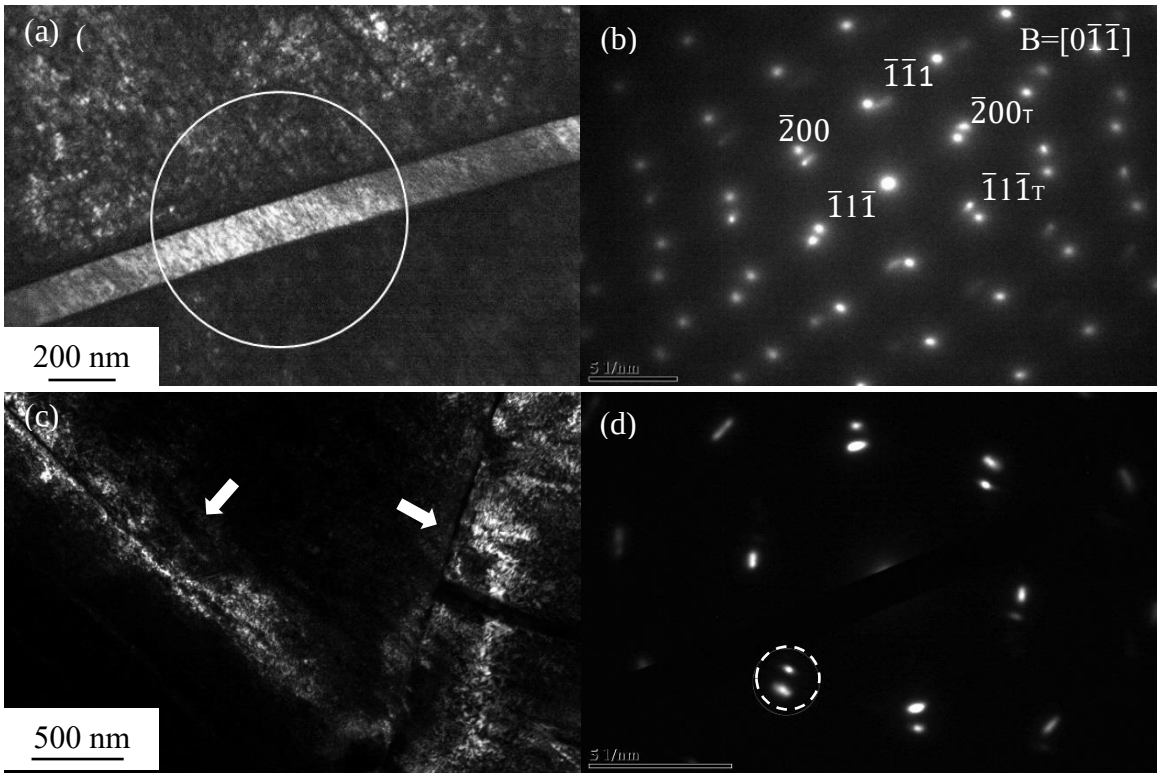

Figure 5.12: TEM images of deformation twining (a) and SADP (b) of the dynamic tested sample at strain rate of about 6×10^3 s^{-1}. TEM dark field image of the deformation twinning and its DP (d)

5.6 Conclusions

TWIP steel with a chemical composition of Fe-15Mn-2.5Si-2Si-0.6C has been comprehensively studied in the aspects of metallography and mechanical properties under tension, QS and high strain rate compression.

The as-received TWIP steel has a uniform and unidentified microstructure after manufacturing and the grain size is roughly ~5 µm to 10 µm. Only austenitic phase was observed before and after mechanical deformation. Mild {100}<001> and {001}<211> textures existed in the as-received steel.

The investigated steel is isotropic and exhibits bilinear true stress-strain curves as well as an extraordinary strong strain hardening behavior with a yield strength of ~600 MPa and high ultimate tensile strength of ~1000 MPa. The strain hardening exponent was

determined to be ~0.33 along the RD and TD under tension. Ductile feature evidenced by the presence of dimples is revealed under SEM from the fracture surface. Course dimples are believed to be caused by the heterogeneous structure with embedded nanotwin bundles. Equiaxed and fine dimples are from the fracture surfaces of homogeneous nanocrystalline and UFG materials.

TWIP steel exhibits a strong strain hardening under QS and DY compressive loads. Significant strain rate hardening has been observed in terms of the yield strength of about 600 MPa and 900 MPa at the strain rate of $\sim 1 \times 10^{-3}\ s^{-1}$ and $\sim 6 \times 10^{3}\ s^{-1}$, respectively. Upon dynamic compressive loading, the sample deformed uniformly without any shear localization being observed on the cross-sectional surface. The strain hardening rate at high strain rate is lower than that QS status and has fewer serrations in the stress-strain curves. This could be explained as that high strain rate suppressed the dynamic strain aging.

TEM observations from the samples upon high strain rate loading display an excessive number of thin deformation twins and SFs. During high strain rate loading, less time was given for the twin embyros to grow compared to the QS tension, which leads to the formation of nanotwins.

CHAPTER 6: THE UNDERLYING MECHANISMS FOR THE REMARKABLE RESISTANCE TO ADIABATIC SHEAR BANDING

The investigated TWIP steel (Fe-15Mn-2.5Si-2Al-0.6C) shows an outstanding and impressive strain and strain rate hardening upon high rate loading. However, the extraordinary strain rate hardening has not been explained and understood comprehensively yet. In this chapter, the theory underlying the strong strain rate hardening will be studied in the context of deformation kinetics: high strain rate sensitivity (SRS) and extremely small activation volume. Moreover, the underlying mechanism for the remarkable plastic stability under tension and compression will be evaluated. Nanoindentation tests that were conducted to examine the activation volume and size effect will be also discussed. Lastly, the mechanical properties at elevated temperatures within the context of the Zener-Hollomon parameter will be discussed at the end of this chapter.

6.1 Strain rate sensitivity and activation volume

Strain rate sensitivity and the presence of nanoscale twins have been widely studied to improve the mechanical properties of nanostructured metals [158-160]. As for TWIP steel, the strain rate jump test is one of the more common methods to determine the SRS value. Figures 5.1 (a-c) displays the engineering stress-strain curves of the TWIP steel corresponding to a strain rate jump test along the RD, ND and TD. The imposed jump rates for each sample are indicated in the graphs. The logarithmic flow stress at each strain rate is plotted against the logarithmic strain rate in Figure 5.1 (d). The SRS value, m, is shown in Figure 5.1 (d) along each loading direction.

The SRS of this nearly isotropic TWIP steel along RD, ND and TD are 0.075, 0.076 and 0.076, respectively, which shows quite consistent results. The high SRS value is consistent

with the strong strain rate hardening behavior that has been observed upon the high strain rate compression test. In the literatures, the SRS for CG FCC metals, such as Cu, is found to be ~0.004 while it is 0.015/0.019 for UFG/NC Cu [37]. However, the SRS of the CG TWIP steel is more than an order of magnitude larger that of CG Cu, and even larger than that of the SRS of UFG/NC Cu. In other words, this CG TWIP steel possesses a remarkably high SRS value which is only found in UFG/NC FCC metals with relatively low melting points. This is probably attributed to the excessive amount of twinning and twin boundaries that developed during plastic deformation and, as such, those twin boundaries refine the existing grains via the "dynamic Hall-Patch" effect [52, 115, 130, 159].

In addition to the strain rate sensitivity, the activation volume for thermal activation is another very important parameter that provides a better understanding for the deformation mechanisms of metals [161]. From Eq. (1.8) and (1.9), the activation volume is calculated to be ~$5.2b^3$ with b being the magnitude of the Burgers vector of TWIP steel which is 2.5×10^{-10} m [162]. In contrast, for CG undeformed Cu, the activation volume is ~$1000b^3$ [37]. After SPD, such as ECAP and cold rolling, the activation volume of UFG/NC Cu was significantly reduced to ~$41b^3$ to $48b^3$ [37]. Through the comparison of the activation volumes of CG and UFG/NC Cu with the investigated TWIP steel which is ~$5.2b^3$, one can see that the activation volume of the CG TWIP steel is three orders of magnitude smaller than that of CG Cu and an order of magnitude smaller than that of UFG Cu. Additionally, it is important to recognize that, in the past, such small activation volume was only found in metals with grain size in the NC regime [52].

This type of CG TWIP steel has an unusually high strain rate sensitivity and extremely low activation volume that only some UFG and NC FCC metal would have. This unique

combination of properties could be ascribed to the extremely high density of mechanical twins that are introduced during straining at high strain rates. Twin boundaries could work as grain boundaries to refine the grain size. Meanwhile, the small distance between twins leads to a very short mean free path for the dislocation movement.

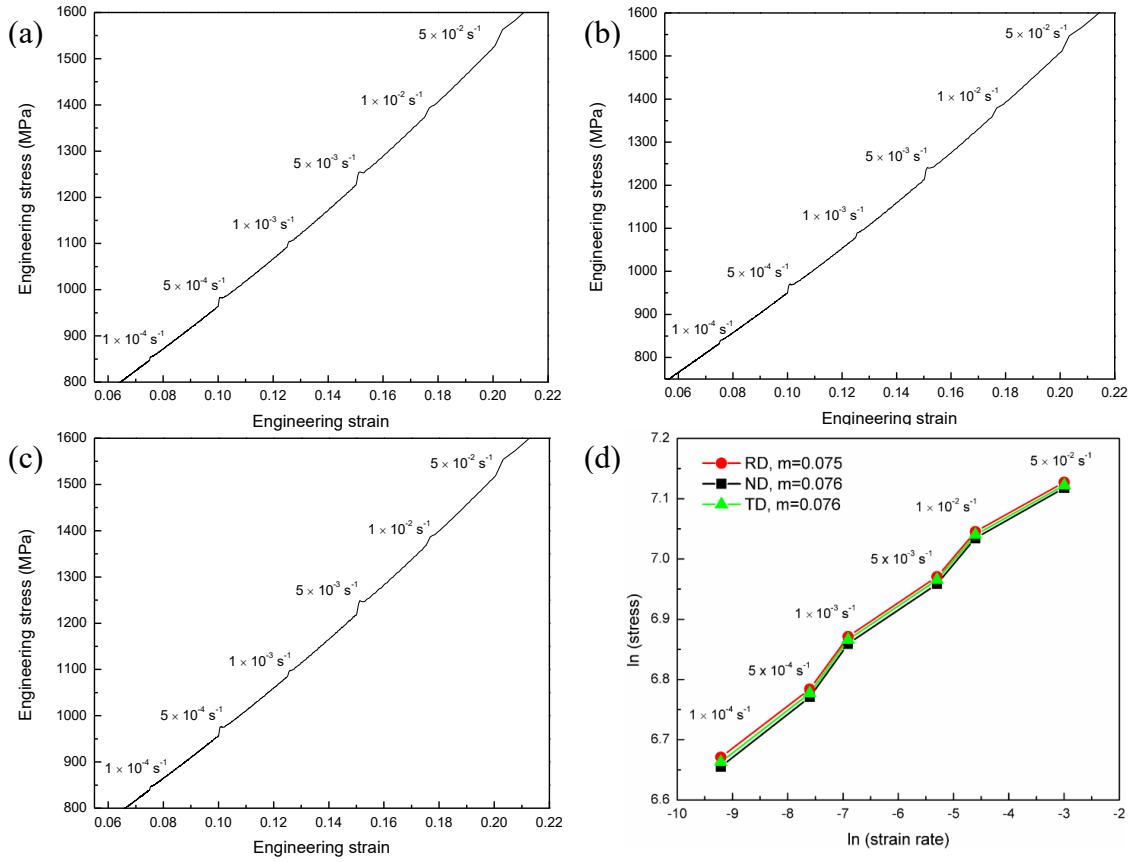

Figure 6.1: Engineering stress-strain curves corresponding to a strain rate jump test of the TWIP steel along RD (a), ND (b) and TD (c). Stress versus strain rate is graphed on a double logarithmic scale (d).

6.2 Size effect

Size effect is defined as changes in material properties such as mechanical, optical or electrical due to changes in the overall physical dimensions or in the internal features of the structure [163-165]. Therefore, a complete understanding of the relationship between the external length scale effect and the internal structure, such dislocation nucleation,

motion and storage and geometrically necessary dislocations (GND) that are required to accommodate plastic strain gradients within the material is essential [164, 166-168]. Systematic investigations of the relationship between the external length scale and the mechanical properties are widely studied because of the greater accessibility to laboratory equipment, such as nanoindentation instruments and micro-compression apparatus.

Many observations of microscale plasticity phenomena display a size effect wherein the smaller the size of the specimen the stronger the response. If explained in terms of using indentation hardness testing in metals, the result is that the hardness value increases as the size of the indenter decreases [169, 170]. For example, a single crystal silver (Ag)'s hardness was found to be dependent on the size of the indentation for the sizes below ~10 μm which is displayed in Figure 6.2. As seen in the figure, the hardness value increases as the size of the indenter or the indent displacement decreases which delivers a strong size effect.

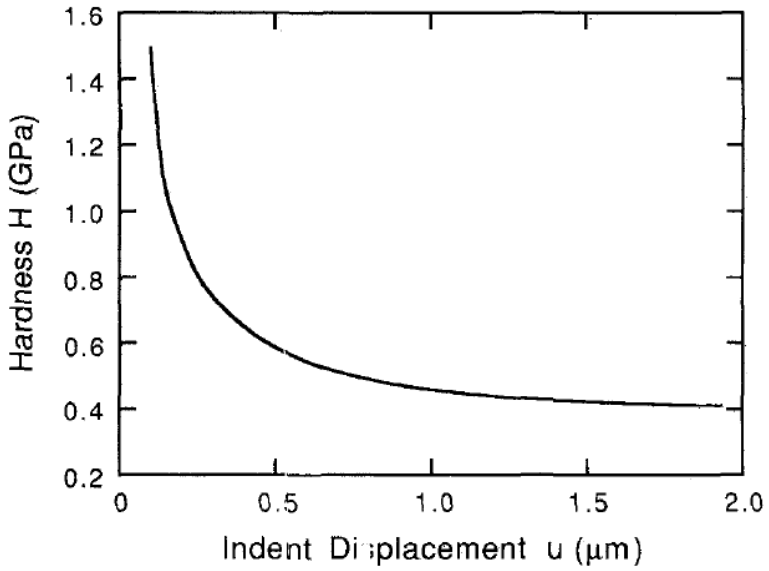

Figure 6.2: Hardness profile of a single crystal silver (Ag) as a function of displacement using nanoindentation with a Berkovich indenter of the same size as a Vickers indenter. [171].

Besides nanoindentation testing, compression test on micro-pillars can also be implemented to evaluate the size effect property. Compressive mechanical property of Ni micropillars having a size range from 5 to 40 μm in diameter is shown in Figure 6.3. Different from the nanoindentation test where hardness value versus indent displacement is displayed, the stress-strain curve is usually shown to illustrate and to study the size effect. From Figure 6.3, the mechanical properties of micro-pillars which have a diameter of 20 μm and 40 μm are similar to those of the bulk Ni sample, displaying a smooth transition from elastic to plastic flow. However, large strain bursts are observed from the samples with 5 μm diameter. The distinct change or the discontinuity in mechanical properties is another way to show the size effect phenomenon during the mechanical test.

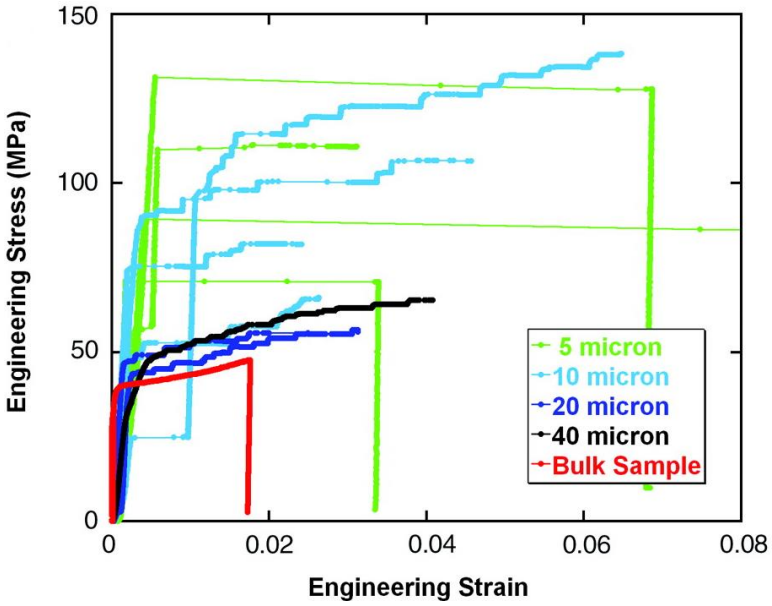

Figure 6.3: Mechanical behavior under compression at room temperature for pure Ni micropillars having a <134> orientation. Bulk Ni single crystal sample having dimensions of about 2.6 × 2.6 × 7.4 mm^3 is also displayed in the figure [163].

The size effect analysis for the TWIP steel was studied based on nanoindentation hardness theory and the hardness versus indentation depth data is shown in Figure 6.4. The distribution of hardness values does not show a noticeable size effect, i.e. hardness value

increases with indentation depth decreases. Because of the extremely small activation volume, the investigated TWIP steel is expected to have a marginal size effect at the best, which is confirmed and demonstrated by the nanoindentation test results in Figure 6.4 with error bars plotted as a function of displacement. From the data profile, the hardness values remain constant at ~3 GPa, which is consistent with the extremely low activation volume that was derived from the high strain rate sensitivity values.

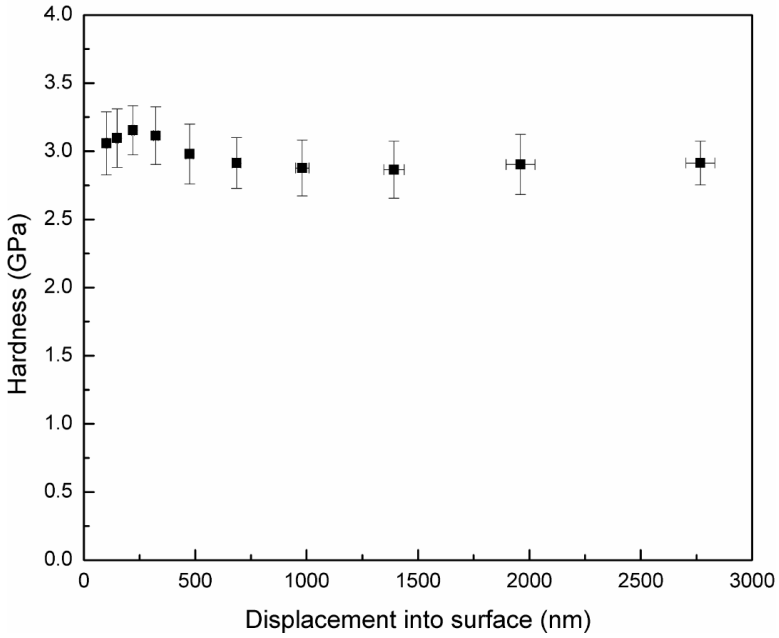

Figure 6.4: Hardness profile as a function of displacement from nanoindentation. The maximum load at each loading was 500 mN.

6.3 Stability under tension and compression

The earliest and most authoritative criterion of plastic instability published by Considère in 1885[172] is

$$\frac{\theta(\varepsilon)}{\sigma(\varepsilon)}\Big|_{\varepsilon=\epsilon NC} \leq 1 \tag{6.1}$$

where $\theta(\varepsilon)$ is the strain hardening rate, $\theta(\varepsilon) = \frac{d\sigma(\varepsilon)}{d\varepsilon}$. σ is the flow stress at a given strain rate $\dot{\varepsilon}$ and $\varepsilon = \epsilon NC$ is the strain at the onset of necking. The Considère criterion signifies

the onset of necking at the point where the strain hardening rate drops below the value of the flow stress at a given strain rate [173].

Figure 6.5 (a) displays the TWIP steel's true stress-strain curve along RD and the strain hardening rate versus true strain. The vertical axis has been rescaled for the strain hardening rate versus true strain curve and is shown in Figure 6.5 (b) for comparison. From Figure 6.5 (b) and Eq. (6.1), the instability condition of TWIP steel occurs at the strain of ~0.44 where the strain hardening rate drops below the true stress. According to the Considère criterion, the investigated TWIP steel has a strong stability under tension until the strain is 0.44 or larger. The necking and failure will happen if the strain passes 0.44, according to the Considère for a rate-independent material.

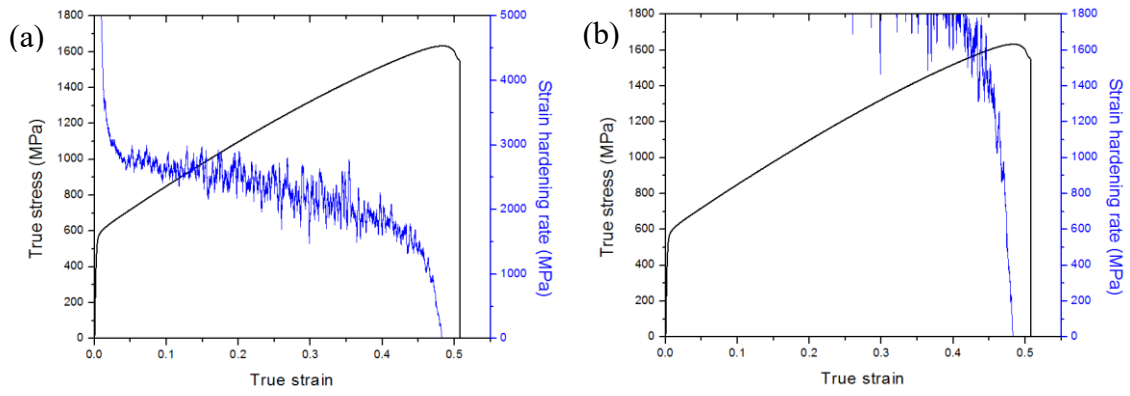

Figure 6. 5: True stress-strain curve (RD) and strain hardening rate vs. true strain (a, b).

In 1967, Hart [174] took the SRS (m) into consideration when discussing the stability under tension and came up with a new criterion as

$$\frac{\theta(\varepsilon)}{\sigma(\varepsilon)}\Big|_{\varepsilon=\epsilon NC} + m \leq 1 \qquad (6.2)$$

In Hart's theory, the plastic instability would occur under tension if the sum of the strain hardening rate over the flow stress and the SRS is equal or smaller than 1. As discussed in the previous context, the TWIP steel has a high SRS of 0.076. If considering the SRS in

Eq. (6.2), the instability of the TWIP steel under tension is postponed to a very late stage. This analysis is consistent with the experimental results that showed uniform elongation and negligible necking was observed under the tensile load.

The investigated TWIP steel exhibited uniform deformation upon high rate loading and no localization was observed from the post-loading images. The remarkable plastic stability under compression can be justified qualitatively at first. From Jonas et al [175], the propensity of flow localization is

$$\alpha = \frac{\gamma - 1}{m} \tag{6.3}$$

where γ is the normalized strain hardening rate. From Eq. 6.3, via the combination of the measured normalized strain hardening rate and the SRS value, the steel has a very low propensity to exhibit plastic instability. The investigated TWIP steel has a strong strain hardening rate and high SRS under compression which favors plastic stability.

Quantitative analysis on the plastic instability can be derived from Eq. (1.5) to be

$$\chi_{SB} = \left(\frac{-\frac{\partial \sigma}{\partial T}}{\rho c}\right)\frac{1}{m}\min\left\{1, \frac{1}{\left(\frac{n}{m}\right)+\left(\sqrt{\frac{n}{m}}\right)}\right\} \tag{6.3}$$

where a is a non-dimensional thermal softening parameter and a has been replaced by $-\frac{\frac{d\sigma}{dT}}{\rho c_P}$. One should note that the TWIP steel did not show any flow softening at high strain rates which leads to a very small value of χ_{SB} for the propensity of plastic instability. In other words, the possibility of having plastic instability in the steel is negative or impossible under high strain rate loading.

6.3 Zener-Hollomon parameter

The deformation behavior of the TWIP steel can be interpreted by the deformation temperature and strain rate, as described by the Zener-Hollomon equation. The Zener-

Hollomon parameter (Z) is defined by [7]

$$Z = \dot{\varepsilon}\exp(\frac{Q}{RT}) \tag{6.4}$$

Where R is the gas constant (8.314 J/mol/K), Q is the related activation energy for deformation. From the equation, it is known that an increase of the strain rate has an equivalent effect to that of a decrease in deformation temperature and vice versa. Either increasing the strain rate or decreasing the deformation temperature, i.e. achieving a high Z value, would facilitate the formation of deformation twins during plastic deformation [176, 177]. Moreover, a larger Z parameter would help to obtain finer twin layers, which is consistent with our TEM observations after the high strain rate test. The effect of strain rate was already discussed in the previous chapter, and the effect of temperature will be examined by QS compression test at elevated temperatures.

The compressive QS stress-strain curves obtained at elevated temperatures are given in Figure 6.5. The compression test was conducted from 223 K to 423 K with 50 K as the increment. The testing temperatures were selected within a range that twinning, other than phase transformation or deformation bands, would be the dominant deformation mechanism during compression [94, 178-186]. The compression test was stopped when the compressive strain reached 0.2 (20%). From the engineering and true stress-strain curves in Figure 6.5 (a) and (b), the yield stress decreases gradually with increasing the testing temperature. On the one hand, the strain hardening rate also decreases as the temperature increases which is displayed in Figure 6.5 (c). On the other hand, the hardening is still thought to be controlled by dislocation accumulation and austenite twining at these testing temperatures [187]. Moreover, the strain hardening rate decreases continuously without any serration up to the strain of about 0.2. Strain hardening exponent given by Figure 6.5

(d) is 0.23 at 223 K and keeps at 0.25 when the testing temperature was 173 K to 373 K then decreases to 0.18 when the testing temperature is 423 K.

In summary, decreasing the deformation temperature should have an equivalent effect on refining deformation twins and providing a strong strain hardening effect, which is consistent with the QS compression test at elevated temperatures. In general, the deformation behavior of the investigated TWIP steel could be explained and predicted by the Zener-Hollomon parameter.

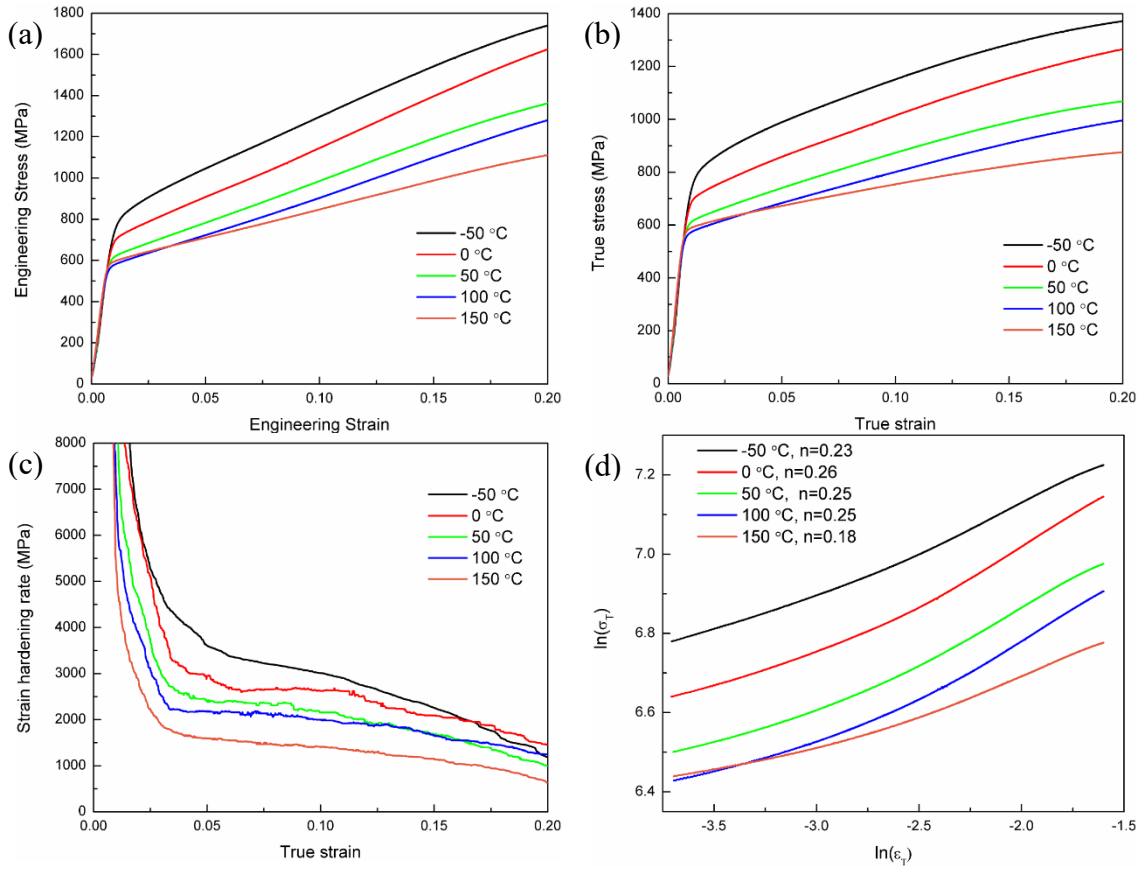

Figure 6. 6: Engineering (a) and true (b) stress-strain curves of investigated TWIP steel under QS compression at different temperatures. Strain hardening rates of the investigated TWIP steel under QS compression at different temperatures (c). Strain hardening exponent of the TWIP steel at different temperatures (d). Compression test was stopped at the strain of about 0.2.

6.4 Conclusions

The isotropic TWIP steel that was tested has an SRS value of ~0.076 along RD, TD and ND, which is much higher than that of CG Cu published in the literature. The activation volume was calculated to be ~$5.2b^3$ which is also much smaller than that of other CG, UFG and even NC FCC metals. The comparatively high SRS value and extremely small activation volume are the dominant factors why the investigated TWIP steel exhibits the observed strong strain rate hardening property.

The small activation volume contributes to the marginal size effect, which was demonstrated by nanoindentation testing. The hardness values were constant at ~3 GPa and negligible hardness value change has been observed as a function of indentation depth.

The TWIP steel exhibits an outstanding plastic stability under tension and compression. The extraordinary stability under tension attributes to the high strain hardening exponent and high SRS. The stability under compression are characterized by the high strain hardening exponent and high SRS.

The Zener-Hollomon parameter is used to justify the relationship between the mechanical properties and the formation of deformation twins. Being consistent with the Zener-Hollomon relationship, increasing the strain rate and decreasing the deformation temperature, i.e., achieving a high Z value, would facilitate the formation of deformation twins during plastic deformation and help to deliver a higher yield stress or flow stress.

CHAPTER 7: SUMMARY AND FUTURE WORKS

Two materials, heterogeneously layered W based materials with BCC structure and Fe-15Mn-2.5Si-2Si-0.6C TWIP steel with an FCC structure have been comprehensively investigated for aspects of their microstructure and mechanical properties, especially the occurrence of ASB or the lack thereof under high strain rate loading. In the heterogeneously layered structure, the stress wave propagated through the inhomogeneous layers and showed the propensity of ASB under high strain rate loading and ballistic testing conditions. In contrast to the ASB favoring material, the TWIP steel is shown to exhibit extraordinary strong strain hardening and strain rate hardening under QS and dynamic compressive loads. The significantly strong strain hardening and the high SRS led to the remarkable plastic stability under tension and compression. Moreover, the small activation volume also resulted in a marginal size effect that is seldom found in CG FCC metals.

7.1 Adiabatic shear favoring BCC layered structure

Heterogeneous multi-layer structures W/Fe/W and W/V/W were produced using a low homologous temperature rolling and diffusion bonding method to achieve a hierarchical structure, whereby the dimensional limitation of rolling was overcome. Three-layer sandwiched structures were firstly examined under OM and SEM, demonstrating no void or absence of delamination after bonding. The W grains in W/Fe/W structure display an elongated structure along the RD with a width of 5-10 μm which was introduced by low homologous temperature rolling.

The inter-diffusion between W and Fe atoms at the W/Fe interface was investigated by SEM and nanoindentation. W atoms have a higher ability to diffuse into the interlayer material which is Fe or V in the three-layer structure. The nanoindentation results revealed

that no significant hardness increase was observed at the interface area, which could be explained as that no excessive amount of intermetallic compounds formed during the bonding process or that the intermetallic phase was too small to detect under nanoindentation. However, solid solution was found inside the interlayer.

The high strain rate mechanical properties of W/Fe/W and W/V/W samples were studied using the SHPB. Both of the W/Fe/W and W/V/W samples displayed strong flow softening and the peak flow stress of W/Fe/W reached ~4000 MPa at a strain rate of ~8×10^3 s^{-1} and 3500 MPa for W/V/W at a strain rate of ~7×10^3 s^{-1}. ASBs, as well as cracks as a consequence of severe plastic deformation, were observed on the cross-sectional surface of the W/Fe/W and W/V/W samples after the dynamic compression tests. The width of the ASB was identified as ~100 μm. In the W/Fe/W system, the temperature rise within the band was calculated to be ~467 K at ~8×10^3 s^{-1} at the strain of 0.1 and the shear strain reached to 0.84 within the band. The global temperature rise of W/Fe/W sample was ~113 K when the compressive strain was 0.1.

The microstructure underwent a significant change after the high strain rate test. After bonding, the Fe grains had a CG structure and grew to 5-10 μm with only a few dislocations being observed under TEM. Upon high strain rate compression, shear bands propagated through the heterogeneous layers and the bonding interface remained almost intact upon high strain rate loading. However, the Fe grains outside the shear bands were severely deformed and subgrains as well as dislocation cells were observed. Inside the ASB, Fe grains were recrystallized and refined into the NC regime with an average grain size of ~100-200 nm due to the sudden temperature rise and subsequent quench within the band.

The W grains in the W/Fe/W system were observed with few dislocations being shown

after bonding. Upon high rate loading, an excessive number of dislocations was introduced in the W layer by the compressive strain. A laminar structure with thick dislocation walls developed in the W layer inside the ASB due to the temperature rise as well as the severe shear strain accumulated inside the bands.

Besides the three-layer sandwiched structure, a four-interlayer structure was also fabricated using diffusion bonding. Inter-diffusion occurred between W and Fe atoms and was examined by EDX at the interfaces. No large voids or delamination have been observed after bonding. Upon high rate loading ranging from ~3×10^3 s^{-1} to 4.5×10^3 s^{-1}, the W/Fe bonding faces remained intact with several light ASBs appearing on the cross-sectional surface. The shear bands propagated through the inhomogeneous layers of the multi-interlayer structure at high strain rate.

Subscale projectiles were fabricated from heterogeneous multi-layers and the ballistic performance was evaluated. ASBs were identified at the head of the projectile residues and hence, demonstrating an early onset of shear localization behavior. ASBs and significant shear failure features were observed under microscopy, suggesting that the adiabatic shear failure was the dominant failure mechanism of the heterogeneous layered structure during the ballistic test. The W/Fe faces inside the residues were still intact after the test.

In general, W/Fe/W system has a strong bonding interface that survived the high strain rate loading and ballistic test. Moreover, this heterogeneously layered structure not only provided a way to extend the geometrical dimensions of rolled W, but also has a propensity to have ASB under dynamic loading condition. This new type of layered material could be used to make a novel W-based KE penetrator.

7.2 Adiabatic shear resistant FCC steel

The as-received Fe-15Mn-2.5Si-2Si-0.6C TWIP steel exhibited a uniform microstructure with only austenitic FCC phase being observed before and after the mechanical tests. The grain size is ~5 μm to 10 μm. Only mild {100}<001> and {001}<211> textures existed in the as-received steel.

The TWIP steel was isotropic along the RD, TD and ND and exhibited bilinear true stress-strain curves as well as extraordinary strong strain hardening with a yield strength of ~600 MPa and high ultimate tensile strength of ~1000 MPa. The strain hardening exponent was determined to be ~0.33 under tensile load. Coarse dimples observed under SEM were believed to be caused by the heterogeneous structure with embedded nanotwin bundles.

An outstanding strong strain hardening behavior was observed under QS and high strain rate compressive loads. The yield strength was ~600 MPa under QS compression and the flow stress was increased to 900 MPa at ~ 6×10^3 s^{-1}. Postmortem examination revealed that the TWIP steel had a uniform deformation at high strain rate without any localized plastic deformation being observed. The strain hardening rate of the dynamically tested sample is lower than that of the sample tested at QS status and has fewer serrations, which could be explained as that high strain rate loading has suppressed the dynamic strain aging.

TEM observations of the dynamically loaded sample suggested an excessive number of thin deformation twins and stacking faults. Upon high strain rate loading, less time was available for twin embryos to grow compared to that available in QS tension, which could lead to the formation of nanotwins.

The isotropic TWIP steel has an SRS value of ~0.076 along the RD, TD and ND, which

is much higher than that of CG Cu or other CG FCC metals published in the literature. The activation volume was calculated to be ~5.2b^3 which is also much smaller than that of other FCC metals. This combination of strong strain hardening and strain rate hardening rendered the TWIP steel to be strongly resistant to plastic instability under both tension and compression. The very small activation volume, ~5b^3, leads to a marginal size effect of the TWIP steel. The nanohardness profile nearly remains constant at ~3 GPa.

The mechanical properties of the TWIP steel is consistent with the Zener-Hollomon equation. The experimental results at high strain rate and elevated temperatures revealed that increasing the strain rate and decreasing the deformation temperature facilitate the formation of deformation twins during plastic deformation and assist in increasing the yield stress or flow stress.

In summary, the mechanical properties of Fe-15Mn-2.5Si-2Si-0.6C TWIP steel have been comprehensively studied and the reason behind the observed substantial plastic stability was explained in the context of deformation kinetics. The extremely small activation volume and its contribution to the marginal size effect on the CG TWIP steel was first proposed and studied in the literatures.

REFERENCES

[1] L.S. Magness, Mechanics of Materials, 17 (1994) 147-154.

[2] L. Magness Jr, Dissertation Abstracts International(USA), 53 (1992) 270.

[3] L.S. Magness, Tungsten & Tungsten Alloys - 1992, (1993) 15-22.

[4] W.D. Cai, Y. Li, R.J. Dowding, F.A. Mohamed, E.J. Lavernia, Rev. Part. Mater., 3 (1995) 71-131.

[5] W. Leonard, L. Magness, DTIC Document, 1995.

[6] L.S. Magness, W.A. Leonard, D. Kapoor, M. Chung, J. Trogolo, ARMY RESEARCH LAB ABERDEEN PROVING GROUND MD, 1998.

[7] C. Zener, J. Hollomon, Journal of applied physics, 15 (1944) 22-32.

[8] R. Recht, J. appl. Mech, 31 (1964) 186-193.

[9] Y. Bai, A criterion for thermo-plastic shear instability, Shock waves and high-strain-rate phenomena in metals, Springer, 1981, pp. 277-284.

[10] B. Yilong, C. Chemin, Y. Shanbing, Acta mechanica sinica, 2 (1986) 1-7.

[11] H.C. Rogers, Annual Review of Materials Science, 9 (1979) 283-311.

[12] K.M. Roessig, J.J. Mason, Exp. Mech., 38 (1998) 196-203.

[13] T.J. Burns, M.A. Davies, International Journal of Plasticity, 18 (2002) 487-506.

[14] A. Molinari, D. Dudzinski, Comptes Rendus De L Academie Des Sciences Serie Ii, 315 (1992) 399-405.

[15] J.D.P. Velasquez, B. Bolle, P. Chevrier, G. Geandier, A. Tidu, Materials Science and Engineering a-Structural Materials Properties Microstructure and Processing, 452 (2007) 469-474.

[16] M. Armendia, A. Garay, L.M. Iriarte, P.J. Arrazola, Journal of Materials Processing Technology, 210 (2010) 197-203.

[17] M. Baker, J. Rosler, C. Siemers, Comput. Struct., 80 (2002) 495-513.

[18] A. Molinari, C. Musquar, G. Sutter, International Journal of Plasticity, 18 (2002) 443-459.

[19] M. Calamaz, D. Coupard, F. Girot, Int. J. Mach. Tools Manuf., 48 (2008) 275-288.

[20] S.L. Semiatin, M.R. Staker, J.J. Jonas, Acta Metallurgica, 32 (1984) 1347-1354.

[21] C.A. Bronkhorst, E.K. Cerreta, Q. Xue, P.J. Maudlin, T.A. Mason, G.T. Gray, International Journal of Plasticity, 22 (2006) 1304-1335.

[22] R. Vaidyanathan, M. Dao, G. Ravichandran, S. Suresh, Acta Materialia, 49 (2001) 3781-3789.

[23] R.D. Conner, R.B. Dandliker, V. Scruggs, W.L. Johnson, Int. J. Impact Eng., 24 (2000) 435-444.

[24] R.S. Culver, Thermal instability strain in dynamic plastic deformation, Metallurgical effects at high strain rates, Springer, 1973, pp. 519-530.

[25] X.Q. Zhou, S.K. Li, J.X. Liu, Y.C. Wang, X. Wang, Materials Science and Engineering a-Structural Materials Properties Microstructure and Processing, 527 (2010) 4881-4886.

[26] T.W. Wright, The physics and mathematics of adiabatic shear bands, Cambridge University Press, 2002.

[27] Q. Wei, H. Zhang, B. Schuster, K. Ramesh, R. Valiev, L. Kecskes, R. Dowding, L. Magness, K. Cho, Acta materialia, 54 (2006) 4079-4089.

[28] Y.B. Xu, J.H. Zhang, Y.L. Bai, M.A. Meyers, Metallurgical and Materials Transactions a-Physical Metallurgy and Materials Science, 39A (2008) 811-843.

[29] A. Marchand, J. Duffy, J. Mech. Phys. Solids, 36 (1988) 251-+.

[30] Q. Wei, L. Kecskes, K. Ramesh, Materials Science and Engineering: A, 578 (2013) 394-401.

[31] S.N. Medyanik, W.K. Liu, S.F. Li, J. Mech. Phys. Solids, 55 (2007) 1439-1461.

[32] M.A. Meyers, K.P. Staudhammer, L.E. Murr, Metallurgical applications of shock-wave and high-strain-rate phenomena, Marcel Dekker New York, NY, 1986.

[33] M.R. Staker, Acta Metallurgica, 29 (1981) 683-689.

[34] U.S. Lindholm, G.R. Johnson, Strain-rate effects in metals at large shear strains, Material Behavior Under High Stress and Ultrahigh Loading Rates, Springer, 1983, pp. 61-79.

[35] Q. Wei, Z.L. Pan, X.L. Wu, B.E. Schuster, L.J. Kecskes, R.Z. Valiev, Acta Materialia, 59 (2011) 2423-2436.

[36] M. Tang, L.P. Kubin, G.R. Canova, Acta Materialia, 46 (1998) 3221-3235.

[37] Q. Wei, S. Cheng, K. Ramesh, E. Ma, Materials Science and Engineering: A, 381 (2004) 71-79.

[38] R.J. Asaro, S. Suresh, Acta Materialia, 53 (2005) 3369-3382.

[39] G. Taylor, Progress in Materials Science, 36 (1992) 29-61.

[40] A.A. Elmustafa, D.S. Stone, J. Mech. Phys. Solids, 51 (2003) 357-381.

[41] Z. Pan, F. Xu, S.N. Mathaudhu, L.J. Kecskes, W.H. Yin, X.Y. Zhang, K.T. Hartwig, Q. Wei, Acta Materialia, 60 (2012) 2310-2323.

[42] B.E. Schuster, J.P. Ligda, Z.L. Pan, Q. Wei, Jom, 63 (2011) 27-31.

[43] Y.Z. Guo, Y.L. Li, Z. Pan, F.H. Zhou, Q. Wei, Mechanics of Materials, 42 (2010) 1020-1029.

[44] Q. Wei, B.E. Schuster, S.N. Mathaudhu, K.T. Hartwig, L.J. Kecskes, R.J. Dowding, K.T. Ramesh, Materials Science and Engineering a-Structural Materials Properties Microstructure and Processing, 493 (2008) 58-64.

[45] Q. Xing, X. Huang, N. Hansen, Metallurgical and Materials Transactions a-Physical Metallurgy and Materials Science, 37A (2006) 1311-1322.

[46] Q. Wei, T. Jiao, K. Ramesh, E. Ma, L. Kecskes, L. Magness, R. Dowding, V. Kazykhanov, R. Valiev, Acta Materialia, 54 (2006) 77-87.

[47] Q. Wei, K.T. Ramesh, E. Ma, L.J. Kesckes, R.J. Dowding, V.U. Kazykhanov, R.Z. Valiev, Applied Physics Letters, 86 (2005) 3.

[48] Q. Wei, T. Jiao, K. Ramesh, E. Ma, Scripta materialia, 50 (2004) 359-364.

[49] G.T. Gray, T.C. Lowe, C.M. Cady, R.Z. Valiev, I.V. Aleksandrov, Nanostruct. Mater., 9 (1997) 477-480.

[50] L. Lu, S.X. Li, K. Lu, Scripta Materialia, 45 (2001) 1163-1169.

[51] R. Schwaiger, B. Moser, M. Dao, N. Chollacoop, S. Suresh, Acta Materialia, 51 (2003) 5159-5172.

[52] L. Lu, R. Schwaiger, Z.W. Shan, M. Dao, K. Lu, S. Suresh, Acta Materialia, 53 (2005) 2169-2179.

[53] Z. Pan, Y. Guo, S. Mathaudhu, L. Kecskes, K. Hartwig, Q. Wei, Journal of Materials Science, 43 (2008) 7379-7384.

[54] Q. Wei, L. Kecskes, Materials Science and Engineering: A, 491 (2008) 62-69.

[55] Q. Wei, T. Jiao, S.N. Mathaudhu, E. Ma, K.T. Hartwig, K.T. Ramesh, Materials Science and Engineering a-Structural Materials Properties Microstructure and Processing, 358 (2003) 266-272.

[56] J. Ligda, B. Schuster, Q. Wei, Scripta Materialia, 67 (2012) 253-256.

[57] Q. Wei, L. Kecskes, T. Jiao, K.T. Hartwig, K.T. Ramesh, E. Ma, Acta Materialia, 52 (2004) 1859-1869.

[58] Y.M. Wang, E. Ma, Materials Science and Engineering a-Structural Materials Properties Microstructure and Processing, 375 (2004) 46-52.

[59] C.E. Anderson, S.A. Mullin, A.J. Piekutowski, N.W. Blaylock, K.L. Poormon, Int. J. Impact Eng., 18 (1996) 1-22.

[60] N.F. Kazakov, Diffusion bonding of materials, Elsevier, 2013.

[61] Y. Saito, N. Tsuji, H. Utsunomiya, T. Sakai, R.G. Hong, Scripta Materialia, 39 (1998) 1221-1227.

[62] N. Tsuji, Y. Saito, H. Utsunomiya, S. Tanigawa, Scripta materialia, 40 (1999) 795-800.

[63] N. Orhan, T.I. Khan, M. Eroglu, Scripta Materialia, 45 (2001) 441-446.

[64] D. Spisak, J. Hafner, Physical Review B, 70 (2004) 13.

[65] W.W. Basuki, J. Aktaa, Journal of Nuclear Materials, 417 (2011) 524-527.

[66] W.W. Basuki, J. Aktaa, Journal of Nuclear Materials, 429 (2012) 335-340.

[67] P. Zhao, S. Wang, S.B. Guo, Y.X. Chen, Y.H. Ling, J.T. Li, Materials & Design, 42 (2012) 21-24.

[68] S. Wang, Y. Ling, P. Zhao, N. Zang, J. Wang, S. Guo, J. Zhang, G. Xu, Fusion Engineering and Design, 88 (2013) 248-252.

[69] W.W. Basuki, J. Aktaa, Journal of Nuclear Materials, 459 (2015) 217-224.

[70] S. Wang, Y. Ling, J. Wang, G. Xu, Vacuum, 114 (2015) 58-65.

[71] S. Takemoto, H. Nitta, Y. Iijima §, Y. Yamazaki, Philosophical Magazine, 87 (2007) 1619-1629.

[72] Z.H. Zhong, T. Hinoki, T. Nozawa, Y.H. Park, A. Kohyama, Journal of Alloys and Compounds, 489 (2010) 545-551.

[73] W.D. Callister, D.G. Rethwisch, Materials science and engineering, John Wiley & Sons NY, 2011.

[74] T.B. Massalski, H. Okamoto, P. Subramanian, L. Kacprzak, W.W. Scott, Binary alloy phase diagrams, American society for metals Metals Park, OH, 1986.

[75] A. Serjouei, R.Q. Chi, Z.Y. Zhang, I. Sridhar, Int. J. Impact Eng., 77 (2015) 30-41.

[76] B. Matchen, Advanced Ceramic Materials: Applications of Advanced Materials in a High-Tech Society I, 122-1 (1996) 333-342.

[77] P. Karandikar, G. Evans, S. Wong, M. Aghajanian, M. Sennett, Adv Ceram Armor IV Ceram Eng Sci Proc, 29 (2009) 163-175.

[78] J.S. Montgomery, M.G.H. Wells, Jom-J Min Met Mat S, 53 (2001) 29-32.

[79] S.J. Perez-Bergquist, G.T. Gray, E.K. Cerreta, C.P. Trujillo, A. Perez-Bergquist, Materials Science and Engineering a-Structural Materials Properties Microstructure and Processing, 528 (2011) 8733-8741.

[80] J.C. Li, Mechanical properties of nanocrystalline materials, CRC Press, 2011.

[81] V. Hohler, K. Weber, R. Tham, B. James, A. Barker, I. Pickup, Int. J. Impact Eng., 26 (2001) 333-344.

[82] S. Curtze, V.T. Kuokkala, Acta Materialia, 58 (2010) 5129-5141.

[83] R.L. Xiong, H.B. Peng, S.L. Wang, H.T. Si, Y.H. Wen, Materials & Design, 85 (2015) 707-714.

[84] O. Grassel, L. Kruger, G. Frommeyer, L.W. Meyer, International Journal of Plasticity, 16 (2000) 1391-1409.

[85] F.Y. Dong, J.C. Pang, P. Zhang, Q.Q. Duan, Z.F. Zhang, Advanced Engineering Materials, 17 (2015) 1675-1682.

[86] R.A. Hadfield, Science, 12 (1888) 284-286.

[87] D. Barbier, N. Gey, S. Allain, N. Bozzolo, M. Humbert, Materials Science and Engineering a-Structural Materials Properties Microstructure and Processing, 500 (2009) 196-206.

[88] L. Bracke, K. Verbeken, L. Kestens, J. Penning, Acta Materialia, 57 (2009) 1512-1524.

[89] I. Gutierrez-Urrutia, S. Zaefferer, D. Raabe, Materials Science and Engineering a-Structural Materials Properties Microstructure and Processing, 527 (2010) 3552-3560.

[90] H. Idrissi, K. Renard, D. Schryvers, P.J. Jacques, Scripta Materialia, 63 (2010) 961-964.

[91] I. Gutierrez-Urrutia, D. Raabe, Acta Materialia, 59 (2011) 6449-6462.

[92] S. Hong, S.Y. Shin, H.S. Kim, S. Lee, S.K. Kim, K.G. Chin, N.J. Kim, Metallurgical and Materials Transactions a-Physical Metallurgy and Materials Science, 44A (2013) 776-786.

[93] S. Lee, W. Woo, B.C. de Cooman, Metallurgical and Materials Transactions a-Physical Metallurgy and Materials Science, 47A (2016) 2125-2140.

[94] J.E. Jung, J. Park, J.S. Kim, J.B. Jeon, S.K. Kim, Y.W. Chang, Met. Mater.-Int., 20 (2014) 27-34.

[95] Y.P. Lu, D.A. Molodov, G. Gottstein, ISIJ Int., 51 (2011) 812-817.

[96] A.A. Saleh, E.V. Pereloma, A.A. Gazder, Materials Science and Engineering a-Structural Materials Properties Microstructure and Processing, 528 (2011) 4537-4549.

[97] D. Barbier, V. Favier, B. Bolle, Materials Science and Engineering a-Structural Materials Properties Microstructure and Processing, 540 (2012) 212-225.

[98] L. Bracke, K. Verbeken, L.A.I. Kestens, Scripta Materialia, 66 (2012) 1007-1011.

[99] O. Bouaziz, H. Zurob, B. Chehab, J.D. Embury, S. Allain, M. Huang, Materials Science and Technology, 27 (2011) 707-709.

[100] L.A. Barrales-Mora, Y. Lu, D.A. Molodov, Steel Res. Int., 82 (2011) 119-126.

[101] O. Bouaziz, S. Allain, C.P. Scott, P. Cugy, D. Barbier, Curr. Opin. Solid State Mat. Sci., 15 (2011) 141-168.

[102] H.J. Lai, C.M. Wan, Journal of Materials Science, 24 (1989) 2449-2453.

[103] X. Liang, J.R. McDermid, O. Bouaziz, X. Wang, J.D. Embury, H.S. Zurob, Acta Materialia, 57 (2009) 3978-3988.

[104] E. Bayraktar, F.A. Khalid, C. Levaillant, Journal of Materials Processing Technology, 147 (2004) 145-154.

[105] J. Seol, J. Kim, S. Na, C. Park, H. Kim, Acta Materialia, (2017).

[106] W. Leslie, G. Rauch, Metallurgical and Materials Transactions A, 9 (1978) 343-349.

[107] B. Qin, Pohang University of Science and Technology, (2007).

[108] B.C. De Cooman, Y. Estrin, S.K. Kim, Acta Materialia, (2017).

[109] C. Efstathiou, H. Sehitoglu, Acta Materialia, 58 (2010) 1479-1488.

[110] J.W. Christian, S. Mahajan, Progress in Materials Science, 39 (1995) 1-157.

[111] I. Karaman, H. Sehitoglu, K. Gall, Y.I. Chumlyakov, H.J. Maier, Acta Materialia, 48 (2000) 1345-1359.

[112] Y.N. Dastur, W.C. Leslie, Metallurgical Transactions a-Physical Metallurgy and Materials Science, 12 (1981) 749-759.

[113] W.S. Owen, M. Grujicic, Acta Materialia, 47 (1998) 111-126.

[114] P.H. Adler, G.B. Olson, W.S. Owen, Metallurgical Transactions a-Physical Metallurgy and Materials Science, 17 (1986) 1725-1737.

[115] K. Lu, Nat. Rev. Mater., 1 (2016) 13.

[116] K. Lu, F.K. Yan, H.T. Wang, N.R. Tao, Scripta Materialia, 66 (2012) 878-883.

[117] H. Idrissi, K. Renard, L. Ryelandt, D. Schryvers, P.J. Jacques, Acta Materialia, 58 (2010) 2464-2476.

[118] J. Venables, Philosophical Magazine, 30 (1974) 1165-1169.

[119] J. Venables, Journal of Physics and Chemistry of Solids, 25 (1964) 685IN1691-1690IN6692.

[120] J.B. Cohen, J. Weertman, Acta Metallurgica, 11 (1963) 996-&.

[121] S. Mahajan, G. Chin, Acta metallurgica, 21 (1973) 1353-1363.

[122] T.H. Courtney, Mechanical behavior of materials, Waveland Press, 2005.

[123] A.H. Cottrell, B.A. Bilby, Proceedings of the Physical Society of London Section A, 62 (1949) 49-62.

[124] P. McCormigk, Acta Metallurgica, 20 (1972) 351-354.

[125] R.A. Mulford, U.F. Kocks, Acta Metallurgica, 27 (1979) 1125-1134.

[126] R.C. Picu, Acta Materialia, 52 (2004) 3447-3458.

[127] L. Chen, H.S. Kim, S.K. Kim, B.C. Cooman, ISIJ Int., 47 (2007) 1804-1812.

[128] K. Renard, S. Ryelandt, P.J. Jacques, Materials Science and Engineering a-Structural Materials Properties Microstructure and Processing, 527 (2010) 2969-2977.

[129] A. Bintu, G. Vincze, C.R. Picu, A.B. Lopes, J.J. Gracio, F. Barlat, Materials Science and Engineering a-Structural Materials Properties Microstructure and Processing, 629 (2015) 54-59.

[130] J. Chen, L. Lu, K. Lu, Scripta Materialia, 54 (2006) 1913-1918.

[131] R.G. Xiong, R.Y. Fu, Y. Su, Q. Li, X.C. Wei, L. Li, J. Iron Steel Res. Int., 16 (2009) 81-+.

[132] D.Z. Li, Y.H. Wei, C.Y. Liu, L.F. Hou, D.F. Liu, X.Z. Jin, J. Iron Steel Res. Int., 17 (2010) 67-73.

[133] Y. Ha, H. Kim, K.H. Kwon, S.-G. Lee, S. Lee, N.J. Kim, Metallurgical and Materials Transactions A, 46 (2015) 545-548.

[134] L.A. Dobrzanski, W. Borek, J. Mazurkiewicz, Materialwiss. Werkstofftech., 47 (2016) 428-435.

[135] S.Q. Xu, D. Ruan, J.H. Beynon, Y.H. Rong, Materials Science and Engineering a-Structural Materials Properties Microstructure and Processing, 573 (2013) 132-140.

[136] H.K. Yang, Z.J. Zhang, Z.F. Zhang, Materials Science and Engineering a-Structural Materials Properties Microstructure and Processing, 622 (2015) 184-188.

[137] O. Bouaziz, N. Guelton, Materials Science and Engineering a-Structural Materials Properties Microstructure and Processing, 319 (2001) 246-249.

[138] S. Dancette, L. Delannay, K. Renard, M.A. Melchior, P.J. Jacques, Acta Materialia, 60 (2012) 2135-2145.

[139] T. Das, R. Saha, S. Bera, K. Dahmen, M. Ghosh, A. Haldar, W. Bleck, S.G. Chowdhury, Metallurgical and Materials Transactions a-Physical Metallurgy and Materials Science, 46A (2015) 6-11.

[140] C. Haase, S.G. Chowdhury, L.A. Barrales-Mora, D.A. Molodov, G. Gottstein, Metallurgical and Materials Transactions a-Physical Metallurgy and Materials Science, 44A (2013) 911-922.

[141] J.E. Jin, Y.K. Lee, Materials Science and Engineering a-Structural Materials Properties Microstructure and Processing, 527 (2009) 157-161.

[142] J.G. Kim, S. Hong, N. Anjabin, B.H. Park, S.K. Kim, K.G. Chin, S. Lee, H.S. Kim, Materials Science and Engineering a-Structural Materials Properties Microstructure and Processing, 633 (2015) 136-143.

[143] Z.Y. Tang, R.D.K. Misra, M. Ma, N. Zan, Z.Q. Wu, H. Ding, Materials Science and Engineering a-Structural Materials Properties Microstructure and Processing, 624 (2015) 186-192.

[144] S. Vercammen, B. Blanpain, B.C. De Cooman, P. Wollants, Acta Materialia, 52 (2004) 2005-2012.

[145] Y.F. Shen, N. Jia, R.D.K. Misra, L. Zuo, Acta Materialia, 103 (2016) 229-242.

[146] E. Lassner, W.-D. Schubert, Tungsten: properties, chemistry, technology of the element, alloys, and chemical compounds, Springer Science & Business Media, 2012.

[147] Y. Prasad, K. Rao, S. Sasidhar, Hot working guide: a compendium of processing maps, ASM international, 2015.

[148] G. Henshall, S. Torres, (1993).

[149] D. Jia, K.T. Ramesh, Exp. Mech., 44 (2004) 445-454.

[150] H. Kuhn, D. Medlin, ASM International, Member/Customer Service Center, Materials Park, OH 44073-0002, USA, 2000. 998, (2000).

[151] B. Schuster, L. Magness, DTIC Document, 2005.

[152] N. Peterson, ADVANCED METALS RESEARCH CORP SOMERVILLE MA, 1960.

[153] Q. Liu, C. Maurice, J. Driver, N. Hansen, Metallurgical and Materials Transactions a-Physical Metallurgy and Materials Science, 29 (1998) 2333-2344.

[154] J.K. Kim, B.C. De Cooman, Materials Science and Engineering a-Structural Materials Properties Microstructure and Processing, 676 (2016) 216-231.

[155] K.A. Ofei, L. Zhao, J. Sietsma, J. Mater. Sci. Technol., 29 (2013) 161-167.

[156] S. Asgari, E. ElDanaf, S.R. Kalidindi, R.D. Doherty, Metallurgical and Materials Transactions a-Physical Metallurgy and Materials Science, 28 (1997) 1781-1795.

[157] L. Xiong, Z.S. You, L. Lu, Scripta Materialia, 119 (2016) 55-59.

[158] D.P. Field, B.W. True, T.M. Lillo, J.E. Flinn, Materials Science and Engineering a-Structural Materials Properties Microstructure and Processing, 372 (2004) 173-179.

[159] L. Lu, X. Chen, X. Huang, K. Lu, Science, 323 (2009) 607-610.

[160] Y.F. Shen, L. Lu, M. Dao, S. Suresh, Scripta Materialia, 55 (2006) 319-322.

[161] Q. Wei, Journal of materials science, 42 (2007) 1709-1727.

[162] O. Bouaziz, S. Allain, C. Scott, Scripta Materialia, 58 (2008) 484-487.

[163] M.D. Uchic, D.M. Dimiduk, J.N. Florando, W.D. Nix, Science, 305 (2004) 986-989.

[164] W.D. Nix, H.J. Gao, Journal of the Mechanics and Physics of Solids, 46 (1998) 411-425.

[165] M.R. Begley, J.W. Hutchinson, J. Mech. Phys. Solids, 46 (1998) 2049-2068.

[166] W.J. Poole, M.F. Ashby, N.A. Fleck, Scripta Materialia, 34 (1996) 559-564.

[167] J.F. Nye, Acta Metallurgica, 1 (1953) 153-162.

[168] M. Ashby, Philosophical Magazine, 21 (1970) 399-424.

[169] N.A. Fleck, G.M. Muller, M.F. Ashby, J.W. Hutchinson, Acta Metall Mater, 42 (1994) 475-487.

[170] H. Li, A. Ghosh, Y.H. Han, R.C. Bradt, J. Mater. Res., 8 (1993) 1028-1032.

[171] Q. Ma, D.R. Clarke, J. Mater. Res., 10 (1995) 853-863.

[172] A. Considère, Series, 1885.

[173] I. Yasnikov, A. Vinogradov, Y. Estrin, Scripta Materialia, 76 (2014) 37-40.

[174] E.W. Hart, Acta Metallurgica, 15 (1967) 351-&.

[175] J. Jonas, R. Holt, C. Coleman, Acta Metallurgica, 24 (1976) 911-918.

[176] Y.S. Li, Y. Zhang, N.R. Tao, K. Lu, Acta Materialia, 57 (2009) 761-772.

[177] G.H. Xiao, N.R. Tao, K. Lu, Scripta Materialia, 59 (2008) 975-978.

[178] G. Frommeyer, O. Grassel, Rev. Metall.-Cah. Inf. Techn., 95 (1998) 1299-1310.

[179] E. Girault, P. Jacques, P. Harlet, K. Mols, J. Van Humbeeck, E. Aernoudt, F. Delannay, Materials Characterization, 40 (1998) 111-118.

[180] G. Frommeyer, U. Brux, P. Neumann, ISIJ Int., 43 (2003) 438-446.

[181] P.J. Jacques, Q. Furnemont, F. Lani, T. Pardoen, F. Delannay, Acta Materialia, 55 (2007) 3681-3693.

[182] H. Ding, D. Song, Z.Y. Tang, P. Yang, Materials Science and Engineering a-Structural Materials Properties Microstructure and Processing, 528 (2011) 868-873.

[183] J.B. Seol, D. Raabe, P.P. Choi, Y.R. Im, C.G. Park, Acta Materialia, 60 (2012) 6183-6199.

[184] X. Sun, A. Soulami, K.S. Choi, O. Guzman, W. Chen, Materials Science and Engineering a-Structural Materials Properties Microstructure and Processing, 541 (2012) 1-7.

[185] S. Lee, Y. Estrin, B.C. De Cooman, Metallurgical and Materials Transactions a-Physical Metallurgy and Materials Science, 45a (2014) 717-730.

[186] S. Martin, S. Wolf, U. Martin, L. Kruger, D. Rafaja, Metallurgical and Materials Transactions a-Physical Metallurgy and Materials Science, 47A (2016) 49-58.

[187] W.J. Dan, F. Liu, W.G. Zhang, Modelling and Simulation in Materials Science and Engineering, 23 (2015).